Aus dem Institut für Immunologie, Medizinische Fakultät Carl Gustav Carus der Technischen Universität Dresden
Direktor: Herr Prof. Dr. med. Axel Roers

The role of RNase H2 in genome maintenance and autoimmune disease

Dissertationsschrift

zur Erlangung des akademischen Grades
Doctor rerum medicinalium (Dr. rer. medic.)

vorgelegt
der Medizinischen Fakultät Carl Gustav Carus
der Technischen Universität Dresden
von

Diplom Biologe Björn Hiller

aus Schwelm

Dresden, Mai 2015

1. **Gutachter:**

2. **Gutachter:**

Tag der mündlichen Prüfung: (Verteidigungstermin)

gez.: _____
Vorsitzender der
Promotionskommission

Content

Abbreviations

AGS	Aicardi Goutières Syndrome
AP	alkaline phosphatase
APC	antigen-presenting cell
ATM	Ataxia telangiectasia mutated
ATR	Ataxia telangiectasia mutated and Rad3-related
bp	base pairs
BSA	bovine serum albumine
CLE	cutaneous lupus erythematosus
cpm	counts per minute
CSF	cerebrospinal fluid
Ctrl/CTRL	Control
DAMP	danger-associated molecular pattern
DC	dendritic cell
DDR	DNA damage response
DIG	Digoxigenin
dNTPs	desoxyribonucleotide triphosphates
dsDNA	double-stranded DANN
dsRNA	double-stranded RNA
DT	diptheria toxin
EDTA	ethylenediaminetetraacetic acid
EGTA	ethylene glycol tetraacetic acid
EMS	ethyl methanesulfonate
ES cells	embryonic stem cells
FACS	fluorescence-assisted cell sorting
H&E	hematoxylin and eosin
H2AX	histone 2AX
HR	homologous recombination
HSC	Hematopoietic stem cells
HU	hydroxyurea
IgG	immunoglobulin G
IL	interleukin
IVC	individually ventilated cage
kb	kilobase pairs
kDa	kilo Dalton
KO	knockout
KOF	knockout first
LPS	lipopolysaccharide
MEF	mouse embryonic fibroblasts
MMR	mismatch repair
MPP	Multi potent progenitor
MTC	Masson`s trichrome

neo	neomycin
NHEJ	non-homologous end-joining
nM/µM/mM/M	nano-/micro-/millimolar/molar
nt	nucleotides
PAMP	pathogen-asociated molecular pattern
PBS	Phosphate-buffered saline
PMSF	phenylmethanesulfonylfluoride
poly I:C	polyinosinic:polycytidylic acid
PRR	pattern recognition receptor
qRT PCR	quantitative real-time PCR
RER	ribonucleotide excision repiar
RLR	RIG I-like receptors
RNase H1	Ribonuclease H1
RNase H2	Ribonuclease H2
rNTPS	ribonucleotide triphosphates
rpm	rounds per minute
RT	room temperature
SLE	Systemic Lupus Erythematosus
ssRNA	single-stranded RNA
TAE	Tris-acetate-EDTA
TBS	Tris-buffered saline
TLR	Toll-like receptor
Top I	topoisomerase I
UV light	ultravioet light
UVC	ultraviolet C
WT	wild type
Bq	bequerel
SPF	specific pathogen free

Abstract

Aicardi-Goutières syndrome (AGS) is an autosomal recessive encephalopathy with low incidence. The disease is caused by mutations in the genes encoding for TREX1, SAMHD1, ADAR, IFIH1 and the three genes encoding for the heterotrimeric RNase H2 enzyme. Biallelic mutations in any of the genes cause elevated type I interferon levels in the cerebrospinal fluid (CSF), the hallmark of AGS. In AGS patients, increased type I interferon levels cause massive inflammation in the brain that leads to mental and physical retardation that likely cause death in early childhood. AGS shows significant overlap with the prototypic autoimmune disease systemic lupus erythematosus (SLE). Like AGS patients, SLE patients are also characterized by increased type I interferon levels, anti-nuclear autoantibodies (ANAs) and arthritis. Moreover, heterozygous mutations in TREX1, SAMHD1 and RNase H2 are also found in a small fraction of SLE patients. Due to the genetic, molecular and clinical overlap, AGS is regarded as a monogenic variant of SLE. This overlap allows for the investigation of SLE pathomechanisms using genetically engineered mouse models with AGS-related mutations.

In order to generate a mouse model that allows for the identification of pathomechanisms in AGS patients with mutations in the genes encoding for the RNase H2 enzyme, we generated mice with deficiency for the RNase H2 enzyme. Mice with complete deficiency for the RNase H2 enzyme (*Rnaseh2c*$^{-/-}$ or *Rnaseh2b*$^{KOF/KOF}$) died perinatally or were stillborn. Mouse embryonic fibroblasts (MEFs) from E14.5 *Rnaseh2b*$^{KOF/KOF}$ embryos displayed impaired proliferation that was caused by the accumulation of MEF cells in G2/M of the cell cycle which increased with cultivation time or if MEF cells were isolated from E18.5 *Rnaseh2b*$^{KOF/KOF}$ embryos. Gene expression analysis of E14.5 fetal liver cells revealed a robust p53-mediated DNA damage response with the cell cycle inhibitor cyclin-dependent kinase inhibitor 1a (*Cdkn1a*, *p21*) being the most up-regulated gene. We found increased numbers of phosphorylated histone H2AX (γH2AX) in fetal liver and thymus cells from E18.5 *Rnaseh2b*$^{KOF/KOF}$ embryos, indicative of DNA double-strand breaks. Finally, we could show increased ribonucleotide loads in genomic DNA from embryos that were completely deficient for the RNase H2 enzyme. Collectively, we have demonstrated that complete RNase H2 deficiency causes persistent genomic ribonucleotide loads that render the DNA instable and prone to DNA strand breaks. DNA damage leads to the activation of p53 that in turn activates the cell cycle inhibitor p21 that inhibits cell cycle progression and likely causes accumulation of RNase H2-deficient cells in G2/M.

To bypass early lethality we also generated bone marrow chimera and cell type-specific knockouts of the *Rnaseh2b* gene. While fetal liver cells of E14.5 *Rnaseh2b*$^{KOF/KOF}$ embryos could maintain hematopoiesis of irradiated recipient mice for almost one year, bone marrow cells from these primary recipients failed to reconstitute lethally irradiated mice in a secondary transfer. In line with this observation, *VavCre*-mediated deletion of the *Rnaseh2b* gene caused a more than hundred fold reduction of peripheral blood B cells, while B cell numbers remained unaltered upon *CD19Cre*-mediated deletion that occurs much later in B cell development. These data suggested that RNase H2 deficiency leads to the accumulation of genomic ribonucleotides that might cause the accumulation of a so far uncharacterized DNA damage species with increasing cell cycle passages. The data further supported our hypothesis that the impact of RNase H2 deficiency is determined by the number of cell proliferation.

Finally, an epidermis-specific knockout of the *Rnaseh2b* gene displayed the most dramatic phenotype. Knockout mice were characterized by hyperpigmentation, hair loss and spontaneous ulcerations of the skin. Microscopically, these mice displayed moderate thickening of the epidermis and dermal fibrosis as indicated by increased collagen deposition. Macroscopic skin phenotypes were completely dependent on p53 expression, since concomitant deletion of the *p53* gene rescued mice from hyperpigmentation, hair loss and ulcerations. This data demonstrated that *Rnaseh2b* deficiency in the epidermis may also lead to DNA damage and subsequent p53 activation as shown for fetal liver from E14.5 RNase H2-deficient embryos. Preliminary data also indicate an increased incidence of cancer formation in RNase H2/p53 double knockouts, identifying the RNase H2 enzyme as an important tumor suppressor.

Zusammenfassung

Das Aicardi Goutières Syndrom (AGS) beschreibt eine sehr seltene autosomal rezessive Enzelopathie, die durch Mutationen in den Genen Trex1, Samhd1, Adar, Ifih1 sowie in allen drei Genen, die für das heterotrimere RNase H2 Enzym kodieren, hervorgerufen wird. Biallelische Mutationen in diesen Genen führen zu einer unkontrollierten Typ I Interferon Antwort und erhöhte Zytokinspiegel in der zerebrospinalen Flüssigkeit, das Hauptcharakteristikum dieser Erkrankung. Die unkontrollierte Typ I Interferon Antwort geht einher mit einer massiven Entzündung des Gehirns, die geistige und körperliche Schädigungen, als auch den frühen Kindstod zur Folge haben kann. Von besonderem Interesse ist das Aicardi Goutières Syndrom auf Grund seiner Gemeinsamkeiten mit der prototypischen Autoimmunerkrankung Systemischer Lupus Erythematodes (SLE). SLE ist wie AGS durch eine unkontrollierte Typ I Interferon Antwort, antinukleäre Autoantikörper und Arthritis charakterisiert. Außerdem werden in einem Teil der SLE Patienten heterozygote Mutationen in den Genen Trex1, Samhd1 sowie in allen drei Genen des heterotrimeren RNase H2 Enzyms gefunden. Aufgrund der klinischen, molekularen und genetischen Gemeinsamkeiten zwischen SLE und AGS, wird das Aicardi Goutières Syndrom als eine monogenetische Variante des SLE betrachtet und stellt somit ein wertvolles Werkzeug für die Entschlüsselung SLE-relevanter Pathomechanismen dar.

Für die Identifizierung von Pathomechanismen des SLE generierten wir verschiedene RNase H2-defiziente Mausmodelle. Vollständig RNase H2-defiziente Mäuse und Mäuse mit einer hypomorphen Expression des RNase H2 Enzyms verstarben allerdings in der frühen embryonalen Entwicklung (E10.5) (*Rnaseh2c*$^{-/-}$) beziehungsweise wurden tot geboren (*Rnaseh2b*$^{KOF/KOF}$). Mausembryonale Fibroblasten aus E14.5 *Rnaseh2b*$^{KOF/KOF}$ Embryonen wiesen eine reduzierte Wachstumsrate auf, welche durch die Akkumulation der Zellen in der G2/M Phase des Zellzyklus hervorgerufen wurde. Beide Phänomene zeigten eine stärkere Ausprägung mit Fortlauf der Kultur oder wenn Mausembryonale Fibroblasten aus E18.5 *Rnaseh2b*$^{KOF/KOF}$ Embryonen gewonnen wurden. Eine Microarray-basierte Genexpressionsanalyse fötaler Leberzellen von E14.5 *Rnaseh2b*$^{KOF/KOF}$ Embryonen offenbarte die verstärkte Expression p53-induzierter Gene, während das Gen *Cdkn1a* (cell cycle-dependent kinase inhibitor 1a), auch bekannt als p21, die stärkste Aufregulation zeigte. Das vermehrte Auftreten von phosphoryliertem Histon H2AX (γH2AX) in fötalen Leber- und Thymuszellen von E18.5 *Rnaseh2b*$^{KOF/KOF}$ Embryonen legte die Existenz einer DNA Schadensantwort nahe. Nachfolgende Untersuchungen konnten zeigen, dass die Abwesenheit des RNase H2 Enzyms zu einer vermehrten Akkumulierung von Ribonukleotiden in der genomischen DNA führt. Zusammenfassend weisen unsere Daten darauf hin, dass der vermehrte Einbau von Ribonukleotiden die genomische DNA

anfällig für DNA Schaden macht und dass dieser Schaden eine p53-mediierte DNA Reparaturantwort auslöst.

Um trotz der frühen Letalität RNase H2-defizienter Mäuse mögliche Pathomechnismen des SLE identifizieren zu können versuchten wir in der Folge die Letalität durch die Generierung von Knochenmarkschimären und Zelltyp-spezifischen Knockouts zu umgehen. In einem ersten Transferexperiment waren fötale Leberzellen von E14.5 *Rnaseh2b*$^{KOF/KOF}$ Embryonen vollständig kompetent letal-bestrahlte Rezipienten zu rekonstituieren. Wurde allerdings das Knochenmark dieser primären Rezipienten in letal-bestrahlte sekundäre Rezipienten transferiert, so waren RNase H2-defiziente Zellen nicht mehr in der Lage diese Tiere zu rekonstituieren. Bei der Generierung Zelltyp-spezifischer Knockouts beobachteten wir ein ähnliches Ergebnis. Während der B Zell-spezifische Knockout (CD19Cre-mediiert) des *Rnaseh2b* Gens nur einen sehr geringen Einfluß auf B Zellen hatte, so führte ein VavCre-spezifischer Knockout in der frühen hematopoietischen Stammzelle zu einer massiven Reduzierung der B Zellzahlen im peripheren Blut. Basierend auf diesen Daten vermuten wir, dass in der Abwesenheit des RNase H2 Enzyms ein unbekannter DNA-Schaden während jeder Zellteilung akkumuliert der nur eine begrenzte Anzahl von Zellzyklen erlaubt.

Wir generierten schließlich einen Epidermis-spezifischen Knockout des *Rnaseh2b* Gens. Dieser Knockout wies den dramatischsten Phänotyp auf und war makroskopisch durch Hyperpigmentation, Haarverlust und spontane Ulzerationen charakterisiert. Mikroskopisch fiel neben einer moderaten Verdickung der Epidermis, die stark veränderte Dermis auf, die eine milde Leukozyten-Infiltration, Interface Dermatitis und erhöhte Kollagenablagerungen aufwies. Die Rückkreuzung des Epidermis-spezifischen Knockouts auf einen p53-defizienten Hintergrund führte in großen Teilen zum Rückgang der Pathologie auf Wildtyp-Niveau. Präliminäre Daten zeigten außerdem, dass die gleichzeitige Abwesenheit des *p53* Gens die Bildung von kanzerogenen Gewebsveränderungen und die Tumorbildung begünstigt. Diese Daten zeigen, dass auch die Abwesenheit des RNase H2 Enzyms in der Haut zu einer p53-mediierten DNA Schadensantwort führt und dass das RNase H2 Enzym eine wichtige Rolle bei der Tumorsuppression einnimmt.

1. Introduction

1.1 The immune system

The human body is constantly exposed to a plethora of pathogens (bacteria, viruses or fungi) that pose a huge threat for the individual fitness. Inability to defend the organism against this danger would inevitably cause severe diseases or even death. The human organism is therefore well equipped with an effective protection system that guards him from invading pathogens and thus preventing the development of harmful diseases (Akira et al., 2006).

The skin represents the first line of defense by forming a physical and mechanical barrier that separates the human body from the surrounding environment (Madison, 2003; Watt, 2014). The tight organization of the epidermis in combination with the secretion of different secretes, like sweat, proteases or mucus, does not allow the penetration by invading pathogens. The second line of defense is represented by the immune system, a large protection system that is composed of cellular and soluble mediators. Thus, even once the first barrier is crossed, so due to a skin lesion that allows penetration by the pathogen, the human organism still has access to the power of the entire components of immune system. The human immune system is composed of two different protection systems that can act separately but usually act in concert to defend the human body, the innate and the adaptive immune system (Janeway and Medzhitov, 2002). The interplay of both, together with the barrier function of the skin, represents a huge wall of defense that can be hardly mounted by an invading pathogen in a healthy human organism. The maintenance of the immune system is thus of particular importance to prevent frequent pathogen infections.

The innate immune response depicts the first line of defense within the immune system (Akira et al., 2006; Kumar et al., 2011; Hoffmann and Akira, 2013). A myriad of different proteins, like acute phase proteins or components of the complement system contribute to the effective pathogen clearance. However, the cellular innate immune response is activated by the detection of so-called pathogen-associated molecular patterns (PAMPs) (Janeway and Medzhitov, 2002). PAMPs are conserved pathogen structures that do not succumb rapid evolutionary changes, as they are often indispensible for pathogen infectivity or vitality. PAMPs are detected by a huge number of germline-encoded pattern recognition receptors (PRRs) (Kawai and Akira, 2011; Broz and Monack, 2013). Another concept for the activation of the innate immune response comprises the detection of danger-associated molecular patterns (DAMPs) (Matzinger, 1994; Matzinger, 2002). In striking contrast to PAMPs, DAMPs are host-derived structures that are presented in the context of a danger signal. Necrotic cells display an important source of DAMPs, since

necrosis leads to concomitant release of endogenous proteins and nucleic acids that represent a very potent danger signal in this context. The activation of innate immune system is a very fast process, since PAMP-binding to the respective PRR can elicit the immediate release of preformed mediators or the rapid *de novo* synthesis and expression of mediators that subsequently interfere with the pathogen. Activation of the receptors of the innate immune system most commonly causes the release of pro-inflammatory cytokines and chemokines. Of particular note is the induction of a type I interferon response upon detection of non-self or mislocalized nucleic acid species that confer a potent antiviral state to the infected host. However, since the activation of PRRs causes the elicitation of a monotonous immune response, the innate immune response has to be regarded as being unspecific and in case pathogens have adopted immune evasion mechanisms (Iannello et al., 2006; Bowie and Unterholzner, 2008), the effector functions of the innate immune system are less effective. The reduced specificity of the innate immune system is partly compensated for by the strength of the innate immune response that is efficient to eliminate the pathogen but that also increases the risk of collateral damage.

Cells that display effector functions during the innate immune response belong to the myeloid lineage of the hematopoietic system. Important members are dendritic cells (DCs) and macrophages (Liu, 2001; Mellman and Steinman, 2001). Both cell types are equipped with the full set of PRR and are therefore the most important sensors of pathogen invasion. Among their various functions, they patrol through the tissue of the human body to sample for the presence of pathogenic structures. Due to their unique ability to phagocytize apoptotic and necrotic cells as well as other insoluble components, these cells take a center stage in the detection of pathogen infection and during the subsequent activation of the adaptive immune system (Fearon and Locksley, 1996; Medzhitov and Janeway, 1997; Liu, 2001). Important characteristic of DCs and macrophages is their ability to present components of the phagocytized material, the antigens, to cells of the adaptive immune system. For this reason, DCs and macrophages (and also B cells) are termed professional antigen-presenting cells (APCs). Antigen-presentation by activated APCs to T cells of the adaptive immune system leads to the activation of the adaptive immune system. In contrast to the innate immune response, the adaptive immune response is specific and effective in the clearance of the invading pathogen. But, since the adaptive immune system is activated by the innate immune system, effector functions of the adaptive immune system are exerted with a delay of some days. However, since the adaptive immune system is capable to built up an immunological memory, the adaptive immune system efficiently protects the human organism during subsequent infections. Key effector cells of the

adaptive immune system are the T cells and B cells. Their function is either to efficiently kill infected cells directly by cytotoxic T cells or to generate an antibody-mediated clearance of the infection via helper T cells and B cells.

Deregulation or defects of the immune system ultimately lead to the development of severe diseases, even in the absence of a pathogen infection. While defects in the innate immune system cause the generation of autoinflammatory diseases, defects in the adaptive immune system lead to autoimmunity. However, there are only few examples of diseases that clearly categorize to either of both types of disease. Most diseases display a combination of autoinflammation and autoimmunity, simply becuase mediators of the innate immune system often influence deregulation of the adaptive immune system. Autoimmunity is characterized by the T cell and B cell-mediated destruction of self-structures, usually prevented by several tolerance mechanisms. In case tolerance is disturbed or incomplete, T cells and B cells with self-specificity promote the generation of autoimmunity.

1.1.1 Nucleic acid sensing

Vertebrate cells are well equipped with a large set of sensors, competent to detect invading pathogens. Since these sensors detect invariant structures of the pathogen, termed pathogen-associated molecular patterns (PAMPs), the respective sensors are called pattern recognition receptors (PRRs). The large group of germline-encoded PRRs can be subdivided according to their cellular localization and most importantly, by the PAMP they are detecting. While there is only a limited number of PRRs that detect invariant surface structures of pathogens, like lipopolysaccharide (LPS) from gram-negative bacteria (TLR4) or flagellin from flagellated bacteria (TLR5), there is a huge group of PRRs that detect nucleic acid species (Medzhitov, 2007; Takeuchi and Akira, 2010). Among the PRRs that sense the presence of nucleic acids, a small number is bound to the endosomal membrane (TLR 3, 7, 8 and 9), whereas most are located in the cytoplasm. Among the large group of cytosolic PRRs only a few are solely activated by non-self nucleic acid species. However, most cytosolic PRRs can be activated by self- as well as non-self nucleic acids, but since the cytosol is usually free from endogenous nucleic acids, their activation mostly occurs in the context of a pathogen infection (Gurtler and Bowie, 2013).

The different pathogen sensors can be divided into two main groups, the Toll-like receptors (TLRs) and the Rig-like receptors (RLRs). The group of TLRs consists of ten human and 13 mouse members. TLRs are membrane-bound receptors that are either located on the cell surface or in the membrane of the endosomes, with the receptor

facing the endosomal lumen (Kawai and Akira, 2010). The group of cell surface TLRs encompasses the TLR-1, 2, 4, 5 and 6. These TLRs monitor the extracellular space and mainly sense bacterial structures (as exemplified above). The group of endosomal TLRs contains TLR-3, 7, 8, 9 and 13 (TLR-8 is absent in the mouse) characterized by the specificity for different nucleic acid species. TLR-3 detects double-stranded RNA (dsRNA), TLR-7 and TLR-8 sense single-stranded RNA (ssRNA), TLR-9 detects the unmethylated CpG motif of double-stranded DNA and TLR-13 is activated by the 23S ribosomal RNA from bacteria (Kawai and Akira, 2010; Oldenburg et al., 2012). Ligand binding to TLR-7, 8, 9 and 13 leads to the activation of the downstream molecule MyD88, while ligand binding to TLR-3 causes the activation of TRIF. However, activation of MyD88 and TRIF activates the NF-κB pathway that leads to IRF3 (interferon regulatory factor 3) activation in case of TRIF and to IRF7 activation in case of MyD88. Finally, activation of both pathways causes the induction of a type I interferon response (Kawai and Akira, 2010).

RLRs are cytosolic sensors with RNA specificity that scan the cytoplasm for nucleic acids from invading microbes. The group of RLRs consists of RIG-I (retinoic acid-inducible gene-I), MDA5 (melanoma differentiation associated gene 5) and LGP2 (laboratory of genetics and physiology 2) (Yoneyama et al., 2005; Loo and Gale, 2011). Long double-stranded RNA that is absent under physiological conditions in eukaryotic cells activates RIG-I and MDA5. While RIG-I is activated by dsRNA of about 300 bp, MDA5 prefers dsRNA longer than 4 kb (Kato et al., 2008). However, the actual RIG-I substrate is a 5` triphosphate RNA that further contains a panhandle structure (Hornung et al., 2006; Pichlmair et al., 2006; Schlee et al., 2009). A 5` triphosphate is virtually absent in eukaryotes since eukaryotic RNA (messenger RNA) possesses a 5` Cap structure that stabilizes the RNA and prevents it from being degraded. Further RIG-I substrates are 5` hydroxyl RNA and 3` monophosphoryl RNA with a double-stranded stem, a product of RNase L activity. Most recent data could show that a 5`-diphosphate can also efficiently trigger RIG-I activation (Goubau et al., 2014). An important feature of RIG-I and MDA5 is the presence of a N-terminal CARD domain (caspase activation and recruitment domain) whose repression during steady state is released upon ligand binding, allowing the oligomerization of four RIG-I molecules and subsequent activation of downstream signaling molecules (Jiang et al., 2012). The downstream adaptor molecule of RIG-I and MDA5 is the MAVS molecule (mitochondrial antiviral signaling; also known as IPS, CARDIF or VISA) that comprises an N-terminal CARD motif, necessary for the interaction of RIG-I or MDA5 and MAVS via a CARD-CARD interaction (Kawai et al., 2005; Meylan et al., 2005; Seth et al., 2005). The C-terminus of the MAVS molecule is linked to the outer mitochondrial membrane and this association was shown

to be important for subsequent signaling pathway activation. Activation of MAVS in turn leads to the activation of the cytosolic kinases TBK1 (tank binding kinase 1) and IKK (inhibitor of nuclear factor kappa). While TBK1 leads to the transcription of type I interferon genes via phosphorylation of the transcription factor IRF3, type I interferon genes and genes encoding for pro-inflammatory cytokines are activated by the transcription factor NF-κB upon IKK activation (Sun et al., 2006).

A third group of nucleic acid sensors comprises the cytosolic DNA sensors that were recently discovered and that do not display a uniform structure. Cytosolic DNA can be detected by the RNA polymerase III / RIG-I pathway (Ablasser et al., 2009; Chiu et al., 2009). Strangely, cytosolic DNA is first transcribed into dsRNA with a 5` triphosphate moiety by the RNA polymerase III, generating an ideal substrate for the RIG-I sensor. Binding of the 5` triphosphate dsRNA molecule to RIG-I leads to the activation of type I interferon genes via the adaptor molecules MAVS and TBK1, and the transcription factor IRF3. Most recently the role of the cyclic GMP/AMP synthase (cGAS) to sense cytosolic nucleic acids was elucidated (Sun et al., 2013; Wu et al., 2013). Similar to the 2`, 5`-oligoadenylate synthethase (OAS), activation of cGAS leads to the generation of a second messenger that activates the stimulator of interferon genes (STING) (Ishikawa and Barber, 2008; Zhong et al., 2008; Sun et al., 2009). Upon binding of dsDNA to cGAS, the second messenger 2`3`- cyclic GMP/AMP (cGAMP) is synthesized from the nucleotides GTP and ATP. Activation of STING leads to the expression of type I interferon genes via the adaptor molecule TBK1 and the transcription factor IRF3. Other sensors of nucleic acids are the DNA-dependent activator of IRFs (DAI), IFI16, DDX41 and AIM2 (absent in melanoma 2). While DAI, IFI16 and DDX41 seem to have redundant functions in the activation of type I interferon genes, AIM2 represents the sole cytoplasmatic DNA sensor that leads to the formation of the AIM2 inflammasome and subsequent IL-1β and IL-18 expression (Wu and Chen, 2014)

1.1.2 Type I interferon response

All mammalian cells express a large set of cytosolic nucleic acid sensors that enable them to sense pathogen infection. However, since not all cells express TLRs concomitantly, they are not able to detect the presence of pathogens in the extracellular space or sense the infection of neighboring cells. To compensate for this inability, professional antigen presenting cells (APCs), like dendritic cells (DCs), macrophages or B cells (with some minor exceptions) express the complete repertoire of PRRs and are thus capable to sample the extracellular space. Moreover, the unique property of DCs, macrophages and B cells to engulf apoptotic cells by phagocytosis allows them further to

scan these cells for the presence of viral components. As described above, nucleic acid binding to the respective PRR leads to the expression of type I interferon via different signaling pathways. De novo synthesized type I interferon is released from the cell where it binds to the interferon alpha receptor (IFNAR) in an autocrine and paracrine fashion. Today, three different types of interferon are described (type I-III). Human and mouse type I interferons encompass 13 interferon alpha (IFNα) and one single interferon beta (IFNβ) as well as interferon epsilon (IFNε), kappa (IFNκ) and omega (IFNω) (Pestka et al., 2004). Genes encoding for type I interferon genes are located on chromosome 9 in humans and on chromosome 4 in mouse (Pestka et al., 2004; Chen et al., 2004). Type II interferons encompass a single cytokine, interferon γ. The gene encoding for IFNγ is located on chromosome 12 in humans and chromosome 10 in mouse (Pestka et al., 2004). After expression of type I interferon, autocrine and paracrine effects cause an anti-viral state in the surrounding tissue (Sadler and Williams, 2008). Type I interferon binds to the type I interferon alpha receptor (IFNAR) that is located in the cell membrane of all cells of the human and mouse organism. It is composed of two subunits, IFNAR1 and IFNAR2. While IFNAR1 is associated with the tyrosine kinase 2 (TYK2), IFNAR2 is associated with the Janus activated kinase 1 (JAK1). Binding of type I interferon to the receptor causes activation of the JAK-STAT pathway (Darnell et al., 1994; Stark and Darnell, 2012). Initially, type I interferon-binding leads to the autophosphorylation and activation of TYK2 and JAK1 which subsequently mediate the phosphorylation of downstream STAT (signal transducer and activator of transcription) molecules. Upon phosphorylation, activated STAT translocates to the nucleus where it activates the expression of interferon-stimulated genes (ISGs) (Schoggins et al., 2011). Interferon-stimulated genes cause the generation of an anti-viral state, since their expression interferes at various levels with the replication cycle of the virus (Sadler and Williams, 2008).

1.2 Interferonopathies

1.2.1 Systemic lupus erythematosus (SLE)

Systemic lupus erythematosus (SLE) is a prototypic autoimmune disease that is clinically characterized by multi organ inflammation, encompassing organs like the skin or kidney. SLE pathology originates in consequence of the breakdown of self-tolerance, triggered by an unbalanced type I interferon response. Pathology is mediated by autoantibodies that are directed against nuclear self-antigens, while the site of immune complex deposition determines the organ involvement (Mok and Lau, 2003; Grammatikos and Tsokos, 2012). As many autoimmune diseases, SLE is a multi-factory disease that has a

genetic but also an environmental component (Agmon-Levin et al., 2012). Moreover, the genetic component itself is very heterogeneous and mutations in many different genes were shown to increase susceptibility to develop SLE pathology. While in rare cases SLE is caused by mutations in a single gene, most SLE patients have concomitant mutations in several genes. Moreover, some mutations in SLE patients are subclinical and need the trigger of an environmental stimulus, like UV light exposure. However, mutations alone or in combination with an environmental trigger cause an unbalanced type I interferon response that fuels the breakdown of self-tolerance. As a consequence of the breakdown, self-structures in combination with a danger-associated molecular pattern (DAMP) elicit an adaptive immune response that leads to the destruction of tissues and organs.

A well-accepted model for SLE pathology is defined by the defective clearance of apoptotic and necrotic cells. Apoptosis describes the programmed cell death during diverse biological processes like tissue differentiation or pathogen defense. Programmed cell death can be activated by an intrinsic or extrinsic pathway, but both lead to the cleavage of several proteins and the fragmentation of the DNA. Since membrane integrity is maintained during apoptosis, it can be regarded as an immunologic 'silent' process that does not trigger an immune response. However, apoptotic cells need to be cleared by professional phagocytizing cells like macrophages or dendritic cells to prevent inflammation. Therefore, apoptotic cells secrete a "find me" signal to attract phagocytes and express an "eat me" signal in order to be phagocytized (Ravichandran and Lorenz, 2007). In contrast to apoptosis, membrane integrity is not maintained during necrosis. Necrosis can be subdivided into primary and secondary necrosis, depending on the type of membrane disintegrity. Primary necrosis is a consequence of physical or chemical insults, while secondary necrosis can be observed in undegraded apoptotic cells that progressively loose membrane integrity (Poon et al., 2014). However, necrosis causes the release of cytoplasmic and nuclear components that might stimulate an immune response due to their strong immunogenicity. Of particular importance is thus the immediate degradation of nucleic acid species originating from the nucleus in order to prevent the activation of nucleic acid sensors that would inevitably cause the initiation of a type I interferon response. Thus, many SLE patients bear mutations in the genes encoding for proteins that play an important role in the degradation of dying cells. Among those, the important member of the complement system C1q is found to be mutated. C1q labels dying cells for the efficient degradation by macrophages. Deficiency for the C1q prevents phagocytosis and leads to the accumulation cell components like various types of nucleic acids that subsequently sensors and the induction of a type I interferon response. Deficiency for the desoxyribonuclease I (DNase I) (Chitrabamrung et al.,

1981) and three prime repair exonuclease 1 (Trex1) (Lee-Kirsch et al., 2007) was also observed in human SLE patients. While DNase I plays an important role in the degradation of double-stranded DNA in the serum, Trex1 is supposed to degrade single-stranded DNA in the cytoplasm and maybe nucleus.

As a consequence of the defective clearance of dying cells, nucleic acid species trigger an unbalanced type I interferon response that supports the generation of an adaptive immune response directed against self peptides that are concomitantly released from dying cells. Complexes of nucleic acids and associated nuclear structures, like centromeres or histones, are thought to represent a potent stimulator for the generation of the adaptive immune response. The synthesis of antibodies directed against these structures might occur in autoreactive B cells in a T cell-independent fashion. Binding of the protein component to the membrane-bound B cell receptor provides the first signal for B cell activation and leads to its internalization and the compartmentalization in endosomes. Subsequent binding of the nucleic acid component to the respective toll-like receptor (TLR) in the endosome provides the second important signal for B cell activation and subsequent synthesis of autoantibodies (Leadbetter et al., 2002). SLE pathology is caused by the deposition of immune complexes consisting of the autoantibody and the respective antigen. Since autoantibodies in SLE are directed against nuclear antigens, immune complexes can only form after the disintegrity of the cellular membrane and the release of nuclear antigens. The inability to clear apoptotic and necrotic cells could lead to the chronic deposition of complexes. However, UV light exposure can also trigger SLE pathology by causing increased rates of apoptotic and necrotic cells. Immune complexes can cause organ failure by their deposition that block organ failure or by an immune response (antibody-dependent cellular cytotoxicity, ADCC) stimulated by the presence of the immune complexes. Local immune complex deposition in the skin or the kidney can cause organ failure, while systemic immune complex deposition might cause death.

1.2.2 Aicardi Goutières Syndrome (AGS)

In 1984, Jean Aicardi and Françoise Goutières were the first to describe a so far unknown disorder of the central nervous system in young children (Aicardi and Goutieres, 1984). They examined eight children of unrelated or consanguieous parents and diagnosed calcifications in the basal ganglia, brain atrophy, acquired microcephaly, elevated numbers of lymphocytes in the cerebrospinal fluid (CSF) and lethality in early childhood. Although the brain calcifications were highly reminiscent of that seen in congenital virus infections, Aicardi and Goutières stated already at that point that the calcification neither derived from virus infection nor from a rare syndrome of familial

calcifications or familial idiopathic hypoparathyroidism. They proposed that the reported cases might belong to a so far unknown or uncharacterized disorder that is inherited in an autosomal recessive Mendelian fashion.

At present, the Aicardi-Goutières syndrome (AGS) is defined as an early-onset encephalopathy that is characterized by calcifications of the basal ganglia, brain atrophy, lymphocytosis and increased type I interferon levels in the CSF. The consequences of AHS are physical and mental retardation and often death in early childhood. Elevated type I interferon levels were first described by Lebon et al. (Lebon et al., 1988) and are now regarded as the hallmark of Aicardi-Goutières syndrome. Importantly, in patients suffering from the disorder, no virus infection can be found at any given time point that can account for the neurological and extra-neurological findings (Crow and Livingston, 2008).

The Aicardi-Goutières syndrome is a heterogeneous disease that can be caused by mutations in at least seven genes. The first AGS-causing gene locus (AGS1) was identified in 2006 by Crow et al., being the 3`- 5` repair exonuclease 1 (TREX1) (Crow et al., 2006a). Thereafter, mutations in any of the three subunits of the ribonuclease H2 (RNase H2A, RNase H2B and RNase H2C) (AGS4, AGS2 and AGS3, respectively) (Crow et al., 2006b) and in the sterile alpha motif and HD domain containing protein 1 (SAMHD1; AGS5) (Rice et al., 2009) were found in AGS patients. Most recently, mutations in the adenosine deaminase acting on RNA (ADAR; AGS6) (Rice et al., 2012) as well as in IFIH1 (melanoma differentiation-associated protein 5, MDA5; AGS7) (Rice et al., 2014) were found in patients suffering from AGS. While mutations in the genes AGS1-6 cause a partial loss-of-function, mutations in AGS7 create a gain-of-function. Still, there is the possibility that there are even more AGS-causing genes and it might be feasible to speculate that any mutation that causes the generation of an unbalanced type I interferon response could cause the development of AGS pathology. However, the current hypothesis is that the accumulation of nucleic acid species in patients deficient for any of the five proteins leads to the elicitation of a type I interferon response that triggers AGS pathology (Alarcon-Riquelme, 2006; Rigby et al., 2008; Crow and Rehwinkel, 2009). Mutations in IFIH1 are not supposed to lead to the accumulation of nucleic acid species, however, mutations cause chronic type I interferon expression independent of an accumulating nucleic acid species and important for the development of the disorder. TREX1, RNase H2, SAMHD1 and ADAR are enzymes with specificity for different nucleic acid substrates. TREX1 degrades single-stranded and double-stranded cytosolic DNA (Stetson et al., 2008; Ablasser et al., 2014), RNase H2 degrades the RNA moiety in RNA:DNA hybrids or removes a single ribonucleotide embedded in DNA duplex (Eder et al., 1993; Rydberg and Game, 2002; Cerritelli and Crouch, 2009) while

SAMHD1 is a desoxynucleoside triphosphate triphosphohydrolase that degrades endogenous nucleotides and thus has essential functions during HIV-1 restriction (Goldstone et al., 2011). More important, SAMHD1 displays nuclease activity with specificity for RNA (Ryoo et al., 2014). Adar deaminates adenosine to inosine in double-stranded RNA that likely changes the RNA information as well as the structure that could inhibit RNA translation. The origin of the nucleic acid species that accumulate in the absence of TREX1, RNase H2, SAMHD1 and ADAR are so far unknown. It is speculated that the nucleic acid might be generated as byproducts of DNA replication or repair (Lan et al., 2014) or derive from the transposition activity of endogenous retroelements (Stetson et al., 2008; Beck-Engeser et al., 2011) The exception of this hypothesis is displayed by the gain-of-function mutations in the *IFIH1* gene, encoding for the sensor of long double-stranded RNA. Two mutations were so far described, one that causes the constitutive activity of the receptor and another that reduces the specificity for the receptor ligand (Funabiki et al., 2014; Rice et al., 2014). However, both mutations cause type I interferon expression.

Aicardi-Goutières syndrome is inherited as an autosomal recessive disorder. Thus, AGS patients mostly display homozygous mutations. However, compound heterozygous mutations can be found in patients with mutations in TREX1. Moreover, there are also two reports of *de novo* heterozygous TREX1 mutations that caused AGS. Both mutations were found to be an amino acid substitution affecting the same amino acid (D200N and D200H), indicating the important role of this amino acid in the nuclease function of Trex1 (Rice et al., 2007). Mutations in the *TREX1* gene and the genes encoding for RNase H2 differ substantially, from a genetical but also from a phenotypical perspective (Rice et al., 2007). While null mutations (frameshift, nonsense mutations or mutations affecting splice-donor and splice-acceptor sites) can be observed in AGS patients with mutations in TREX1, null mutations have never been observed in AGS patients with mutations in the genes encoding for the RNase H2 enzyme. Since these AGS patients only display missense mutations, like amino acid substitutions, complete RNase H2 deficiency in humans likely causes embryonic lethality. Patients with mutations in the TREX1 gene display a neonatal form of AGS disease, while all other AGS patients display an early-onset form of the disease. These patients display AGS pathology few days after birth, most often after a period of normal growth normal growth. Most remarkably, a late-onset form of the disease characterizes AGS patients with mutations in the *RNASEH2B* gene. Patients with mutations in the *RNASEH2B* gene display pathology after normal growth of up to one year. In contrast to most other AGS patients, these patients do not display severe physical and mental retardation and

lethality is less frequent. Recently, patients with compound heterozygous mutations in SAMHD1 were also described to show a less severe phenotype.
Comparison of SLE patients and AGS patients revealed a phenotypical overlap between both disorders (Ramantani et al., 2010). Most importantly, SLE and AGS cluster to the family of diseases that are called interferonopathies, since pathology in both diseases is mediated by an unbalanced type I interferon (Crow, 2011; Crow, 2014). Moreover, about 40 % of AGS patients display cold-induced chilblain-like skin lesions that can also be found in a small fraction of SLE patients. A recent publication demonstrated even more common features of both disorders. Clinical common features were the lupus rash of the skin, oral ulcers and arthritis. Molecular features were anti nuclear antibodies ANAs, decreased complement levels, thrombocytopenia and leukocytopenia. Based on the molecular and phenotypic overlap, the Aicardi Goutières syndrome is now regarded as a monogenic variant of the systemic lupus erythematosus. AGS mouse models might therefore represent a versatile tool that allows for the elucidation of the pathomechanism in SLE disease.

1.3 Ribonucleases H

Ribonucleases H (RNase H) are small enzymes with RNA-specificity that can be found in all living organisms (Dirksen and Crouch, 1981; Frank et al., 1998). So far two RNase H molecules were described in eukaryotes, termed RNase H1 and RNase H2 that differ in their substrate specificity (Cerritelli and Crouch, 2009). While both enzymes can cleave the RNA moiety in RNA:DNA hybrids, RNase H1 is only capable to cleave at positions of at least four consecutive ribonucleotides in a DNA duplex (Eder and Walder 1999), whereas RNase H2 is competent to cleave even a single ribonucleotide embedded in a DNA duplex (Rydberg and Game, 2002). Three RNase H molecules can be found in prokaryotes, RNase HI-III. RNase HI and RNase HII show similar substrate specificity compared to the eukaryotic enzymes, while RNase HIII displays the same substrate specificity like RNase HI.

1.3.1 Ribonuclease H1

Human RNase H1 is a monomeric nuclease that is encoded by the *RNASEH1* gene on chromosome 2. It is a 32 kDa (32.200 kDa) protein consisting of 286 amino acids. The murine RNase H1 enzyme is a 32 kDa (31.805 kDa) protein that consists of 285 amino acids, encoded by the *Rnaseh1* gene on mouse chromosome 12. The typical organization of the eukaryotic RNase H1 enzyme consists of a N-terminal mitochondrial target sequence (MTS), followed by a hybrid binding domain (HBD), a connection domain (CD)

and a C-terminal RNase H domain (H domain) (Fig.1.1) (Cerritelli and Crouch, 2009). The N- as well as the C-terminus of the RNase H1 enzyme contains highly conserved regions encompassing the hybrid binding domain (N-terminus) and the RNase H domain (C-terminus), indicating their important role for RNase H1 activity. The hybrid binding domain of the enzyme was shown to be important for the processive hydrolysis of the RNA:DNA substrate by the RNase H1 domain, as HBD-deficient RNase H1 from human and mouse cleaved RNA:DNA hybrids in a distributive manner. Mutations in the amino acids W43, K59 and K60 in human RNase H1 were also shown to reduce binding capacity and subsequent reduced cleavage efficiency (Cerritelli and Crouch, 2009). The messenger RNA (mRNA) of the RNase H1 transcript is characterized by two in-frame start codons. Translation from the first start codon includes the MTS domain leading to the mitochondrial localization of the RNase H1 enzyme, while translation from the second excludes the MTS domain causing the retention of the protein in the nucleus (Cerritelli et al., 2003; Cerritelli and Crouch, 2009; Suzuki et al., 2010) While human and mouse RNase H1 transcripts contain a MTS domain, transcripts from *Saccharomyces cerevisiae* (*S. cerevisiae*) and *Caenorhabditis elegans* (*C. elegans*) are deficient for the domain. However, deficiency for mitochondrial RNase H1 in these organisms is compensated by other mechanisms (Cerritelli and Crouch, 2009).

Figure 1.1: General composition of the RNase H1 enzyme. The RNase H1 enzyme is composed of four domains, encompassing the mitochondrial target sequence (MTS), the hybrid binding domain (HBD), the cluster domain (CD) and the RNase H domain (H-Domain). Due to the absence of the MTS domain in *S. cerevisiae* and *C. elegans*, RNase H1 deficiency does not cause lethality as in RNase H1-deficient mice. Adopted from "RNase H, the enzymes in eukaryotes" **(Cerritelli and Crouch, 2009)**.

Deficiency for the RNase H1 enzyme in the yeast strain Saccharomyces cerevisiae (S. cerevisiae) did not have any impact on cell viability, but RNase H1-deficient yeast displayed increased sensitivity upon treatment with the alkylating agent EMS (ethyl methanesulfonate), while sensitivity towards hydroxy urea (HU) and caffeine remained mostly unaltered (Arudchandran et al., 2000). Experiments could further show that in the absence of the RNase H1 enzyme, RNase H2 expression was up-regulated, most likely in order to compensate for the RNase H1 deficiency in degrading the RNA moiety of RNA:DNA hybrids (Arudchandran et al., 2000). However, mice deficient for the RNase H1 (*Rnaseh1*$^{-/-}$) enzyme are embryonic lethal and display developmental arrest at embryonic day 8.5 (E8.5) (Cerritelli et al., 2003). *Rnaseh1*$^{-/-}$ mice are characterized by reduced

mitochondrial DNA content followed by increased apoptosis. Thus, RNase H1 plays an important role during the replication of the mitochondrial DNA (mtDNA), most likely by removing ribonucleotides inserted into the genomic DNA during replication. Due to the absence of the MTS domain in *S. cerevisiae* RNase H1, RNase H1 is not located in mitochondria of this organism and might be compensated by other proteins. Thus, RNase H1 deficiency in yeast does not display the same severe phenotype as observed in RNase H1-deficient mice (Arudchandran et al., 2000).

1.3.2 Ribonuclease H2

In contrast to the RNase HII enzyme from prokaryotes, eukaryotic RNase H2 is a heterotrimeric enzyme consisting of the subunits A, B and C that are encoded on different chromosomes of the respective organism (Frank et al., 1998; Jeong et al., 2004). The human RNase H2 consists of the 299-amino acid RNase H2A (Chr. 19; 33.400 kDa), the 308-amino acid RNase H2B (Chr. 13; 34.800 kDa) and the 164-amino acid RNase H2C (Chr. 11; 17.800 kDa) proteins, whereas the mouse RNase H2 consists of the 301-amino acid RNase H2A (Chr. 8, 33.513 kDa), the 308-amino acid RNase H2B (Chr. 14; 34.725 kDa) and the 166-amino acid RNase H2C (Chr19; 17.823 kDa) subunit. The heterotrimeric RNase H2 complex in human and mouse displays an elongated arrangement with the RNase H2C subunit located in the middle of the complex (Fig. 1.1) (Figiel et al., 2011; Reijns et al., 2011). The central RNase H2C subunit interfaces with the N-terminus of the RNase H2B subunit and the C-terminus of the RNase H2A subunit. The RNase H2A subunit possesses the active site that mediates hydrolysis of ribonucleotides embedded in DNA. The B and C subunit of the RNase H2 enzyme are supposed to have mainly structural and stability functions. Whereas the heterotrimeric RNase H2 enzyme in eukaryotes display processive cleavage, the prokaryotic, monomeric RNase HII enzyme display distributive cleavage, indicating that the B and C subunit may contribute to the processivity of the enzyme. The B subunit of the RNase H2 enzyme further contains a nuclear localization sequence (NLS) as well as a PIP (PCNA-interacting peptide)-box, a classical PCNA (proliferating cell nuclear antigen) binding motif (Bubeck et al., 2011). After its synthesis, RNase H2C first interweaves with RNase H2B before the complex consisting of the B and C subunit interfaces with the A subunit and the heterotrimeric complex is shuttled to the nucleus. However, since the A subunit is insoluble in the absence of the complex of the B and C subunit, the expression of the B and C subunit determine the generation of the RNase H2 enzyme complex (Chon et al., 2009). Moreover, all three subunits are necessary for enzyme activity (Chon et al., 2009; Reijns et al., 2011). Although RNase H1 and RNase H2 share the common feature of degrading

the RNA moiety in RNA:DNA hybrids, only the RNase H2 enzyme is capable to cleave a single ribonucleotide in a DNA duplex.

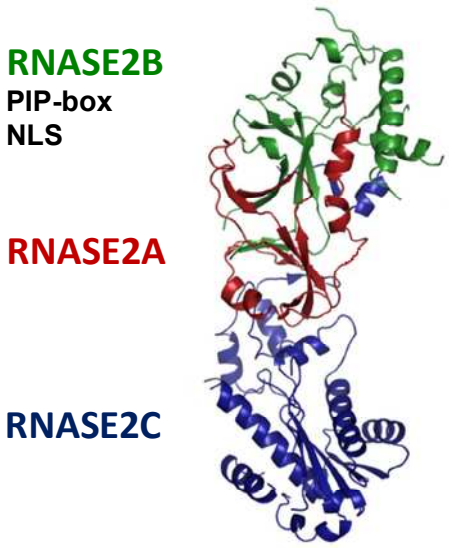

Figure 1.2: Chrystal structure of the heterotrimeric RNase H2 enzme. Ribbon diagram reveals linear orientation of the three subunits composing the heterotrimeric complex. The RNase H2A subunit forms the center of the RNase H2 complex and is enframed by the B subunit (green) and C subunit (blue). While the A subunit possesses the catalytic center, the B and C subunit are supposed to contribute to the stability and processivity of the enzyme. The B subunit further contains a nuclear localization sequence (NLS) that directs the complex to the cell nucleus and a PIP-box that allows interaction with PCNA. Adopted from Reijns et al. (Reijns et al., 2011)

Deficiency for the RNase H2 enzyme in *S. cerevisiae* was shown to have no consequence on cell viability. RNase H2-deficient cells become modestly sensitive upon treatment with HU or EMS but remain unaffected upon caffeine treatment (Arudchandran et al., 2000). Mutations in the human RNase H2 enzyme have also been described in the type I interferonopathies Aicardi-Goutières syndrome (AGS) and systemic lupus erythematosus (SLE) (Crow et al., 2006b; Crow, 2011; Crow, 2014; Günther et al., 2015). In patients suffering from AGS, mutations in the genes encoding for the RNase H2 enzyme are found to be homozygous. All mutations are described to be missense mutations that cause reduced enzyme activity only in some cases (G37S mutation in the RNase H2A subunit) (Perrino et al., 2009; Reijns et al., 2011). The consequences for most other mutations are still not understood. However, since null mutations have never been observed in AGS patients, complete deficiency likely cause embryonic lethality (Rice et al., 2007). While mutations in the genes encoding for the RNase H2 enzyme are found to be homozygous, mutations in SLE patients are found to be heterozygous non-synonymous and splice site

mutations (Günther et al., 2015). Mutations in SLE patients were shown to cause impaired enzyme activity, reduced complex stability or even mislocalization (Günther et al. 2015). Heterozygous mutations in SLE patients cause the accumulation of genomic ribonucleotides that initiates a p53-mediated DNA damage response and impaired cell proliferation. Additionally, exogenous stimulation of patients` cells with UVC and poly I:C caused a more persistent type I interferon response when compared to cells from healthy patients, indicating increased sensitivity of these cells to produce type I interferon.

1.3.2.1 Ribonucleotide excision repair (RER)

Mouse data has shown that in the absence of the RNase H2 enzyme one ribonucleotide is incorporated every 7600 nucleotides (nt) causing an overall ribonucleotide load of about one million per mouse genome during a single round of replication (Reijns et al., 2012). Therefore, the persistence of ribonucleotides represents the most frequent mutation of the DNA and causes a massive threat for the genomic information, since genomic ribonucleotides render the DNA sensitive for cleavage. In eukaryotes, ribonucleotides are efficiently removed by the concerted activity of the RNase H2 (RNH201 in yeast) and the Flap endonuclease 1 (FEN-1) (RAD27 in yeast) enzyme (Eder et al., 1993; Rydberg and Game, 2002; Cerritelli and Crouch, 2009). Early in vitro-studies using human and yeast cell-free extracts have shown that the RNase H2 enzyme incises the DNA backbone 5-prime of the incorporated ribonucleotide and subsequent cleavage of the FEN-1 enzyme 3-prime of the ribonucleotide leads to the formation of a gap that can be perfectly sealed by human DNA polymerase β and DNA ligase III in association with XRCC1 (Rydberg and Game, 2002). In contrast to RNase H2, RNase H1 is not capable to cleave at positions of single ribonucleotides in double-stranded DNA and needs at least four succeeding ribonucleotides for cleavage (Rydberg and Game, 2002; Cerritelli and Crouch, 2009). Therefore, RNase H1 cannot compensate for RNase H2 deficiency to remove single ribonucleotides from the DNA. In contrast, Exo1 could replace FEN-1, although FEN-1 showed a more than twofold efficiency. Due to the PIP box in the B subunit of the RNase H2 enzyme, RNase H2 was thought to localize at places of DNA replication and repair via PCNA. Structural analysis could confirm the interaction between both concluding that PCNA directs RNase H2 on DNA replication and DNA repair substrates (Bubeck et al., 2011). RNase H2, FEN-1, DNA polymerase δ and DNA ligase I from S. cerevisiae all contain a PIP box allowing for the interaction with PCNA. While PCNA greatly stimulated ribonucleotide excision repair, repair was independent of the PIP box, since deletion did not alter RER efficiency (Sparks et al. 2012). This data shows that the interaction of the RNase H2 enzyme via the PIP box is dispensable for RER.

1.3.2.2 Ribonuclease activity of DNA topoisomerase I

DNA topoisomerases are enzymes with important functions in relieving torsional stress as a consequence of DNA replication and transcription (Vos et al., 2011). DNA topoisomerases can be divided into two main groups, but all share the common feature of a nucleophilic tyrosine in the active site that initiates the transesterification reaction by attacking a phosphodiester bond of the DNA. While type I topoisomerases cleave a single DNA strand, type II topoisomerases are capable to cleave both strands of the DNA. Of particular importance are the type IB topoisomerases (swivelases) that nick one strand to allow the rotation of the single strand around the other and thereby facilitating relaxation. In a first transesterification reaction, the reactive hydroxyl-group of the topoisomerase IB attacks the phosphodiester bond of the DNA strand, causing the formation of a covalent complex of the topoisomerase and the DNA via a 3`-phosphotyrosyl bond. In this conformation, rotation and relaxation can occur. In a second transesterification reaction, the hydroxyl-group attacks the phosphodiester bond of the topoisomerase I-DNA complex in order to release the topoisomerase I enzyme and to re-ligate the nicked DNA strand.

Beside the above function, Sekiguchi et al. showed in 1997 that topoisomerase IB from vaccinia and humans displays also ribonuclease activity and catalyzes the site-specific cleavage of a ribonucleotide embedded in a DNA:DNA duplex (Sekiguchi and Shuman, 1997). They could show that cleavage proceeds via two transesterification reactions leading to a cleavage product containing a 2`, 3`cyclic phosphate and 5`-OH terminus. In a first step, the active site tyrosine of topoisomerase IB attacks the scissile phosphodiester, forming an intermediate, with the topoisomerase IB covalently linked to the ribonucleotide via a 3`- phosphotyrosyl bond. In a second step, this 3`- phosphotyrosyl bond is attacked by the 2`- OH of the ribose that causes the release of the topoisomerase and leading to a 2`, 3` cyclic phosphate end as well as a 5`-OH group at the other side of the nick. Moreover, they could demonstrate that a single ribonucleotide embedded in a DNA:DNA duplex is sufficient to initiate ribonuclease activity of the topoisomerase IB. Studies using a RNase H2-deficient yeast strain (*rnh201Δ*) showed increased ribonucleotide levels in the genomic DNA that were even more increased when wild type DNA polymerase ε was replaced by a mutated DNA polymerase (*pol2-M664G*) (Nick McElhinny et al., 2010). A *pol2-M644G rnh201Δ* yeast strain was characterized by slow progression through the S phase and G2/M of the cell cycle, increased desoxyribonucleotide (dNTP) levels and 2- to 5-bp deletions in repetitive sequences (McElhinny et al. 2010). However, the 2- to 5-bp deletions were subsequently shown to be completely dependent on topoisomerase I, since concomitant deletion of the

topoisomerase I gene (*top1*), reverted the numbers of deletions to wild type levels (Kim et al., 2011).

As a consequence of topoisomerase I-mediated cleavage at positions of embedded ribonucleotides 2`, 3`- cyclic phosphate ends are formed that cannot be ligated. During the repair process of 2`, 3`- cyclic phosphate ends, unligatable DNA ends are processed causing the formation of a gap that facilitates misalignment in repetitive sequences followed by ligation and subsequent deletion of DNA sequence. In addition, activation of the S phase checkpoint as well as increased dNTP levels were also shown to be dependent on topoisomerase I cleavage, since a *pol2-M644G rnh201Δ top1Δ* yeast strain displayed reduced cell numbers in G2/M and lower dNTP levels. Collectively, absence of the ribonuclease H2 in yeast causes increased genomic ribonucleotide levels that are in part removed by the ribonuclease activity of the topoisomerase. It was shown that topoisomerase I cleavage causes the generation of unligatable 2`, 3` cyclic phosphate ends that leads to the formation of 2- to 5-bp deletions, increased dNTP levels and S phase checkpoint activation. Therefore, topoisomerase I cleavage represents an imperfect mechanism to remove genomic ribonucleotides.

1.3.2.3 Ribonucleotide incorporation into genomic DNA

The maintenance of genome integrity is of particular importance in order to allow healthy life of subsequent generations. Therefore, several mechanisms have been evolved to prevent the generation, accumulation and propagation of mutations in the genomic information. Among the various assaults that might cause mutations of the DNA sequence, the incorporation of ribonucleotides into the genomic DNA represents the biggest threat for the maintenance of the genomic information, since the presence of genomic ribonucleotides renders the DNA double-strand susceptible to DNA cleavage. Ribonucleotide incorporation represents the most frequent DNA lesion and occurs in consequence of the essential cellular processes of DNA replication and transcription. RNase H2 activity takes center stage during these processes since it was shown to efficiently remove incorporated ribonucleotides and thus maintaining genome stability.

1.3.2.3.1 Frequent ribonucleotide incorporation during DNA replication

DNA polymerases display high fidelity in discriminating ribonucleotides from their incorporation into the DNA double-strand during DNA replication (Joyce, 1997). Their preference for desoxyribonucleotides is accomplished by the presence of a bulky amino acid (mostly phenylalanine or tyrosine) that builds a steric gate in the active site of DNA polymerases. This steric gate allows the integration of desoxyribonucleotides while it

would clash with bigger substrates. Ribonucleotides differ from desoxyribonucleotides by the presence of a hydroxyl group at the C_2 atom of the sugar ring that renders the ribonucleotide too bulky to enter the DNA polymerases` active site. However, frequent incorporation of ribonucleotides can be observed *in vivo* and *in vitro*, despite the high fidelity of DNA polymerases. One reason is the different stringency of DNA polymerases to discriminate ribonucleotides (Joyce, 1997) that can be even more shifted in the presence of different cofactors. Eukaryotic replication of the genomic DNA is managed by three B family polymerases, Pol α, δ and ε. While polymerase ε copies the leading strand, polymerase α and δ are involved in lagging strand DNA synthesis. Due to the deficiency of a proofreading exonuclease, polymerase α is much more inaccurate and less processive than the other polymerases and its likely function is to initiate lagging strand synthesis that is continued by polymerase δ. Data from *S. cerevisiae* has shown that polymerase α displays the highest frequency of ribonucleotide incorporation (1/625) followed by polymerase ε (1/1250) and polymerase δ (1/5000) (Williams and Kunkel, 2014). Collectively, replication of the genomic DNA by the activity the three eukaryotic polymerases cause the integration of about 14000 ribonucleotides into the yeast genome during a single generation. Extrapolating this value to the human genome would lead to the integration of more than two or three million ribonucleotides during a single round of replication (Williams and Kunkel, 2014). The other reason for the frequent integration of ribonucleotides is the high concentration of ribonucleotides in the cell that exceeds the concentration of desoxyribonucleotides (Traut, 1994; Nick McElhinny et al., 2010). This ratio is even more shifted to increased ribonucleotide concentrations in post-mitotic cells in which the cellular dNTPs are reduced. Finally, the availability of the four different dNTPs changes during the cell cycle (Chabes et al., 2003), increasing the probability of the integration of a certain ribonucleotide during a certain phase of the cell cycle. This difference in concentration levels in different phases of the cell cycle or different cell states renders the discrimination between desoxyribonucleotides and ribonucleotides imperfect.

1.3.2.3.2 Initiation of lagging strand synthesis by RNA primers

Replication of the leading DNA strand is a continuous process, since DNA polymerases are competent to replicate the template DNA in 5` to 3` direction while the replication fork migrates along the double-stranded DNA. In very contrast to leading strand synthesis, replication of the lagging strand is a discontinuous process due to the inability of DNA polymerases to replicate DNA in a 3` to 5` direction. To replicate the lagging strand of the DNA, DNA polymerases require short nucleotide-primers as initiation start for replication in 5` to 3` direction. In eukaryotes, these primers are oligonucleotides consisting of 7-14

ribonucleotides synthesized by the enzyme primase, a subunit of the DNA polymerase α (Kuchta and Stengel 2010). The newly synthesized DNA fragments between two RNA primers is termed Okazaki fragment and encompasses about 200 to 300 nucleotides. Estimations amount the number of ribonucleotides that are incorporated into the genomic DNA as a consequence of lagging strand synthesis to about 150 million (Williams and Kunkel, 2014). Therefore, lagging strand synthesis represents by far the biggest source of ribonucleotide incorporation. However, since the DNA is exclusively made of desoxyribonucleotides, ribonucleotides of the RNA primer have to be removed. Due to their ribonucleotide-specificity, the RNase H endonucleases were supposed to play an important role in the removal of the RNA primers. Using model substrates, several authors could demonstrate that the RNase H2 enzyme together with the flap endonuclease 1 (FEN-1) removes RNA-primers for the initiation of lagging strand synthesis. In this process, RNase H2 degrades the RNA primer leaving a single ribonucleotide attached 5-prime to the subsequent Okazaki fragment. This product is an ideal substrate of the Okazaki fragment maturation system encompassing the FEN-1 enzyme that cuts 3`-prime of the ribonucleotide while the replication fork migrates along the unwinding DNA double-strand.

1.3.2.3.3 R loops as transcriptional byproducts

Unwinding of the DNA double helix is necessary to allow RNA transcription, a process in which the RNA polymerase complex moves along the coding DNA strand in order to transcribe the genetic information into a messenger RNA transcript that is later translated into a polypeptide. During transcription, a hybrid of eight base pairs (bp), consisting of the nascent RNA transcript and the template DNA, is formed within the transcription bubble (Nudler et al., 1997). This interaction is immediately resolved and two separated exit channels for the RNA transcript and the reforming DNA double-strand in the RNA polymerase complex prevent the formation of hybrid structures (Westover et al., 2004). However, there is emerging evidence that the nascent RNA strand can invade the DNA strands outside the RNA polymerase complex before the DNA double-strand winds up again. This model for the formation of a three-stranded nucleic acid structure, termed the R loop, is called the “thread back” model (Roy et al., 2008). In contrast to the “thread back” model, there is also the probability that R loops are constantly formed by the extension of the eight base pair RNA:DNA hybrid in the transcription bubble while the RNA polymerase complex moves further along the DNA (Aguilera and Garcia-Muse, 2012). RNA:DNA hybrids in R loops are more stable compared to double stranded DNA (dsDNA) (Roberts and Crothers, 1992), indicating the importance to prevent their

formation or to efficiently resolve these structures in order to avoid detrimental consequences. Factors that positively influence the formation of R loops are a high GC-content, DNA supercoiling and DNA strand breaks (Roy and Lieber, 2009; Roy et al., 2010).

The current opinion is that R loop formation promotes genome instability. Displacement of the non-coding DNA strand by the nascent RNA transcript is believed to render the unpaired strand susceptible to DNA lesions and transcription-associated mutagenesis (TAM) or transcription-associated recombination (TAR) (Skourti-Stathaki and Proudfoot, 2014). The precise mechanisms that account for the generation of DNA damage upon R loop formation are only poorly understood. Important insights came from the mechanism of class switch recombination (CSR), an important event during the development of adaptive immune responses against pathogens. Increased transcription of GC-rich switch regions leads to the formation of R loops, where the nascent RNA transcript displaces the complementary DNA strand to form a RNA:DNA hybrid. The activation-induced cytidine deaminase (AID) subsequently catalyzes the deamination of cytidine to uracil in the displaced DNA strand and repair processes cause the generation of double-strand breaks that are necessary for CSR (Xu et al., 2012). According to the mechanisms during R loop-mediated class switch recombination, non-beneficial R loop formation might also go along with genetic modifications of the unpaired DNA strand. However, these processes are not well understood so far. More importantly, R loops can induce genome instability by blocking replication folk progression. Results of R loop formation are replication folk collapse, recombination and chromosomal breaks. Again, the exact mechanisms that cause genome instability in consequence of replication folk collapse are still to be defined.

However, R loops adopt an intermediate conformation between the B form of dsDNA and the A form of double stranded RNA (dsRNA) (Shaw and Arya, 2008). This special conformation might allow for the identification of R loops and their subsequent removal. Beside the efficient clearance of the R loop by the ribonucleases H1 and H2 that both degrade the RNA moiety in the RNA:DNA hybrid, other mechanisms contribute to the prevention of R loop formation. Topoisomerases relax the supercoiled DNA strand in front of the transcription machinery in order to prevent interaction between RNA transcript and the DNA double-strand. Moreover, other helicases, like the DNA helicase Pif1, the RNA helicase DHX9 and Sen1, are competent to degrade RNA:DNA hybrids (Aguilera and Garcia-Muse, 2012).

1.3.2.4 Benefits of ribonucleotide incorporation

Complete deficiency for the RNase H2 enzyme was shown to cause early embryonic lethality in mouse and human, whereas RNase H2 deficiency does not have any impact on the viability of the yeast S. cerevisiae. Homozygous loss-of-function mutations in the genes encoding for the RNase H2 enzyme that reduce enzyme activity cause the rare recessive encephalopathy Aicardi-Goutieres Syndrome (AGS), whereas heterozygous mutations are associated with the common autoimmune disease Systemic Lupus Erythematosus (SLE). Both diseases are characterized by bad prognosis, leading to early mortality in particular in case of AGS. Due to these consequences of RNase H2 deficiency, accumulation of ribonucleotides in the genome of mammalian organisms was believed to have detrimental effects. However, recent data likely demonstrated that ribonucleotide incorporation might also have a beneficial impact (Potenski and Klein, 2014; Williams and Kunkel, 2014).

Mismatch repair (MMR) of misincorporated desoxyribonucleotides requires the targeting of the MMR machinery to the nascent DNA strand and strand discontinuities are needed to serve as initiation start. Gaps between Okazaki fragments were supposed to target to the nascent DNA to the lagging strand and concomitantly serve as inititation start for MMR (Claverys and Lacks, 1986). Subsequent studies have shown that exonuclease 1 (EXO1) can interact with PCNA allowing for the introduction of additional strand discontinuities (Pena-Diaz et al., 2012). However, since EXO1 has 5` to 3` polarity, cleavage of the leading strand could not be readily explained by EXO1 activity, since EXO1 would have to migrate several hundred nucleotides from the 3`-terminus to or even across the mismatch and would also have to compete with nucleosome loading behind the replication fork (Schöpf et al., 2012). Ghodgaonkar et al. could finally demonstrate that eukaryotic mismatch repair (MMR) is initiated by single strand breaks generated by RNase H2-mediated. Due to the high frequency of ribonucleotide incorporation by the polymerase ε, RNase H2-mediated ribonucleotide cleavage of the nascent leading strand serves as entry site for the EXO1 that facilitates MMR.

Another beneficial impact of ribonucleotide incorporation can be found during “Mating type switching” in *S. pombe*. Data shows that a two-ribonucleotide imprint might initiate the recombination process that is necessary for the switch of the mating type (Williams and Kunkel, 2014).

1.4 DNA damage response (DDR)

The maintenance of genome integrity is of particular importance in order to allow the propagation of the accurate genomic information to subsequent generations. However, the genomic DNA is constantly exposed to endogenous as well as exogenous threats that

can cause damage of the genomic information. Therefore, efficient repair pathways have been evolved to prevent the generation of mutations in the genomic information. Among the different threats, genomic ribonucleotides represent by far the most frequent DNA lesion. Studies in RNase H2-deficient yeast have shown that ribonucleotides are incorporated during basic cellular processes like replication and transcription. Investigation of the ribonucleotide incorporation rate of the three different DNA replicases demonstrated various frequencies causing the total incorporation of about 14000 ribonucleotides during a single replication cycle (Williams and Kunkel, 2014). Extrapolation to the human or mouse genome might indicate that several million ribonucleotides are possibly integrated during the process of replication only. However, under normal conditions, ribonucleotides are efficiently removed by the simultaneous activity of RNase H2 and FEN-1 (Rydberg and Game, 2002). The most threatening DNA damage is represented by DNA strand breaks, as they might induce apoptosis (Rich et al., 2000) or could lead to cancer. On the other hand, DNA double-strand breaks are naturally occurring during class-switch recombination in B cells or during meiosis. However, endogenous factors like stress-induced reactive oxygen species or exogenous UV light can also cause DNA strand breaks. To maintain genome integrity and to prevent cancer formation, the DNA damage response (DDR) pathway, an extensive signaling network that responds to DNA lesions, has been evolved to efficiently and accurately repair DNA strand breaks (Harper and Elledge, 2007). Not surprisingly, mutations in genes that encode for important players of the DDR pathways, like BRCA1 or p53, are strongly associated with cancer formation. The repair pathway that is elicited upon DNA strand breaks is hierarchically organized, with the sensor of the DNA damage on top of the hierarchy, followed by mediators and transducers of the DNA damage repair pathway and effector molecules that ultimately cause cell cycle arrest and the repair of the damage. Most importantly, signal transduction is conferred by post-transcriptional modifications, mostly phosphorylation, dephosphorylation and ubiquitination.

The Trex1-deficient mouse model displayed activation of the DNA damage response triggered by short ssDNA that was supposed to be derived from replication intermediates. As a consequence of Trex1 deficiency, these replication intermediates caused ATM-dependent checkpoint activation via Chk2 and p53 (Yang et al., 2007).

1.4.1 Double-strand break (DSB) repair

DNA double-strand breaks (DSBs) are detected by the trimeric MRN (Mre11-Rad50-Nbs1) complex in mammalian cells. The importance of this complex is reflected by the observation that mutations in the genes encoding for Mre11, Rad50 and Nbs1 cause

increased DNA damage sensitivity, genomic instability and telomere shortening (D'Amours and Jackson, 2002). Moreover, mice completely deficient for Mre11, Rad50 or Nbs1 are embryonic lethal. As sensor of DNA damage, MRN recruits the phosphatidylinositol 3-kinase-like kinase (PIKK) ATM (Ataxia telangiectasia mutated) to the DNA lesion. Another function is to generate regions of single-stranded DNA in order to amplify the signal needed for checkpoint activation. Upon recruitment, the inactive ATM dimer divides and subsequent autophosphorylation at different residues leads to the active form of ATM. Phosphorylation at serine 1981 was shown to occur early during DNA damage response, although this particular modification was not enough for activation (Bakkenist and Kastan, 2003). Subsequently, active ATM phosphorylates various downstream mediator molecules as well as the MRN complex that in turn leads to the oligomerization of the complex. An immediate target of the ATM molecule is the histone H2AX. Phosphorylation of amino acid serine 139 (γH2AX) and concomitant dephosphorylation of tyrosine 142 (constantly phosphorylated in the absence of DNA damage) leads to the recruitment of MDC1 (mediator of DNA damage checkpoint protein 1) (Lukas et al., 2011). MDC1 is subsequently phosphorylated by various kinases and its function is to prevent dephosphorylation of H2AX as well as to mediate the spreading of phosphorylated H2AX to neighboring nucleosomes by tethering ATM to the lesional DNA. Accumulation of these proteins at the DNA lesion cause the formation of DNA damage-induced foci and subsequent unwinding of the DNA double-strand allows repair proteins to gain access to the lesion. CHK2 (checkpoint kinase 2) is another important downstream target of the ATM kinase. ATM-mediated phosphorylation of CHK2 is followed by phosphorylation of the transcription factor p53. p53 in turn is a very potent transcription factor that is kept outside the nucleus by various mechanisms. MDM2, an E3 ubiquitin ligase keeps p53 expression on a low level, by labeling p53 for degradation. Furthermore, MDM2 inhibits p53 translation by ubiqutination of the positive regulator of p53, RPL26. However, phosphorylation of various downstream molecules by ATM leads to increased p53 transcription and protein stabilization that allows for the translocation of p53 into the nucleus where it activates the expression of different effector molecules. p53-dependent activation of p21 leads to cell cycle arrest in G1 or G2/M, by inhibiting cyclin-dependent kinases important for cell cycle progression, while p53-dependent activation of BAX induces apoptosis.

DNA double strand breaks are repaired by one of two possible repair pathways, homologous recombination (HR) or non-homologous end joining (NHEJ). During NHEJ, ends of the broken DNA are tethered together via the Ku protein complex that immediately binds to the DNA ends during G1. In contrast to NHEJ, HR is dependent on DNA end resection to generate a 3` single-strand overhang that can invade the DNA double-strand

of the sister chromatids in order to repair the damage. The choice between both is dependent on the cell cycle phase. HR of DNA double-strand breaks is only possible during S/G2 phase of the cell cycle, since HR requires the presence of the sister chromatids that serve as template for the repair of the double-strand break. During G1 phase of the cell cycle, DNA double-strand breaks are preferentially repaired by NHEJ. Two important mediators of the DRR mediate the pathway choice. While the p53-binding protein (53BP1) mediates NHEJ, the breast cancer-associated gene 1 (BRCA1) directs the repair to HR. 53BP1 is an immediate target of the PIKK ATM. However, MDC1-mediated phosphorylation of 53BP1 promotes its recruitment to the DNA lesion, where it participates in the generation of DNA damage foci. Binding to the DNA adjacent to the lesion inhibits DNA end resection, thus preventing the generation of a substrate for HR. At this time point BRCA1 is also bound to the damaged DNA strand, but its concentration is supposed to be too low to mediate HR. During the phase transition from G1 to S/G2, BRCA1 binds to the DNA in proximity of the damaged site and displaces 53BP1 allowing for DNA end resection by the 5`- to – 3` exonuclease (EXO1), the flap-endonuclease DNA2 together with BLM (Bloom syndrome RecQ helicase-like) and MRE11 (part of the MRN complex). While MRE11 is important in initiating DNA end resection, EXO1 and DNA2 perform long-range resection. The switch between NHEJ in G1 to HR in S/G2 is thought to be mediated by phosphorylation of CtIP. Phosphorylation of CtIP leads to the formation of the complex CtIP-MRN-BRCA1 that displaces 53BP1 from the lesional DNA. However, it turned out that NHEJ could be the preferred pathway independent from the cell cycle most likely due to increased availability of members of the NHEJ pathway.

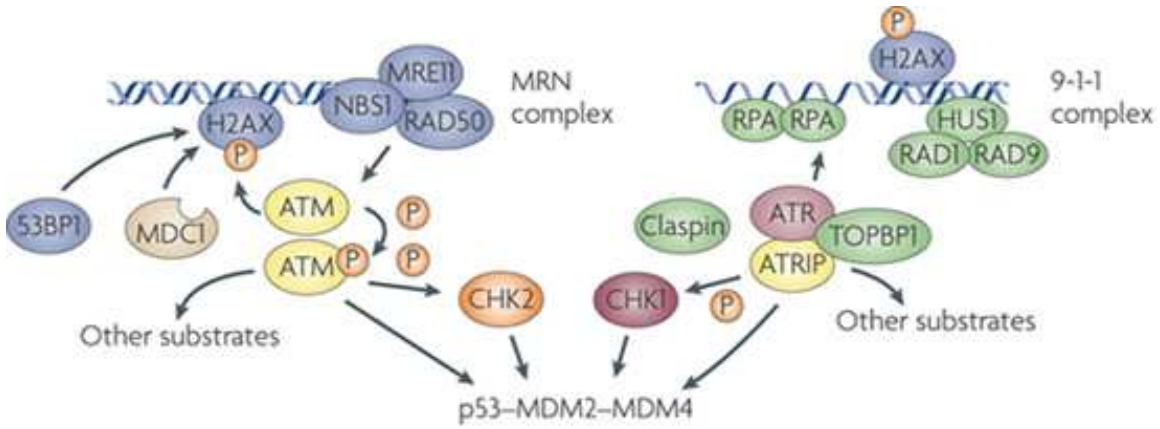

Figure1.3: Schematic overview of the DNA damage response upon DNA double-strand and single-strand breaks. While DNA double-strand breaks are sensed by the MRN (MRE11-NBS1-RAD50) complex that subsequently recruits the kinase ATM (Ataxia telangectasia mutated), RPA that anneals to single-stranded DNA recruits the kinase ATR (Ataxia telangectasia mutated and Rad3-related) upon single-strand breaks of the DNA. The activation of CHK2 by ATM and CHK1 by ATR/ATRIP leads to the activation of the tumor suppressor gene p53 that mediates a plethora of effector functions like apoptosis, cell cycle arrest or senescence. Single-strand breaks as well as double-strand breaks cause the phosphorylation of the histone 2AX (H2AX) and is thus widely used as a DNA damage marker (Adopted from Meek et al. (Meek, 2009)

1.4.2 Single-strand break (SSB) repair

In contrast to the DDR in response to double-strand breaks whose repair is mediated by ATM activity, the repair of single-strand breaks is mediated by the DNA damage sensor ATR (ataxia telangiectasia mutated and Rad3-related) another member of the phosphatidylinositol-3-kinase-like kinase (PIKK) family. ATR is activated upon the presence of single strand breaks and thus plays an important role in the pathways of single-strand break repair, but also during replication folk stalling, since replication folk stalling is an ultimate consequence of single-strand breaks. Since single-strand breaks can also be present during the generation or repair of double-strand breaks, ATR is not exclusively activated upon single-strand break repair. However, ATR activity during DNA double-strand break repair is restricted to S/G2 phase of the cell cycle, since BRCA1-mediated DNA end resection can only occur in this phase of the cycle.

In consequence of single strand breaks, the replication protein A (RPA) binds to single-stranded DNA (ssDNA) in order to prevent unwanted binding and degradation of the strand. The complex of ssDNA and RPA is detected by ATRIP (ATR-interacting protein), a protein that is regarded as an obligate subunit of ATR (Zou and Elledge, 2003). Although ATRIP directs ATR to the side of single-stranded DNA, ATR needs to be activated by the RAD9-RAD1-HUS1 (9-1-1) complex that further mediates the contact between ATR and TOPBP1 (topoisomerase-binding protein-1) (Lee et al., 2007). Single-strand break repair

is only initiated when both complexes, ATR/ATRIP and 9-1-1/TOPBP1, are recruited to the strand break. It is speculated that this mechanism represents a form of single-strand break repair regulation. However, upon activation, ATR phosphorylates several downstream molecules. Most importantly, CHK1 is phosphorylated at serine 317 and 345 that promotes CHk1 activation. Interaction between ATR and CHK1 is mediated by Claspin and constitutive presence of Claspin maintains CHK1 phosphorylation. Upon activation CHK1 dislocates from the chromatin and phosphorylates downstream substrates. Most important substrates are the Cdc25 phosphatases that mediate cell cycle progression by dephosphorylating cyclin-dependent kinases (Cdks). Thus, phosphorylation of Cdc25 leads to their inactivation and thus promoting cell-cycle arrest and allowing for the repair of the DNA damage. At the same time, CHK1 phosphorylates and activates Wee1, the kinase that phosphorylates and inactivates Cdks. Upon persistent DNA damage, ATR and CHK1 also phosphorylate p53, thus promoting sustained cell cycle arrest or apoptosis (Taylor and Stark, 2001). In order to repair single strand breaks, ATR phosphorylates several mediators of homologous recombination, like BRCA1, WRN (Werner syndrome ATP-dependent helicase) and BLM (Bloom syndrome RecQ helicase-like). The restricted expression and activation of CHK1 during S/G2 implicates repair of single-strand breaks by homologous recombination only.

1.5 Aim

Systemic lupus erythematosus (SLE) is a prototypic autoimmune disease that is characterized by an uncontrolled type I interferon response. It can be caused by mutations in various different genes, but environmental factors, like UV light, were also shown to influence at least the onset of the disease. However, the heterogeneity as well as the impact of non-genetic factors massively impedes the investigation of pathomechanisms underlying the disease. The rare autosomal recessive encepalopathy Aicardi-Goutières Syndrome (AGS) is also characterized by an uncontrolled type I interferon response and shares genetic, molecular and clinical features with SLE. Due to the overlap, AGS is currently regarded as a monogenic variant of SLE and might thus be a valuable tool to elucidate mechanisms of SLE pathology.

The aim of this doctoral thesis was to generate a mouse model for the Aicardi-Goutières Syndrome to allow for the investigation of pathomechanisms of AGS and SLE disease. To this end, we wanted to generate and analyze mice deficient for the RNase H2 enzyme that is mutated in a major portion of human AGS patients, but also in a small fraction of SLE patients. The RNase H2 enzyme is heterotrimeric nuclease that is only functional as a complex. In a first approach, we thus planed to inactivate the RNase H2 enzyme in mice by

deleting the *Rnaseh2c* gene that encodes for the smallest subunit of the enzyme. Together with the *Rnaseh2b KOF* mouse line that became commercially available from the EUCOMM consortium, the *Rnaseh2c* knockout mouse allowed for the investigation of complete RNase H2 deficiency. We hoped that these mice will recapitulate the uncontrolled type I interferon response of AGS patients in order to investigate the underlying cell-intrinsic mechanisms that cause the imbalance. Furthermore, since the *Rnaseh2b KOF* mouse line could also be used for the cell type-specific deletion of the *Rnaseh2b* gene, we also had a powerful tool available that allowed for the investigation of RNase H2 deficiency in different cell types. We were eventually interested if the deficiency of the RNase H2 enzyme in one particular cell type would be capable to trigger AGS pathology.

2 Material and Methods

2.1 Material

2.1.1 Primers

Genotyping PCR

allele	name	sequence
Rnaseh2b KOF	Rnaseh2b_40844_F	5`-CCTGAGAATGTCTGCATGGC-3`
	CAS_R1_Term	5`-TCGTGGTATCGTTATGCGCC-3`
	Rnaseh2b_40844_R	5`-GCTCATCTTGTGAGGAGGGC-3`
Rnaseh2c ko	Typing H2c wt for	5`-CACAGATCCCTTCTCACCACTTGGA-3`
	Typing H2c neo for	5`- CTGCTTGCCGAATATCATGGTGGAA-3`
	Typing H2c rev	5`-CCGAAGAACAGACCCAAGAGGAGAA-3`
Rnaseh2b floxed/deleted	5` check delta LacZ	5`-TCATCTGATGGCTCTCGGAGGAATG-3`
	3` check delta LacZ	5`-GGAGGGCACTCTAAAGAGCAAGCTA-3`
	3` check delta Exon5	5`-CTGTTGAACTGATGGCGAGCTCAGA-3`
LacZ	5` Typing LacZ h2b	5`-GGAGAATCCCGGCCCTGGGATCTGG-3`
	3` Typing LacZ h2b	5`-CTTCTGGTGCCGGAAACCAGGCAAAG-3`
p53	p53 common for	5`-ACAGCGTGGTGGTACCTTAT-3`
	p53 wild type rev	5`-TATACTCAGAGCCGGCCT-3`
	p53 mutant rev	5`-CTATCAGGACATAGCGTTGG-3`
Rag1	oIMR1746 (wt for)	5`-GAGGTTCCGCTACGACTCTG-3`
	oIMR3104 (common)	5`-CCGGACAAGTTTTTCATCGT-3`
	oIMR8162 (mutant for)	5`-TGGATGTGGAATGTGTGCGAG-3`
Ifnar1	Ifnar-upE3-for	5`-GCCCATGTATACATTTGCTCATTCCG-3`
	Ifnar-Neo-rev2	5`-CCAAGCGAAACATCGCATCGAGCGAG-3`
	Ifnar-E3-rev	5`-CGGATCAACCTCATTCCACGAAGATG-3`

Quantitative real time PCR (qRT PCR)

allele	name	sequence
Rnaseh2b	5` qRT Rnaseh2b E7/9	5`-AGGTTTCCAGGGACAAGGAAGAGGA-3`
	3` qRT Rnaseh2b E7/9	5`-GTCAATGAAGCTGGAGGTTCTGGAAG-3`
beta actin	5` qRT beta actin E3/4	5`-TGACCCAGATCATGTTTGAGACCTTCA-3`
	3` qRT beta actin E3/4	5`-GGAGTCCATCACAATGCCTGTGG-3`
Cdkn1a	5` p21	5`-GCAGATCCACAGCGATATCC-3`
	3` p21	5`-CAACTGCTCACTGTCCACGG-3`
Phlda3	5` Phlda3	5`-TTCGCCCGCATCAAAGCCGT-3`
	3` Phlda3	5`-AGGGGGCAGCGGAAGTCGAT-3`
Zmat3	5` Zmat3 qRT E4/6	5`-GAGTCACTCATTCTCGGACTCCGC-3`
	3` Zmat3 qRT E4/6	3`-GAGCGGGCATTGAAGTAAGGGC-3`
ISG15	5` ISG15	5`-GGTGTCCGTGACTAACTCCAT-3`
	3` ISG15	5`-TGGAAAGGGTAAGACCGTCCT-3`
Oligoadenylat - synthetase 1 (OAS1)	OAS-P1	5`-CCATCTGCATCAGGAGGTGGAG-3`
	OAS-P2	5`-GGAGGTACATTCCTCGATGAGGATG-3`
Rsad2	Vip-F-new	5`-CAAGCGAGGACTGCTTCTGCTC-3`
	Vip-R-new	5`-GCAGAATCTCACAAGCTTGCCC-3`
Ifi44	Ifi44-For	5`-GGCACATCTTAAAGGGCCACACTC-3`
	Ifi44-Rev	5`-CTGTCCTTCAGCAGTGGGTCATG-3`

Generation of Rnaseh2c targeting vector

allele	name	sequence
homology region 1	5` HR up (*XbaI*)	5`-GGACT*TCTAGA*TGGTACTTTGCAAGCAGCCCCTGGAGGAGA-3`
	5` HR down (*BamHI*)	5`-CGTACC*GGATCC*GTGATGAGGATTGGACTCAGGGCCTTGGAC-3`
homology region 2	3` HR up (*HindIII*)	5`TATGGTGTCCTAGGCTTTAGCTAGTCGCAGTCATT*AAGCTT*CTTTGGTCCACGTGTTCAGAGCGGACCTGG-3`
	3` HR down (*XhoI*)	5`CCTAATGAATTGGCCTGTAGCTGGTAGTCTATCCAT*CTCGAG*ACTCCGCCTCCTGTGCTCTATTGCTTTAGG-3`
DT gene cassette	DT-XhoI-For-New (*XhoI*)	5`-GCTAG*CTCGAG*CCGTCGACGGTATCGATAAGCTTGATATCGAATT-3`
	DT-XhoI-Rev-New (*XhoI*)	5`-GCTAG*CTCGAG*CCCACCCCCCAGAATAATAGAATGACACCTACT-3`

Sequencing primers

allele	name	sequence
homology region 1	HR1seq1 for	5`-CTGCAAGGCGATTAAGTTGGGTAA-3`
	HR1seq1 rev	5`-GCACATGTCCTACCAGCTCACACTG-3`
	HR1seq2 for	5`-CATGTGCAGTGAGCTGGTGGGACAT-3`
	HR1seq2 rev	5`-CTACCGGTGGATGTGGAATGTGTGC-3`
homology region 2	HR2seq1 for	5`-GAATAAAGACCGACCAAGCGACGTC-3`
	HR2seq1 rev	5`-CCTCCTATCCTACCGAAGTTACTGG-3`
	HR2seq2 for	5`-GGAACAGACAGACCAAACCACAACC-3`
	HR2seq2 rev	5`-CACACAGGAAACAGCTATGACCATG-3`

Test for homologous recombination of the targeting vector

allele	name	sequence
Screening PCR	HR2seq1 for	5`-GAATAAAGACCGACCAAGCGACGTC-3`
	HR2-est.	5`-GTGCTTGGATCATCACGAGGCCAGTAG-3`
upstream probe	*T7*-H2c probe1 up for	5`*TAATACGACTCACTATAGGGAGA*CTGAAACGAGATGGAGTGACCATGAGGAC-3`
	SP6-H2c probe1 up rev	5`*ATTTAGGTGACACTATAGAAGCG*GTCCTAATAGGGACAGGAAATTGCTCTG-3`
downstream probe	*T7*-H2c probe1 down for	5`*TAATACGACTCACTATAGGGAGA*CAGTGTCATCAGTTTAGCTGCGATCC-3`
	SP6-H2c probe1 down rev	5`*ATTTAGGTGACACTATAGAAGCG*GTAAGGCTAGTCTCTGAGAACCGACG-3`

2.1.2 Kits

Kit	product number	Vendor
DIG RNA Labeling Kit (SP6/T7)	11175025910	Roche Diagnostics GmbH, Mannheim
DIG Wash and Blocking buffer set	11585762001	Roche Diagnostics GmbH, Mannheim
FastStart Universal SYBR Green Master (Rox)	4913914001	Roche Diagnostics GmbH, Mannheim
MEGAclear™ Transcription Clean-Up Kit	AM1908	Life Technologies GmbH, Darmstadt
Peroxidase Substrate Kit DAB	SK-4100	Vector Laboratories, Inc., Burlingame, California
RevertAid™ H Minus cDNA Synthesis Kit	K1631	Life Technologies GmbH, Darmstadt
RNeasy Fibrous Tissue Mini Kit	74704	Qiagen GmbH, Hilden
RNeasy Mini Kit	74104	Qiagen GmbH, Hilden
Trichrome Stain (Masson) Kit	HT15-1KT	Sigma-Aldrich Chemie GmbH, München

2.1.3 Buffers and solutions

buffer	reagents
1x PBS	137 mM NaCl, 2.7 mM KCl, 10 mM Na2HPO4, 1.8 mM KH2PO4 (pH 7.4)
1x TBS	50 mM Tris HCl (pH 7.5), 150 mM NaCl
50x TAE	2 M Tris, 50 mM EDTA (pH 8), 5.7% acetic acid
TE buffer	10 mM Tris HCl, 1 mM EDTA (pH 7.6)
1x lysis buffer	0.1 M Tris-HCl, 0.2 M NaCl, 0,2% SDS, 5 mM EDTA (pH 8)
ES cell lysis buffer	10 mM NaCl, 10 mM Tris-HCl (pH 7.5), 10 mM EDTA, 0.5% sacrosyl, 0.4 – 1 mg /ml proteinase K
Red blood cell lysis buffer	155 mM NH4Cl, 10 mM KHCO3, 0.1 mM EDTA
Denature buffer	1.5 M NaCl, 0.5 M NaOH
Neutralization buffer	1.5 M Tris, 1.5 M NaCl (adjusted with HCl to pH 7.6)
20x SSC	3 M NaCl, 0.3 M tri-sodium citrate (adjusted with HCl to pH 7)
Wash buffer 1	2 x SSC, 0.1% SDS
Wash buffer 2	0.2 x SSC, 0.1% SDS
Blocking buffer (Ki67)	1% BSA, 0.1% cold fish skin gelantin, 0.5% Triton X-100, 0.05% sodium azide, 0.01 M PBS (pH 7.2)
Steamer buffer	2 mM tri-sodium citrate, 0.05% Tween 20 (pH 6)
solution D	4 M guanidinium thiocyanate, 25 mM sodium citrate (pH 7), 0.5% Sarkosyl, 0.1 M β-mercaptoethanol
FACS buffer	2% fetal calf serum in 1 x PBS
Protein extraction buffer	50 mM Tris (pH 8), 280 mM NaCl, 0.5% NP40, 0.2 mM EDTA, 0.2 mM EGTA, 10% (v/v) glycerol, 0.1 mM sodium vandate, 1 mM DTT*, 1 mM PMSF* (*freshly added)
Cytoplamic buffer	20 mM HEPES, 10 mM KCl, 1 mM EDTA, 0.1 mM sodium vandate, 1 mM DTT*, 1 mM PMSF* (*freshly added)
Anesthetization solution	10 mg/ml xylazine, 1 mg/ml ketamine in 0.7% physiologic salt solution

2.1.4 Antibodies

cell type	epitope	fluorochrome	clone	isotype	dilution
hematopoietic cells	CD45	FITC	30-F11	rat IgG2b, κ	1:400
		eFluor450	30-F11	ratIgG2b, κ	1:400
		V500	30-F11	ratIgG2b, κ	1:200
	CD45.1	FITC	A20	mouse IgG2a, κ	1:400
		PECy7	A20	mouse IgG2a, κ	1:100
	CD45.2	PE	104	mouse IgG2a, κ	1:100
neutrophilic granulocytes	CD11b	FITC	M1/70	rat IgG2b, κ	1:1600
		Biotin	M1/70	rat IgG2b, κ	1:800
	Ly6C/G (Gr1)	PerCP Cy5.5	RB6-8C5	rat IgG2b, κ	1:1200
		Biotin	RB6-8C5	rat IgG2b, κ	1:800
antigen-presenting cells (APCs)	MHC II I-A/I-E	eFluor 450	M5/114.15.2	rat IgG2b, κ	1:200
	MHC II I-AB	FITC	AF6-120.1	mouse IgG2a, κ	1:500
B cells	CD19	PECy7	eBio1D3	rat IgG2a, κ	1:200
		eFluor450	eBio1D3	rat IgG2a, κ	1:400
		Biotin	eBio1D3	rat IgG2a, κ	1:800
	CD45R (B220)	APC	RA3-6B2	rat IgG2a, κ	1:200
		FITC	RA3-6B2	rat IgG2a, κ	1:200
		Biotin	RA3-6B2	rat IgG2a, κ	1:400
α/β-T cells	CD3e	APC	145-2C11	IgG	1:100
		Biotin	145-2C11	IgG	1:400
	CD4	PE	GK1.5	rat IgG2b, κ	1:500
		Biotin	GK1.5	rat IgG2b, κ	1:400
	CD8a	APC-eFluor 780	53-6.7	rat IgG2a, κ	1:200
		Biotin	53-6.7	rat IgG2a, κ	1:800
NK cells	NK1.1	Biotin	PK136	rat IgG2a, κ	1:800
erythrocytes	Ter119	Biotin	TER-119	rat IgG2b, κ	1:800
hematopoietic stem cells	CD150	PECy7	TC15-12F12.2	rat IgG2a, α	1:200
	CD48	APC	HM48-1	IgG	1:100
		FITC	HM48-1	IgG	1:100
	CD117 (c-kit)	APC-eFluor 780	2B8	rat IgG2b, κ	1:1600
	Ly6A/E (Sca1)	PerCP Cy5.5	D7	rat IgG2a, κ	1:400
		V500	D7	rat IgG2a, κ	1:200
hematopoietic stem cells, skin stem cells	CD34	eFluor 660	RAM34	rat IgG2a, κ	1:25
keratinocytes	CD49f	PE	eBioGoH3	rat IgG2a, κ	1:400
	CD104	Biotin	346-11A	rat IgG2a, κ	1:100
Langerhans cells	CD205 (DEC205)	PerCP-eFluor 710	205yekta	rat IgG2a, κ	1:200
	CD207 (Langerin)	PE	eBioL31	IgG2a	1:100
	CD103	APC	2E7	IgG	1:200
γ/δ-T cells	γ/δ TCR	FITC	eBioGL3 (GL-3, GL3)	IgG	1:100
blocking antibody	CD16/32	unconjugated	93	rat IgG2a, λ	1:200

2.2 Animal experiments

2.2.1 Mouse husbandry

All mice were housed at the Experimental Centre of the University of Technology Dresden (Medical Faculty Carl Gustav Carus) in individually ventilated cages (IVCs) and under specific-pathogen-free conditions (SPF). Pathogen-free conditions were regularly tested according to the Federation for Laboratory Animal Science (FELASA). At most five adult mice of the same gender were kept in a single Ehret type 2L cage (Ehret, ≈ 500cm^2). Mice were housed at an ambient temperature of 22℃ and a relative humidity of 50-60% during a day-night cycle of 12 hours each. Mice had constant access to food and water (acidified, pH 4.5) (*ad libitum*). To obtain newborn litter, mice older than 8 weeks were crossed. One male mouse was bred to one or two female mice. The newborn litter was weaned three weeks after birth. The newborns were ear-tagged and a tail tip was cut with a heated scissor to allow for genotyping. Mouse housing was organized using the Phyton-based Relational Animal Tracking (PyRAT) software (Scionics Computer Innovation GmbH Germany, Dresden). All experimental procedures were according to the German animal welfare law approved by the Landesdirektion Dresden.

2.2.2 Genotyping

For genotyping of the newborn litter, isolated DNA was amplified according to standard PCR techniques (see below). An appropriate set of primers was used to amplify the particular gene locus (Table 2.1.1). PCR products were subsequently separated by gel electrophoresis in 1% agarose gels (Biozym LE Agarose, Biozym Scientific GmbH, Hessisch Oldendorf) in 1 x TAE buffer and visualized using the Molecular Imager® ChemiDoc™ XRS Imaging System (Bio-Rad Laboratories GmbH, München). Mouse genotypes were immediately registered in the PyRAT software.

2.2.3 Mouse skin thickness

Mice were anesthetized and the back was shaved using an electric shaver. To determine the skin thickness, the neck skin was grabbed using blunt forceps and the emerging skin fold was measured in triplicate using a caliper (Mitutoyo Deutschland GmbH, Neuss). In case of spontaneous ulcerations, the measuring point was placed more caudal. Ear thickness was determined at the un-tagged ear and also measured in triplicate.

2.3 Standard molecular techniques

2.3.1 Isolation protocols

2.3.1.1 Isolation of genomic DNA from mouse tail tips

Tail tips were lysed in a 1.5 ml collection tube containing 500 µl lysis buffer and 5 µl Proteinase K (20 mg / ml). Lysis was performed for at least 2 hours at 56°C and constant shaking at 1000 rpm. Lysed tails were centrifuged for 10 minutes at 13000 rpm and the supernatant was transferred into a new 1.5 ml collection tube containing 500 µl isopropanol. DNA was precipitated by inverting the tube at least ten times and pelleted by centrifugation for 10 minutes at 13000 rpm. The supernatant was removed and the pellet was washed in 350 µl 70% ethanol. The pellet was dried to allow the evaporation of the ethanol and finally resuspended in 100 µl TE buffer. Resuspension was facilitated by incubation at 56°C for 2 hours and constant shaking at 800 rpm. In case DNA was isolated from larger tissues or organs, the reaction mixture was scaled accordingly.

2.3.1.2 RNA isolation from newborn mouse epidermis

To obtain RNA for gene expression analysis, newborn mice were prepared as described (2.4.2.2). To avoid unwanted RNA degradation, the Dispase (neutral protease, grade II, Roche Diagnostics GmbH, Mannheim) digest was reduced to 2 hours at 4°C. The epidermis was manually separated from the dermis by softly shifting the epidermis against the dermis using blunt forceps. RNA from the epidermis was subsequently isolated following the RNeasy Mini Kit protocol. Tissue was disrupted in 600 µl RLT buffer containing β-mercaptoethanol using the gentleMACS Dissociator (Miltenyi Biotec GmbH Germany, Bergisch Gladbach) and program RNA_01. RNA was finally eluted in 50 µl elution buffer.

2.3.1.3 RNA isolation from murine fetal liver cells

Fetal liver cells from E14.5 mouse embryos were isolated and immediately (≤ 30min) homogenized in 1 ml solution D using the gentleMACS dissociator (Miltenyi Biotec GmbH Germany, Bergisch Gladbach) and program RNA_01. Subsequent RNA isolation was performed by acid guanidinium thiocyanate-phenol-chloroform extraction according to Chomczinsky et al. (Chomczynski and Sacchi, 2006). To avoid contamination with phenol, the aqueous phase was pipetted generously. RNA was finally resuspended in 100 µl nuclease-free water.

2.3.1.4 RNA isolation from adult mouse skin

Skin biopsies were collected using an 8 mm biopsy puncher (Stiefel, SmithKline Beecham Ltd. UK). The adipose tissue was carefully removed using scalpels and the skin was immediately placed in RNAlater RNA Stabilization Reagent (Qiagen, Hilden). The skin was homogenized in 600 µl RLT buffer containing β-mercaptoethanol using the gentleMACS Dissociator (Miltenyi Biotec GmbH Germany, Bergisch Gladbach) and program RNA_01. RNA was isolated according to the RNeasy Fibrous Tissue Kit protocol and finally eluted in 50 µl elution buffer. The optional on-column DNase I digest was omitted.

2.3.2 Nucleic acid species

2.3.2.1 Polymerase chain reaction (PCR)

Gene loci of interest were amplified by polymerase chain reaction (PCR). Primers for amplification were chosen using the non-commercial Primer-BLAST software (The National Center for Biotechnology Information, Bethesda, Maryland) according to the preferences of the primer length of 25 bp, a GC content of 40-60% and an annealing temperature of 58°C. Standard PCR was performed in a total volume of 50 µl, containing 1 µl genomic DNA, 0.2 mM dNTPs, 1 x Taq polymerase buffer, 0.2 mM 5`-primer, 0.2 mM 3`-primer, 1.5 µl Taq DNA polymerase and water. An expected PCR product of 500 bp was amplified with an initial denaturation step at 95°C for 5 min, followed by 35 cycles of denaturation at 95°C for 3 0 s, annealing at 58°C for 30 s and elongation at 72°C for 30 s (PCR-Cycler T3000 Therm ocycler, Biometra Biomedizinische Analytik GmbH, Göttingen). The annealing and elongation time of longer products were adjusted accordingly. Elongation time of 1 kb was set to 1 minute. PCR products were separated by gel electrophoresis in 1% agarose in 1x TAE buffer and visualized using the Molecular Imager® ChemiDoc™ XRS Imaging System (Bio-Rad Laboratories GmbH, München)

2.3.2.2 Isolation of PCR products from agarose gels

PCR products were isolated according to the manual of the GENECLEAN Turbo Kit (MP Biomedicals Europe). For that purpose PCR products were cut from the agarose gel using the Molecular Imager® ChemiDoc™ XRS Imaging System (Bio-Rad Laboratories GmbH, München) and transferred into 1.5 ml collection tubes and the weight of the gel piece was determined. The extracted DNA was usually eluted in 30 µl elution buffer.

2.3.2.3 Quantification of nucleic acid concentrations

Nucleic acid concentrations (DNA and RNA) were either measured using NanoDrop 2000 (Thermo Fisher Scientific Germany, Frankfurt a. M.) or the Qubit® 2.0 Fluorometer (Life Technologies Germany, Darmstadt) according to the recommendations of the vendor. In case nucleic acid concentrations were measured using the Qubit® 2.0 Fluorometer, 2 µl nucleic acid were put into the reaction.

2.3.2.4 Sequencing of PCR products

The gene locus to be sequenced was amplified using standard PCR techniques, PCR products were subsequently separated by gel electrophoresis in 1% agarose gels in 1 x TAE buffer and extracted from the gel as described (2.3.2.2). Finally, the DNA concentration of PCR products was determined using NanoDrop Technology. For the sequencing of a product of 400 bp, 72 ng PCR product were either mixed with the forward or the reverse primer in a total volume of 12 µl and send to Seqlab – Sequence Laboratories Göttingen GmbH. Sequencing results were displayed using Chromas Lite software (Technelysium Pty Ltd. Australia, Brisbane). Amount of PCR product was adjusted to the length of the PCR product.

2.3.2.5 cDNA synthesis

100 ng – 1 µg total RNA were reverse transcribed into cDNA using poly $(dT)_{18}$ oligonucleotides following the manufacturer`s instructions (RevertAid™ H Minus cDNA Synthesis Kit, Thermo Fisher Scientific Germany, Frankfurt a. M.). In brief, RNA and poly $(dT)_{18}$ primers were mixed in a total volume of 12 µl and denatured at 65℃ for 5 min followed by an incubation for 5 min on ice. Additional reagents were added to a final concentration of 1 x reaction buffer, 20 units RiboLock™ RNase Inhibitor, 1 mM dNTP mix, 200 units RevertAid™ H Minus M-MuLV Reverse Transcriptase (RT) and water in a final volume of 20 µl. Reverse transcription was performed at 42℃ for 60 min. Reverse transcription was also performed without RNA (non-template control) and without reverse transcriptase (RT-). These samples were used to check for contamination and served as negative controls in subsequent quantitative real-time PCR. To avoid reverse transcription of DNA, intron-spanning primers were used.

2.3.2.6 Quantitative real time PCR (qRT PCR)

Quantitative real time PCR mix was prepared according to the FastStart Universal SYBR Green Master (Rox) protocol (Roche Diagnostics GmbH, Mannheim). 1 µl cDNA was added to a final reaction volume of 25 µl, containing 1 x SYBR Green, 6 µM

forward and reverse primer (Table 2.1.1), respectively. Target genes were amplified by polymerase chain reaction, initiated by denaturation for 15 min at 95℃ and followed by 40 cycles of denaturation for 15 s at 95℃, annealing for 30 s at 58℃ and elongation for 30 s at 72℃. Incorporation of SYBR green was analyzed using the Mx3005P QPCR system (Agilent Technologies Sales & Services GmbH & Co.KG, Waldbronn) and the MxPro QPCR software (Agilent Technologies Sales & Services GmbH & Co.KG, Waldbronn). Non-template and RT- cDNA was used as control for DNA contamination. Fold change of transcript levels was calculated by pair-wise comparison of knockout versus wild type samples that were normalized to the reference gene beta actin.

2.3.2.7 Microarray analysis

Gene expression analysis was performed in collaboration with Julia Jarrells and Britta Schilling from the Max Planck Institute for Cell Biology and Genetics in Dresden.
RNA quality was first determined using the 2100 Bioanalyzer Instruments (Agilent Technologies Sales & Services GmbH & Co.KG, Waldbronn). Samples with uneven or bad quality were rejected from the experiment. RNA was then reverse transcribed, amplified and biotin labeled using the Message Amp II-Biotin Enhanced Kit (Ambion, Life Technologies Germany, Darmstadt). Hybridization, staining and scanning of the GeneChip Mouse Genome 430 2.0 microarrays were performed according to the Affymetrix GeneChip Expression Analysis Technical Manual (P/N 702232 Rev. 3) (Affymetrix UK Ltd.)

2.4 Cell cultivation

2.4.1 Cell culture media

2.4.1.1 Fibroblast medium

Fibroblast medium: Gibco® Dulbecco`s modified Eagle medium (DMEM) (Life Technologies Germany, Darmstadt) supplemented with 10% fetal bovine serum (Biochrom, Merck KGaA Germany, Darmstadt), 100 u/ml penicillin, 10 µg/ml streptomycin (Biochrom, Merck KGaA Germany, Darmstadt), 1 x non-essential amino acids (Biochrom, Merck KGaA Germany, Darmstadt) and 100 µM β-mecaptoethanol (Sigma-Aldrich Chemie GmbH, München)

2.4.1.2 Keratinocyte medium

DMEM (2/3) + HAM`s F12 (1/3) (FZ9995, Biochrom, Merck KGaA Germany, Darmstadt) supplemented with 10% calcium free FCS Gold (PAA, GE Healthcare

Europe, Freiburg), 100 u/ml penicillin, 10 µg/ml streptomycin (Biochrom, Merck KGaA Germany, Darmstadt), 1 mM L-glutamine, 0.025 g sodium L-ascorbate (A4034, Sigma-Aldrich Chemie GmbH, München), 10 ng/ml epidermal growth factor (EGF)(E9644, Sigma-Aldrich Chemie GmbH, München), 5 µg/ml insulin (11882, Sigma Aldrich), 0.5 µg/ml hydrocortisone (H4001, Sigma-Aldrich Chemie GmbH, München), 10^{-10} M cholera toxin (C-8052, Sigma-Aldrich Chemie GmbH, München) and 1.8×10^{-4} M adenine (A3159; Sigma-Aldrich Chemie GmbH, München)

2.4.1.3 B cell medium

B cell medium: Gibco® RPMI 1640 (Life Technologies Germany, Darmstadt) supplemented with 10% fetal bovine serum (Biochrom, Merck KGaA Germany, Darmstadt), 100 u/ml penicillin, 10 µg/ml streptomycin (Biochrom, Merck KGaA Germany, Darmstadt), 2 mM L-alanyl-L-glutamine and 10 µM β-mecaptoethanol (Sigma-Aldrich Chemie GmbH, München)

2.4.2 Cell preparation

2.4.2.1 Preparation of mouse embryonic fibroblasts

Timed breedings were set and embryos were collected by caesarian section 14.5 or 18.5 days after detection of a vaginal plug. Embryos were decapitated and inner organs as well as all red tissue were removed. The embryos were minced with scissors, digested in 1 ml 1 x trypsin (0.25%, Life Technologies Germany, Darmstadt) for 10 minutes at 37℃ and disaggregated by aspiration through a 1000 µl pipette tip. Embryonic cells were seeded in 10 ml complete DMEM medium on a 10 cm culture dish. The embryo`s tail was used for genotyping.

2.4.2.2 Preparation of keratinocytes from newborns` skin

Newborns were collected one or two days after birth, killed by decapitation and kept on ice. For disinfection, newborns were incubated for one minute each in Betaisodona® (1:1 in 1 x PBS, Mundipharma GmbH Germany, Limburg), 70% ethanol, 1 x PBS and 1 x antibiotic-antimycotic (Life Technologies Germany, Darmstadt). All extremities were removed leaving short stubs and the tail was used to isolate genomic DNA for genotyping. Using a scissor, a sagittal cut was made along the dorsum and the skin was peeled off using blunt forceps. After digestion in 5 mg / ml Dispase (neutral protease, grade II, Roche Diagnostics GmbH, Mannheim) for about 15 hours at 4℃, the dermis was separated from the epidermis using blunt forceps and softly shifting the

dermis against the epidermis. The epidermis was then placed onto a droplet of 500 µl trypsin (TrypLE Express without phenol red, Life Technologies Germany, Darmstadt), with the basal membrane facing the trypsin. After digestion for additional 30 minutes at room temperature, keratinocytes were isolated from the epidermis by repeated flushing with complete keratinocyte medium. The cell suspension was collected, strained using a 100 µm nylon filter and centrifuged for eight minutes at 500 g. The supernatant was discarded and the cell pellet was resuspended in 2 ml complete keratinocyte medium. 1 x 10^6 keratinocytes were seeded on a 6 cm petri dish pre-coated with 30 µg/ml Collagen G (Biochrom, Merck KGaA Germany, Darmstadt).

2.4.3 *In vitro* cell assays

2.4.3.1 ^{3}H-thymidine proliferation assay

2.5 x 10^3, 5 x 10^3 and 10 x 10^3 mouse embryonic fibroblasts were seeded in triplicates into flat-bottom 96-well plates and cultivated in complete DMEM medium. After 48 hours of incubation, 3.7 x 10^4 becquerel (Bq) ^{3}H-thymidine (HARTMANN ANALYTIC GmbH Germany; Braunschweig) were added to each well and cells were cultivated for additional 48 hours. Finally, mouse embryonic fibroblasts were washed, detached from the 96-well plate and transferred onto “Printed Filtermat A” (Perkin Elmer Germany, Rodgau), lysed in water, washed to remove excess label and covered with MeltiLex™ A Melt-on Scintillator Sheets (Perkin Elmer Germany, Rodgau). Incorporation of ^{3}H-thymidinde was measured for one minute per well using the 1450 MicroBeta TriLux scintillation counter (Perkin Elmer Germany, Rodgau).

2.4.3.2 Cell cycle analysis

5 x 10^5 mouse embryonic fibroblasts were seeded into a 6-well plate and cultivated until confluency in complete DMEM medium. After 72 hours, supernatant was transferred to a new collection tube, cells were washed in 1 x PBS, incubated in 1 x trypsin (0.25%, Life Technologies Germany, Darmstadt) and then added to the collected supernatant. The cell suspension was then centrifuged at 1200 rpm for 5 min, the supernatant was discarded and the cell pellet was washed in 1 x PBS. Finally, cells were resuspended in 500 µl 1 x PBS and fixed by adding 4.5 ml 70% ethanol for at least 24 hours at -20°C. For DNA content analysis c ells were washed in 1 x PBS and resuspended in 0.5 mg/ml RNAse A (Sigma-Aldrich Chemie GmbH, München) and 2.5 µg/ml propidium iodide (Sigma-Aldrich Chemie GmbH, München) and incubated for 10-30 minutes at room temperature in the dark. Cells were analyzed using MACSQuant flow cytometer (Miltenyi Biotec GmbH Germany, Bergisch Gladbach).

2.4.3.3 *In vitro* LPS stimulation of splenic B cells

Total spleen cells were isolated as described and seeded at a density of 3 x 10^5 cells in complete B cell medium containing 25 µg/ml LPS from Salmonella Minnesota Re 595 (Sigma-Aldrich Chemie GmbH, München). For DNA content analysis, cells were harvested after three days and fixed as described for mouse embryonic fibroblasts. For the ^{3}H thymidine incorporation assay, cells were seeded into 96 well plates and stimulated for 48 hours before ^{3}H thymidine was added and cells were further cultivated for additional 24 hours. Cells were transferred onto “Printed Filtermat A” (Perkin Elmer Germany, Rodgau), lysed in water, washed to remove excess label and covered with MeltiLex™ A Melt-on Scintillator Sheets (Perkin Elmer Germany, Rodgau). Incorporation of ^{3}H-thymidinde (HARTMANN ANALYTIC GmbH Germany; Braunschweig) was measured for one minute per well using the 1450 MicroBeta TriLux scintillation counter (Perkin Elmer Germany, Rodgau).

2.5 Preparations of cell suspensions

2.5.1 Peripheral blood cells

Peripheral blood was collected from the retro-orbital bulbus and immediately mixed with an equivalent volume of heparin (1:10 in 1 x PBS, Merck KGaA Germany, Darmstadt). Red blood cells were lysed three times by incubating complete blood in red blood cell lysis buffer for 1 minute at RT. Reaction was stopped by adding an equivalent volume of PBS. Finally, blood leukocytes were resuspended in FACS buffer.

2.5.2 Fetal liver / fetal thymus cells

Fetal liver was isolated from E14.5 or E18.5 embryos and fetal thymus was isolated from E18.5 embryos, respectively. Organs were transferred to a 6 well plate containing 2 ml FACS buffer per well. Fetal liver and fetal thymus was disaggregated by aspiration through an 18G x 1½ needle (Beckton Dickinson Germany, Heidelberg) for ten times before cells were further homogenized by aspiration through a 20G x 1½ needle (Beckton Dickinson Germany, Heidelberg) for additional ten times. Red blood cell lysis was not performed on fetal liver and thymus cells. The cell suspension was finally filtered through a 100µm mesh to remove tissue debris.

2.5.3 Spleen cells

The spleen was immediately withdrawn from the mouse peritoneum and transferred into ice-cold 1 x PBS. Surrounding white tissue was carefully removed before the spleen was minced into small pieces and transferred onto a 100 µm nylon filter. The plunger of a 5 ml syringe was used to press the cells softly through the filter. The filter was subsequently washed with FACS buffer to obtain maximal spleen cell numbers. Cells were centrifuged for 5 min at 1200 prm and RT, the supernatant was removed and red blood cells were lysed in red blood cell lysis buffer. Lysis was stopped by adding 1 x PBS, cells were again centrifuged for 5 minutes at 1200 rpm and RT and the supernatant was removed. Cells were resuspended in 5 ml FACS buffer and finally filtered via a 100 µm nylon mesh.

2.5.4 Bone marrow cells

Femur and tibia were isolated and muscle tissue was carefully removed. Bones were subsequently crushed in a volume of 5 ml FACS buffer using mortar and pistil. Bone marrow cells were disaggregated by aspiration through a 23G x 1½ needle (Beckton Dickinson Germany, Heidelberg) and subsequently filtered through a 40 µm nylon mesh. Cell suspension was centrifuged for 5 minutes at 1200 rpm and RT, the supernatant was discarded and red blood cells were lysed by incubation in red blood cell lysis buffer for 1 minute at RT. Reaction was stopped by adding an equivalent volume of 1 x PBS, pelleted, resuspended in 2 – 3 ml FACS buffer and filtered through a 40 µm nylon filter.

2.5.5 Adult epidermal cells

Epidermis cells from adult skin were isolated according to Jensen et al (Jensen et al., 2010). Mice were first narcotized using anesthetization solution (100 µl per mg bodyweight), thoroughly shaved and killed by cervical dislocation. The dorsal skin was completely excised and the adipose tissue was carefully scraped using scalpels. The skin was placed on a layer of 1 x trypsin (0.25%, Life Technologies Germany, Darmstadt) with the dermis facing the liquid. After incubation for about 2 hours, the epidermis was separated from the dermis by slowly shifting the epidermis against the dermis using blunt forceps. The epidermis was subsequently minced with scalpels into small pieces and digested in 5 - 10 ml 1 x trypsin (0.25%, Life Technologies Germany, Darmstadt) for another hour. Reaction was stopped by adding an equal volume of complete keratinocyte medium (calcium-free) and cells were strained through a 40 µm nylon mesh. Cells were then centrifuged for 8 min at 500 g and RT and the pellet was finally resuspended in 2 ml FACS buffer.

2.6 Southern Blot analysis

2.6.1 DIG-labeled RNA probes for Southern Blot analysis

The DNA sequence of the upstream and downstream probe was first amplified on BAC DNA (BAC RP23-156A18) (Osoegawa et al. 2000) using the appropriate set of primers (see table 2.1.1) and standard PCR techniques. PCR products were size-separated by gel electrophoresis and the correct PCR product was subsequently extracted from the agarose using the GENECLEAN Turbo Kit (MP Biomedicals Europe) following the recommendations of the vendor. Amplification of genomic DNA was performed using primers containing promoter sequences of RNA polymerase T7 and SP6 allowing for subsequent synthesis of DIG-labeled RNA probes. 1 µg DNA, 1x NTP labeling mixture, 1x Transcription buffer, Protector RNase inhibitor, RNA polymerase SP6 and RNA polymerase T7, respectively, and water were added to a final volume of 20 µl. The reaction was incubated for 2 hours at 37°C. Template DNA was removed by digestion with DNase I for additional 15 minutes at 37°C before the reaction was stopped by adding EDTA (pH 8) to a final concentration of 0.1 M. DIG-labeled RNA probes were finally purified using the MEGAclear™ Transcription Clean-Up Kit (Life Technologies Germany, Darmstadt) and following the instructions of the protocol. The RNA probe was eluted in 50 µl elution solution.

2.6.2 Isolation of genomic DNA from mouse ES cells (96 well plate)

Confluent ES cells were washed once with 100 µl PBS and subsequently lysed in ES cell lysis buffer at 56°C in a humidified chamber over night. After lysis, ES cells were cooled to RT for 1 h. Thereafter, additional 100 µl 100% ethanol were added to the ES cell lysate and DNA was allowed to precipitate for 1 – 2 hours before the supernatant was carefully discarded while the DNA remained attached to the bottom of the 96 well plate. DNA was subsequently washed three times in 70% ethanol. Finally DNA was dried for 10 – 15 minutes to allow ethanol evaporation and dissolved in 20 µl distilled water. In case DNA yield was too low, ES cells were expanded to 10 cm petri dishes to obtain maximal DNA yield. The isolation protocol was adjusted accordingly.

2.6.3 Restriction enzyme digestion of genomic DNA

For Southern Blot analysis of the DNA from gene-targeted mouse ES cells, different amounts of genomic ES cell DNA were digested with the restriction enzyme ApaLI (Thermo Fisher Scientific Germany, Braunschweig). The reaction mix of 60 µl contained different amounts of DNA, 1x buffer Tango (NEB), 1mM spermidine, 1mM DTT, 50 µg / ml RNAse A (Sigma-Aldrich Chemie GmbH, München) and 50 units ApaLI. The DNA was digested at 37°C overnight and the next morning additional 10 units ApaLI (in a total volume of 10 µl containing 1x buffer Tango) were added to the reaction and further incubated for two more hours.

2.6.4 Southern Blot

ApaLI-digested DNA was size-separated by gel electrophoresis in a 0.8% TAE agarose gel with 3 V/cm for about six hours. A 1 kb DNA marker (Thermo Fisher Scientific Germany, Frankfurt a. M.) and Digoxigenin-labeled DNA Molecular Weight marker III and VII (Roche Diagnostics GmbH, Mannheim) served as a size standard. After electrophoresis, the excess of the agarose gel was cut using the Molecular Imager® ChemiDoc™ XRS Imaging System (Bio-Rad Laboratories GmbH, München). DNA was then denatured twice for 15 minutes in denature solution followed by neutralization for 15 minutes in neutralization buffer. To allow DNA transfer onto a nylon membrane via capillary blotting, the agarose gel was placed upside down onto three layers of moistened chromatography paper (3MM, GE Healthcare Europe, Freiburg) which were placed on a platform and whose ends submerged into a reservoir of 20 x SSC. The nylon membrane (positively charged, Roche Diagnostics GmbH, Mannheim), pre-moistened in 2 x SSC to allow efficient transfer, was placed on the agarose gel. Three

moistened sheets of Chromatography paper and a pile of Apura paper was placed on top. To increase capillary forces, a weight was placed on the Apura paper. The DNA was blotted onto the nylon membrane overnight and thereafter cross-linked by incubation at 120°C for 30 minutes. For Southern Blot analysis, the membrane was pre-hybridized in DIG Easy Hyb Granules (Roche Diagnostics GmbH, Mannheim) for at least one hour at 50°C, before the DIG-labeled probe was added and the membrane was further incubated overnight at 50°C. Unbound probe was removed by adding wash buffer 1 (2 x 5 minutes at RT) before the membrane was extensively washed with wash buffer 2 (2 x 15 minutes at 63°C). For secondary antibody incubation, the membrane was first equilibrated for 5 minutes in DIG washing buffer (Wash and block buffer set, Roche Diagnostics GmbH, Mannheim), blocked for at least one hour and incubated in anti-Digoxigenin antibody labeled to alkaline phosphatase (AP) that was diluted in DIG blocking buffer. The membrane was incubated for additional two hours, before it was washed two times with DIG washing buffer for 15 minutes at RT. For the detection DIG-labeled DNA, the membrane was equilibrated with DIG detection buffer for 5 minutes at RT before CDP-Star (Roche Diagnostics GmbH, Mannheim) was added. Hybridization of the probe was detected using the Luminescent Image Analyzer LAS-3000 Image analyzer (FUJIFILM Europe GmbH, Düsseldorf).

2.7 Flow cytometry

2.7.1 Determination of absolute cell numbers

Cells were diluted 1:10 in FACS buffer containing 1 µg/ml propidium iodide (Sigma-Aldrich Chemie GmbH, München) and counted using MACSQuant® Analyzer and MACQuantify™ software (Miltenyi Biotec GmbH Germany, Bergisch Gladbach).

2.7.2 Peripheral blood chimerism

To determine the peripheral blood chimerism, one capillary blood was taken from the retro-orbital bulbus of chimeric mice and immediately mixed with 100 µl heparin (1:10 diluted in 1 x PBS, Merck KGaA Germany, Darmstadt) to avoid agglutination of the blood. To obtain white blood cells, 60 µl peripheral blood/heparin-mix was lysed three times in red blood cell lysis buffer. White blood cells were subsequently stained for $CD11b^+$ $Gr1^+$ polymorphonucleated cells (PMNs), $B220^+$ B cells and $CD3^+$ T cells. Donor, competitor and recipient cells were discriminated by staining for CD45.1 and CD45.2.

2.7.3 KSL SLAM staining of E14.5 fetal liver cells and adult bone marrow cells

To enrich for hematopoietic stem cells (HSCs), fetal liver cells and bone marrow cells were incubated with a lineage antibody cocktail, containing biotinylated anti mouse CD19, B220, CD3e, CD4, CD8, CD11b, Nk1.1, Gr1. Cells were additionally incubated with rat immunoglobulin G (IgG) and CD16/32 to prevent unspecific antibody staining to Fc gamma receptor (FcγR). When fetal liver cells were stained for HSCs, CD11b was excluded from the lineage antibody mix. After incubation for 1 hour at 4℃ in the dark, cells were washed three times with FACS buffer and subsequently incubated with CD117 APCeF780, Sca1 PerCP Cy5.5, CD48 APC, CD150 PE Cy7 and anti-biotin Streptavidin Pacific Blue for 1 hour at 4℃ in the dark. In case donor, competitor and recipient had to be discriminated, anti mouse CD45.1 and CD45.2 were added. Cells were washed three times in FACS buffer and resuspended in at least 500 µl FACS buffer. Shortly before FACS analysis, propidium iodide (Sigma-Aldrich Chemie GmbH, München) was added to a final concentration of 1 µg/ml. FACS analysis was either performed on BD FACSAria™ II, BD FACSAria™ III or BD LSR II (Beckton Dickinson Germany, Heidelberg) and analyzed using FlowJo Single Cell Analysis Software (FLOWJO, LLC Data analysis software)

2.7.4 Epidermal stem cell staining

Stem cells from the epidermis were stained according to Jensen et al. (Jensen et al., 2010). Epidermis cells were isolated as described (2.5.5) and subsequently stained in a total volume of 250 µl with CD45 FITC, CD34 eF660, Sca1 PerCP Cy5.5 and CD49f PE. Shortly before FACS analysis, propidium iodide (Sigma-Aldrich Chemie GmbH, München) was added to a final concentration of 1 µg/ml. The addition of CD45 allowed staining for Sca1 expression on epidermal hematopoietic cells. FACS analysis was either performed on BD FACSAria™ II, BD FACSAria™ III or BD LSR II (Beckton Dickinson Germany, Heidelberg) and analyzed using FlowJo Single Cell Analysis Software (FLOWJO, LLC Data analysis software).

2.8 Histology

2.8.1 Paraffin sections

For the generation of paraffin sections, mouse tissues and mouse organs were isolated and fixed in a tenfold excess of 4% formaldehyde (pH 7.4) for at least one day. After

maximal fixation for three days, tissues and organs were trimmed into small samples and subsequently dehydrated using the “Semi-enclosed Benchtop Tissue Processor” Leica TP1020 (Leica Mikrosysteme Vertrieb GmbH Germany, Wetzlar). During the dehydration process, samples were first washed in PBS before sections were dehydrated by a series of ethanol with increasing percentages (70%, 80%, 96% and 99%). Finally ethanol was replaced by xylene. Using the “Modular Tissue Embedding Center” Leica EG1150 (Leica Mikrosysteme Vertrieb GmbH Germany, Wetzlar), samples were casted in paraffin (Paraplast® Plus, Sigma-Aldrich Chemie GmbH, München) and subsequently cut into 6 µm sections using the “Automated Rotary Microtome” RM2265 (Leica Mikrosysteme Vertrieb GmbH Germany, Wetzlar). Depending on the following staining, sample sections were put onto different types of cover slips and dried over night at 37°C.

2.8.2 Hematoxylin and eosin (H&E) staining

Sample sections were placed onto uncoated glass slides and deparaffinized and re-hydrated in a graded alcohol series. Sections were twice incubated for 5 minutes in xylene and subsequently incubated for 2 minutes in 99% ethanol, 96% ethanol, 80% ethanol, 70% ethanol and distilled water, respectively. For H&E staining, sections were first incubated for 2 minutes in Mayer`s hemalm solution before sections were exposed to warm tab water to allow staining of the nuclei. Afterwards, sections were stained with eosin for additional 2 minutes and excess of eosin was removed for 30 seconds in tab water. Finally, H&E stained sample sections were again dehydrated in a graded alcohol series and covered with Entellan (Merck KGaA Germany, Darmstadt). After H&E staining, nuclei appear dark blue or violet, while cytoplasm, elastin and collagen appear pink. Erythrocytes can be detected as yellow or orange dots.

2.8.3 Masson`s trichrome staining

Masson`s trichrome staining of mouse skin sections was performed according to the protocol of the Trichrome Stain (Masson) Kit (Sigma-Aldrich Chemie GmbH, München). Nuclei were stained black with the Weigert`s Iron Hematoxylin solution. Cytoplasm and muscle fibres appeared red, while collagen appeared blue after staining.

2.8.4 Ki67 staining

For Ki67 staining dorsal skin sections were mounted on poly-lysine coated glass slides (POLYSINE® SLIDES, Gerhard Menzel GmbH, Braunschweig). Paraffin-embedded

dorsal mouse skin sections were first deparaffinized at 56℃ for 30 minutes and subsequently re-hydrated in a gradual alcohol series. Sections were three times incubated in fresh xylene for 10 minutes, followed by incubation for 10 minutes in 100% ethanol and 96% ethanol and for 20 minutes in 80% ethanol. Sections were finally washed for 10 minutes in tap water. For epitope exposure, sections were incubated in steamer buffer for one hour in hot steam. After three washing steps in 1x PBS for about 3 minutes each, skin sections were treated with 3% hydrogen peroxide (H_2O_2) for 20 minutes to inactivate endogenous peroxidase. After repeated washing in 1x PBS, sections were blocked for at least one hour in blocking buffer at RT. Sections were incubated with the primary antibody rat anti mouse Ki67 (1:50, DAKO GmbH Germany, Hamburg) at 4℃ over night. Subsequently, sections were incubated with secondary antibody polyclonal rabbit anti rat IgG (biotinylated) (1:200, DAKO GmbH Germany, Hamburg) and tertiary streptavidin HRP (1:300, DAKO GmbH Germany, Hamburg) for at least 1 hour at RT. All incubation steps were performed in a humidified chamber and antibodies were diluted in blocking buffer. After antibody incubation, sections were extensively washed in 1x PBS 3-5 times for 5 minutes each. Ki67-positive cells were detected using the Peroxidase Substrate Kit DAB (Vector Laboratories, Inc., Burlingame), following the recommendations of the vendor. Substrate was left on the sections until Ki67-positive cells were sufficiently brown. Sections were finally counter-stained with methyl green and mounted with Cytoseal 60 (Thermo Fisher Scientific Germany, Frankfurt a. M.).

2.8.5 Detection of phosphorylated H2AX (γH2AX)

Aliquots of 1 x 10^5 cells were washed, centrifuged at 1200 rpm for 5 minutes at RT and resuspended in 200 µl 1% Albumin bovine Fraction V, pH 7.0 (SERVA Electrophoresis GmbH Germany, Heidelberg) in 1 x PBS. Cytospins were generated using the Shandon Cytospin3 device (Thermo Fisher Scientific Germany, Frankfurt a. M.) and low speed centrifugation at 1000 rpm for 2 minutes with medium rotor acceleration onto Superfrost Plus glass slides. Cytospins were dried overnight, briefly washed in 1 x TBS, fixed in 4% paraformaldehyde for 30 minutes, permeabilized in 0.25% Triton X-100 in 1 x TBS for 5 minutes and blocked in 3% BSA in 1 x TBS for at least 1 h at RT. Cells were first incubated with primary anti phospho-Histone-H2AX (Ser139, clone JBW301) (1:500, Merck KGaA Germany, Darmstadt) and subsequently incubated with secondary rabbit anti mouse IgG (H+L) Alexa Fluor 488 (1:500, Life Technologies Germany, Darmstadt) for at least 1h at RT in the dark, respectively. Numbers of γH2AX-foci per cell were determined using the EUROStar fluorescence microscope (EUROIMMUN, Medizinische Labordiagnostik AG Germany, Lübeck) at a 400 x magnification. Cells from Rnaseh2b$^{WT/WT}$ and Rnaseh2b$^{KOF/KOF}$ embryos were counted in a blinded fashion.

2.9 Ribonuclease assays

2.9.1 Protein extraction

Prior to extraction, cells were harvested and washed in 1 x PBS. Cells were first incubated with protein extraction buffer for 10 min on ice before an equal volume of cytoplasmic buffer was added and incubated for additional 10 min. After incubation, cells were pelleted at 12000 rpm for 10 min at 4℃. The supernatant was transferred to a new collection tube and protein concentration was determined using the Bradford assay. Protein concentrations were calculated using a standard curve.

2.9.2 RNase H activity assay

Fluorometric RNase H activity assays were performed according to Crow et al (Crow et al., 2006b) in collaboration with Martin Reijns and Andrew Jackson (Institute of Genetics and Molecular Medicine, University of Edinburgh). Substrates for the determination of RNase H2 activity were as follows: RNA:DNA hybrid (forward strand: 5`-rGrArU-rCrUrG-rArGrC-rCrUrG-rGrGrA-rGrCrU-fluorescein-3`) and DNA_{11}-RNA-DNA_3:DNA (forward strand: 5`-dGdAdT-dCdTdG-dAdGdC-dCdTdG-dGdGrA-dGdCdT-

fluorescein-3`) (desoxyribonucleotde, ribonucleotide). Each forward strand was annealed to the complementary reverse DNA strand (5`-DABCYL-dAdGdC- dTdCdC-dCdAdG-dGdCdT-dCdAcG-dAdTdC-3`). Fluorescent label in the forward strands was quenched by the presence of DABCYL of the reverse strand. Upon RNase H2-mediated cleavage of the substrate, quenching of the fluorescein is released and fluorescence is emitted as light. Thus, RNase H2 activity is determined by light emission over time. For the exact determination of the converted substrate per time, a standard curve was generated ranging from 0.78 pmol to 50 pmol. An unlabeled DNA oligonucleotide was therefore annealed to the forward strands that allows for constant fluorescence.

RNase H2 activity assay was performed in a total volume of 100 µl assay buffer containing 250 nM of the respective substrate and 100 ng / µl cell lysate at an ambient temperature of 37°C. Fluorescence was detected every 5 minutes during a time period of 90 minutes using a VICTOR^3 1420 multi label counter (Perkin Elmer Germany, Rodgau) with a 480 nm excitation filter and a 535 nm emission filter.

2.9.3 Nick translation assay

DNA concentration was determined using the NanoDrop ND-1000 (Thermo Fisher Scientific Germany, Braunschweig). 200 ng of mouse or yeast DNA was digested in 0.5 units *E.coli* RNase HII (New England Biolabs, Frankfurt a.M.) in a total volume of 50 µl for 150 minutes at 37°C. RNase HII-digested DNA was precipitated in the presence of 1 µl glycogen, 0.3 M sodium acetate (pH 5.2) and two volumes of ice cold 100% ethanol. Precipitated DNA was pelleted for 10 minutes at 13000 rpm and RT, quickly dried to allow the ethanol to evaporate and finally dissolved in nuclease-free water. Reagents of the nick translation assay were added to a final concentration of 1 x buffer 2 (New England Biolabs, Frankfurt a.M.), 20 µM unlabeled dATP, dGTP and dTTP. 3.7 x10^5 Bq ^{32}P-dCTP (HARTMANN ANALYTIC GmbH Germany; Braunschweig) and 5 units *E.coli* DNA polymerase I (New England Biolabs, Frankfurt a.M.) in a final reaction volume of 20 µl. Nick translation reaction was performed for 35 minutes at 16°C. Radioactively-labeled DNA was afterwards separated from unincorporated nucleotides by gel electrophoresis in a 1% TAE agarose gel. The gel was dehydrated using a GD 2000 Vacuum Gel Dryer system (GE Healthcare Europe, Freiburg) and label incorporation was visualized by autoradiography using PhosphorImager SI (Molecular Dynamics/GE Healthcare Europe, Freiburg)

2.10 Statistics

All data is shown as mean ± standard deviation (SD). Significances were calculated using the unpaired, two-tailed Fisher`s t-test. $p \leq 0.5$ (*),$p \leq 0.1$ (**).
Due to an outlier in the knockout group, statistics were not calculable in the microarray-based gene expression analysis of the fetal liver. Deregulated genes with a fold change ≥ 2 were displayed. False discovery rates in the microarray-based gene expression analysis of total skin were corrected using the Benjamini-Hochberg correction. Deregulated genes with a fold change ≥ 1.5 and $p \leq 0.5$ were displayed.

3 Results

3.1 Generation and characterization of the *Rnaseh2c* knockout mouse line

To allow the investigation of cell-intrinsic mechanisms that cause the severe inflammatory encephalopathy Aicardi-Goutières syndrome (AGS), this thesis aimed to generate a mouse model for AGS by generating knockout mice deficient for the RNase H2 enzyme. Loss-of-function mutations in any of the three subunits of the ribonuclease H2 (RNase H2) complex cause AGS in human patients (Crow et al., 2006b). We therefore decided to delete the *Rnaseh2c* gene, encoding for the smallest subunit of the mouse RNase H2 enzyme. In order to inactivate the *Rnaseh2c* gene, we replaced all four coding exons by a neomycin resistance cassette that concomitantly allowed for the selection during gene targeting (Fig. 3.1).

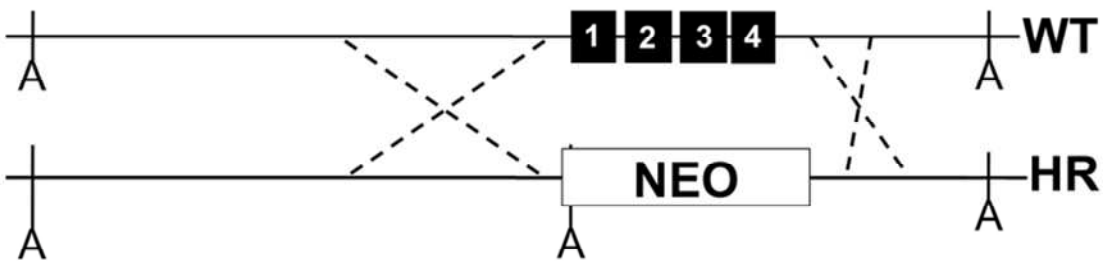

Figure 3.1: Strategy for the generation of the *Rnaseh2c* knockout mouse line. In order to inactivate the mouse *Rnaseh2c* gene, all four exons were replaced by a neomycin resistance cassette. The resistance gene cassette was concomitantly used to select for ES cell clones that had integrated the targeting vector by homologous recombination (HR). By insertion of the neo cassette, an additional ApaLI (A) restriction site was introduced that allowed testing for homologous recombination by Southern Blot analysis.

3.1.1 Generation of the *Rnaseh2c* knockout mouse line

To replace the mouse *Rnaseh2c* gene with a neomycin resistance gene cassette, a targeting vector was generated that contained the neomycin gene flanked by DNA sequences homologous to the upstream and downstream region of the *Rnaseh2c* gene as well as an additional diphtheria toxin (DT) gene 3-prime of homology region 2 that allowed for negative selection of recombined ES cells. For the amplification of the upstream homology region (homology region 1), primers 5′ HR up and 5′ HR down were used to generate a 1810 bp PCR product with an 5` XbaI and a 3` BamHI restriction site. Accordingly, primers 3′ HR up and 3′ HR down amplified the 900 bp downstream homology region (homology region 2) with a 5` HindIII and 3` XhoI restriction site. Both homology regions were amplified on C57BL/6 mouse DNA and PCR products were

sequenced to eliminate mutated PCR products. For the insertion of the PCR products into a pBluescript vector containing a PGK-gb2-neomycin resistance cassette (previously generated in our group), the vector was first digested with the respective combination of restriction enzymes and dephosphorylated in order to prevent religation of the vector. Finally, PCR products of the homology regions were inserted into the pBluescript vector by ligation. Correct insertion was checked by a restriction enzyme digest and subsequent gel electrophoresis. The DT gene cassette was amplified from a pSERC vector (provided by Thomas Wunderlich, Cologne) with primers DT-XhoI-For-New and DT-XhoI-Rev-New, generating XhoI restriction sites at both ends of the PCR product. Again, PCR products were sequenced to avoid any mutation. The pBluescript vector containing the neomycin gene flanked by to homology regions was digested with XhoI, dephosphorylated and the DT gene cassette was inserted downstream of homology region 2. Correct insertion was tested by restriction enzyme digest and gel electrophoresis. Finally, the pBluescript vector (8592bp) containing the neomycin gene cassette flanked by two homology regions and the downstream DT gene cassette was tested for correct size by restriction enzyme digest. Additionally, upstream and downstream homology regions as well as the DT gene cassette were sequenced.

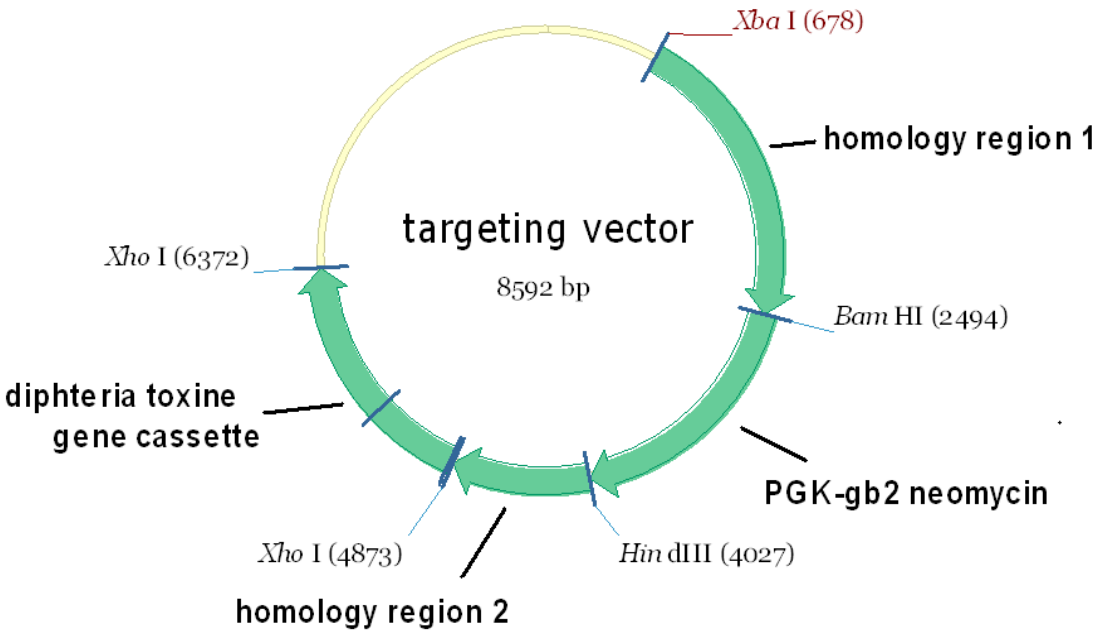

Figure 3.2: Targeting vector to replace all four coding exons of the Rnaseh2c gene by a neomycin resistance cassette. The targeting vector of 8592bp contained a PGK promoter- and gb2 promoter-driven neomycin resistant cassette to facilitate selection for G418-resistance in prokaryotic and eukaryotic cells. The neo cassette was flanked by an 1810bp upstream homology region (homology region 1) and a 900bp downstream homology region (homology region 2) to promote homologous recombination. An additional diphtheria toxine downstream homology region 2 allowed for negative selection of erroneous integrates.

In collaboration with Dora Schreier and Ronald Naumann at the Transgenic Core Facility (TCF) of the Max Planck Institute for Cellular Biology and Genetics (MPI CBG) in Dresden, 30 µg/ml Sac I-linearized targeting vector DNA was electroporated into JM8.F6 ES cells (C57BL/6) using the Gene Pulser Xcell™ Electroporation Systems (BioRad). Electroporated ES cells were subsequently cultivated in the presence of geneticin (G418) to select for ES cells that had integrated the targeting vector. ES cells that erroneously incorporated the diphtheria toxin gene cassette died upon negative selection. Only upon homologous recombination of the targeting vector without the DT cassette and the expression of neomycin resistance gene, ES cells were resistant to G418 selection. G418-resistant ES cell clones were picked into 96 well plates and cultivated until maximum density. Subsequently, DNA was isolated and screened for positive clones using PCR and primers annealing to homology region 2 (HR2seq1 for) and to wild type sequence downstream of the homology region 2 (HR2-est.). Screening PCR amplified a product of 1492bp only upon integration of the targeting vector into the wild type *Rnaseh2c* gene locus. We identified three clones by PCR that were subsequently verified by Southern Blot analysis.

For verification of PCR-positive ES cell clones we took advantage of the additional ApaLI restriction site in the neomycin resistant cassette. Using DIG-labeled RNA probes, annealing upstream and downstream of the homology regions, allowed us to discriminate between the wild type (WT) and recombined (HR) allele. In the wild type situation, the upstream and the downstream probe labeled a DNA fragment of 9.3 kb. Upon homologous recombination the upstream probe labeled a DNA fragment of 5.7 kb while the downstream probe labeled a fragment of 3.6 kb (Fig. 3.3). Homologous recombination of ES cell clone C9 was finally confirmed by Southern Blot analysis (Fig.3.3).

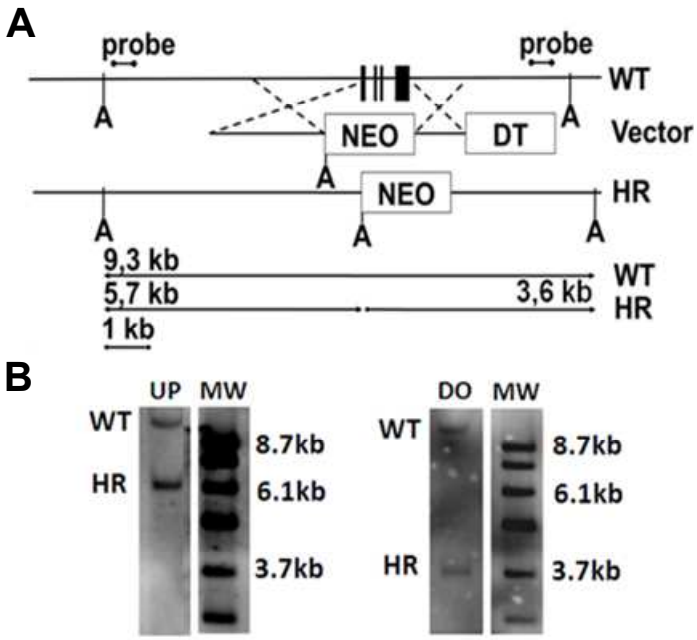

Figure 3.3: Southern Blot strategy to detect site-specific homologous recombination of the targeting vector into the *Rnaseh2c* locus. (A) Upon homologous recombination of the targeting vector, an additional ApaLI (A) restriction site was introduced along with the neomycin resistance gene, allowing for the discrimination between the wild type *Rnaseh2b* allele (WT) and the homologous recombined allele (HR) by Southern Blot analysis. DIG-labeled RNA probes, binding upstream and downstream of the *Rnaseh2c* locus, respectively, detected a single fragment of 9.3 kb in the wild type situation (WT). Upon homologous recombination, the upstream probe detected a 5.7 kb fragment and the downstream probe a 3.6 kb fragment. **(B)** Southern Blot analysis was performed on ApaLI-digested DNA from G418-resistant ES cell clone C9. Upstream (UP) and downstream (DO) probes detected DNA fragments of 5.7 kb and 3.6 kb, respectively, indicating homologous recombination of the targeting vector at the *Rnaseh2c* gene locus. MW, Molecular Weight.

Finally, ES cell clone C9 was injected into morula of albino C57BL/6 mice (C57BL/6J-Tyr<c-2J>) that were subsequently transplanted into CD1 foster mice Hsd:ICR(CD-1) We detected a single male pup with a high degree of coat color chimerism in the first litter. To check for germ-line transmission of the recombined ES cells, this founder chimera was bred to wild type albino C57BL/6 female mice. Only upon germline transmission of the ES cells, offspring with black coat color was born (Fig. 3.4). Pups with black coat color were subsequently genotyped by PCR for presence of the neomycin resistance gene cassette.

Figure 3.4: Newborn litter of the founder chimera and an albino C57BL/6 mouse. Breeding of the founder coat-color chimera to albino C57BL/6 mice tested germ-line transmission of the ES cell clone C9. Only upon germ line transmission, pups with black coat-color were born.

3.1.2 Characterization of the *Rnaseh2c* knockout mouse line

Heterozygous *Rnaseh2c* knockout mice (*Rnaseh2c*$^{+/-}$) were intercrossed to obtain homozygous knockout mice. Genotyping PCR of weaned litter displayed no homozygous *Rnaseh2c* knockout mice (*Rnaseh2c*$^{-/-}$) (Fig. 3.5), suggesting lethality of *Rnaseh2c*$^{-/-}$ mice during embryogenesis. To verify this and to determine the time point of lethality, timed breedings were set and embryos were collected at embryonic day 10.5 (E10.5) by caesarian section. We observed few embryos with abnormal morphology. Genotyping PCR of E10.5 *Rnaseh2c* knockout embryos identified these abnormal embryos as *Rnaseh2c*$^{-/-}$ embryos. Due to their abnormal morphology and their non-Mendelian distribution we concluded that RNase H2-deficient embryos start to degrade early in embryogenesis but are almost entirely reabsorbed at day E10.5. Collectively, this data demonstrates the importance of the RNase H2 enzyme during mouse development. Deficiency of the enzyme causes death and subsequent degradation in early embryonic development.

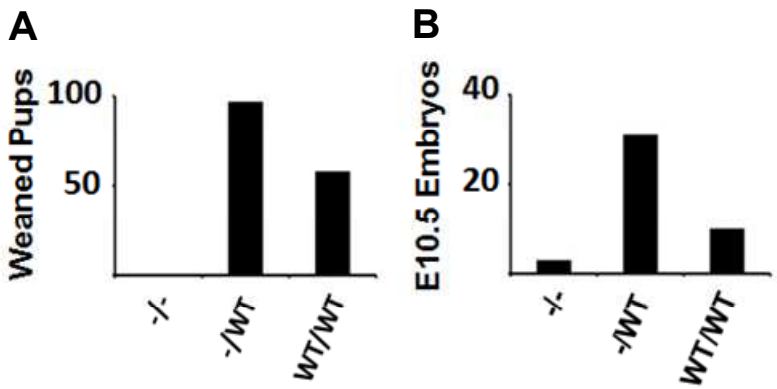

Figure 3.5: Breeding of Rnaseh2c$^{-/WT-}$ mice to homozygosity. To obtain *Rnaseh2c*$^{-/-}$ mice, heterozygous Rnaseh2c mice were crossed. **(A)** At weaning, no *Rnaseh2c*$^{-/-}$ mouse was observed. **(B)** Upon caesarian section at day E10.5, *Rnaseh2c*$^{-/-}$ embryos were detected which were characterized by non-Mendelian distribution and abnormal morphology, indicating degradation at earlier time points.

3.2 Analysis of the *Rnaseh2b KOF* mouse line

During the generation and investigation of the *Rnaseh2c* knockout mouse line, we started to analyze the *Rnaseh2b KOF* mouse line, not knowing that deficiency of the *Rnaseh2c* gene was embryonic lethal. The *Rnaseh2b KOF* mouse line was generated by the European Conditional Mouse Mutagenesis Program (EUCOMM, (Friedel et al., 2007)) by inserting a promoter-less reporter cassette into intron 4/5 of the *Rnaseh2b* gene (Fig. 3.6). Main feature of the reporter cassette is a strong splice acceptor (EN2 SA) at its 5`-terminus that is supposed to splice to exon 4 of the *Rnaseh2b* gene, thus terminating mRNA translation due to a polyadenylation sequence (pA) at the 3`-end of the reporter cassette. Collectively, *Rnaseh2b*$^{KOF/KOF}$ mice are supposed to express a non-functional and truncated RNase H2b protein that causes complete RNase H2 deficiency (Testa et al., 2004).

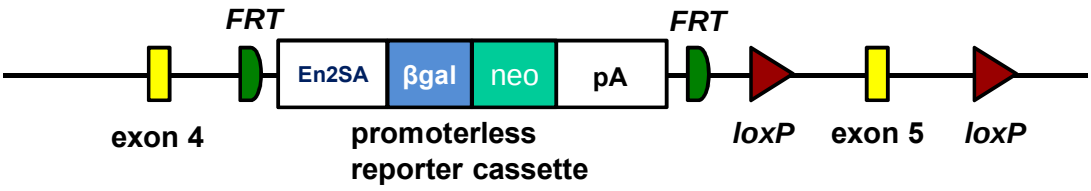

Figure 3.6: Schematic overview of the promoterless reporter cassette used to knockout the *Rnaseh2b* gene. To inactivate the *Rnaseh2b* gene, a promoterless reporter cassette was inserted into intron 4/5 of the *Rnaseh2b* gene locus. The strong splice acceptor EN2SA directs splicing to exon 4, generating gene transcripts containing sequence of the reporter cassette. Translation of these transcripts is subsequently terminated due to the presence of the polyadenylation signal (pA) at the terminus of the reporter cassette. The cassette also contains a β-galactosidase reporter (βgal) as well a neomycin resistance cassette (neo).

We obtained *Rnaseh2b*$^{WT/KOF}$ mice from EUCOMM and intercrossed heterozygous mice to obtain *Rnaseh2b*$^{KOF/KOF}$ mice. However, we did not observe any *Rnaseh2b*$^{KOF/KOF}$ pups at weaning. Upon subsequent inspection of the newborn litter, we could observe seven dead newborns that displayed morphological changes when compared to littermate controls. Genotyping identified these newborns as *Rnaseh2b*$^{KOF/KOF}$ mice. When compared to their littermate controls (*Rnaseh2b*$^{WT/KOF}$ and *Rnaseh2b*$^{WT/WT}$), *Rnaseh2b*$^{KOF/KOF}$ newborn mice were much smaller in size, showed abnormal morphology and were stillborn (Fig. 3.7). To investigate the time point of lethality, we set timed breedings and isolated embryos at embryonic day E14.5 and E18.5. We found *Rnaseh2b*$^{KOF/KOF}$ embryos at Mendelian ratios at embryonic day 14.5 and 18.5. Again, knockout embryos were smaller in size and revealed edema and paleness when compared to littermate controls (Fig. 3.7). We hypothesized that paleness in RNase H2-deficient embryos was indicative of reduced blood supply that might have caused embryonic lethality.

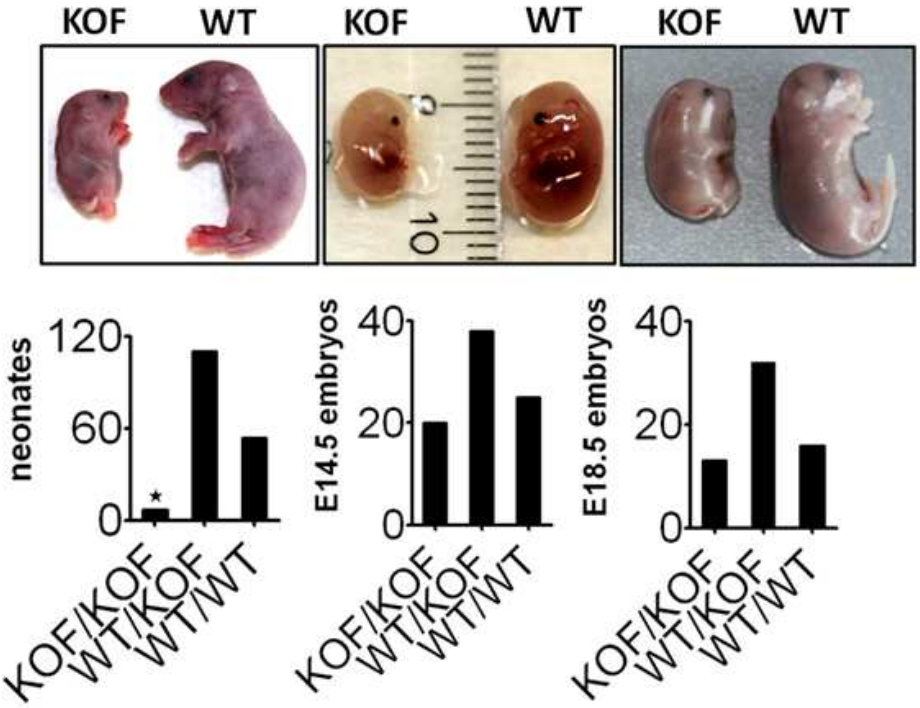

Figure 3.7: *Rnaseh2b KOF* litter at weaning and at embryonic day E14.5 and E18.5. *Rnaseh2b*$^{WT/KOF}$ mice were crossed to obtain *Rnaseh2b*$^{KOF/KOF}$ mice. No *Rnaseh2b*$^{KOF/KOF}$ newborn mouse could be identified after weaning. Upon inspection of the litter, we found seven stillborn *Rnaseh2b*$^{KOF/KOF}$ mice. At embryonic day E14.5 and E18.5 of mouse development, *Rnaseh2b*$^{KOF/KOF}$ mice were present at Mendelian ratios, but appeared smaller and showed signs of edema and paleness.

Analysis of H&E-stained paraffin-sections of stillborn *Rnaseh2b*$^{KOF/KOF}$ mice did not reveal major conspicuities, all organs were present but proportionally smaller in size

(data not shown). Additionally, no signs of inflammation, like leukocyte-infiltrations, could be detected. Silke Glage at the institute for laboratory animal science in Hannover performed detailed analysis of stillborn sections and revealed edema in many organs as well as extended vessels and bleedings, suggesting defects in vessel wall architecture (data not shown).

However, since the pathology of *Trex1*$^{-/-}$ mice was completely dependent on an unbalanced type I interferon expression and could be completely rescued by breeding of the *Trex1*$^{-/-}$ mouse on either a RAG1-, IRF3- or IFNAR1-deficient background (Stetson et al., 2008), we aimed to rescue the lethal embryonic phenotype of RNase H2-deficient mice by breeding the *Rnaseh2b KOF* mouse line on a Rag1- (Mombaerts et al., 1992) and Ifnar1-deficient (Muller et al., 1994) background, respectively (Fig. 3.8). Neither RAG1- nor IFNAR1-deficiency could rescue the lethal phenotype of *Rnaseh2b* knockout mice, indicating that lethality of *Rnaseh2b*-deficient mice was not caused by type I interferon or mediated by lymphocytes.

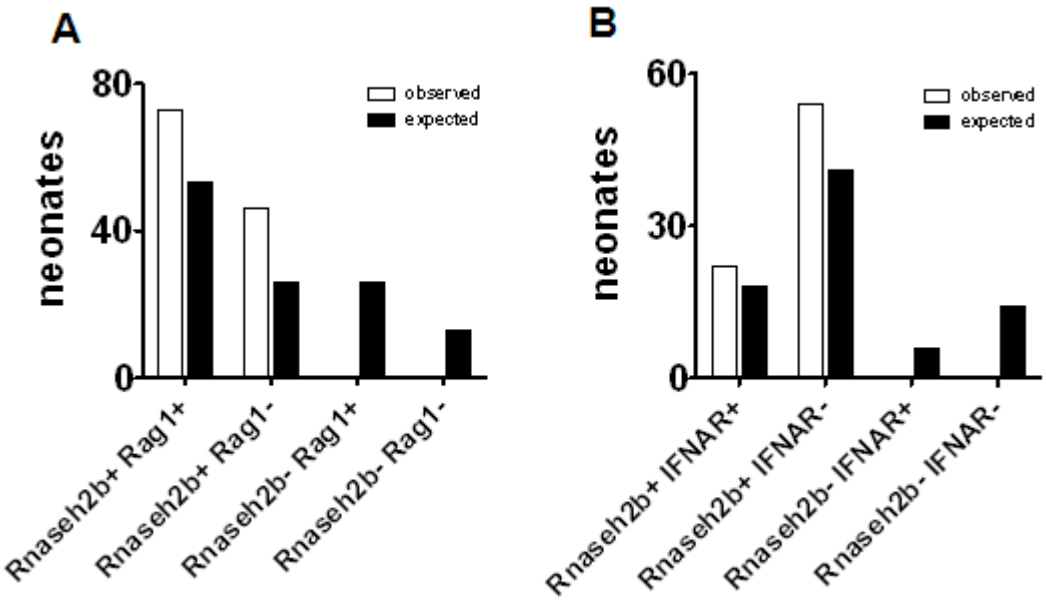

Figure 3.8: Breeding of RNase H2b-deficent mice on a RAG1- and IFNAR-deficient background did not rescue early embryonic lethality. To rescue the embryonic lethality of *Rnaseh2b*$^{KOF/KOF}$ mice, the *Rnaseh2b KOF* mouse line was bred to a **(A)** Rag1- and **(B)** Ifnar1-deficient background, respectively. Neither Rag1- nor Ifnar1 deficiency rescued the lethality, indicating that mortality of *Rnaseh2b*$^{KOF/KOF}$ mice is not caused by a type I interferon response or mediated by lymphocytes. Black bars indicate observed and grey bars indicate expected newborns.

Collectively, our data demonstrated that *Rnaseh2b*$^{KOF/KOF}$ mice were stillborn and lethality could not be rescued by breeding on a RAG1- or IFNAR1-deficient background, obviating that the pathology of RNase H2-deficient mice was mediated by a unbalanced type I interferon as in *Trex1*$^{-/-}$ mice. *Rnaseh2b*$^{KOF/KOF}$ embryos at day E14.5 and E18.5

were present at Mendelian ratios but displayed edema and paleness, indicative of decreased blood supply. Together with the tissue bleedings, these findings might hint to impaired vessel wall functions.

3.2.1 Mouse embryonic fibroblasts from *Rnaseh2b*$^{KOF/KOF}$ mice display impaired proliferation and progress slower through the G2/M phase of the cell cycle

Aiming to investigate the pathomechanism responsible for the early embryonic lethality in *Rnaseh2b*$^{KOF/KOF}$ mice, we bypassed lethality by generating mouse embryonic fibroblasts (MEFs) from mouse embryos at day E14.5. Since *Rnaseh2b*$^{KOF/KOF}$ mice show extended life span compared to *Rnaseh2c*$^{-/-}$ mice, we first determined the residual *Rnaseh2b* transcript levels and RNase H2 enzyme activity of MEFs from E14.5 *Rnaseh2b*$^{KOF/KOF}$ embryos. *Rnaseh2b* transcript levels were determined using exon-spanning primers annealing to exonic DNA sequences downstream of the gene trap cassette, allowing for the detection of full-length transcripts. Quantitative real time PCR (qRT PCR) of RNA extracted from *Rnaseh2b*$^{KOF/KOF}$ MEFs showed massive downregulation of *Rnaseh2b* transcripts when compared to RNA from wild type littermate control MEFs (49.49 ± 16.29 fold) (Fig.3.9). However, we were still able to detect wild type *Rnaseh2b* transcripts in MEFs from *Rnaseh2b*$^{KOF/KOF}$ embryos, suggesting that low residual *Rnaseh2b* transcript levels resulted from splicing of exon 4 to exon 5. Upon correct splicing, the gene trap cassette is lost and a wild type transcript is generated (Fig. 3.6). In collaboration with Martin Reijns and Andrew Jackson at the Institute of Genetics and Molecular Medicine (University of Edinburgh) we further determined the residual activity of the RNase H2 enzyme in *Rnaseh2b*-deficient MEFs using an RNase H2-specific fluorometric assay (Fig. 3.9). In line with the detection of residual wild type Rnaseh2b transcripts, the RNase H2 activity assay displayed low residual activity of about 6% in *Rnaseh2b*$^{KOF/KOF}$ MEF cells (n=2) compared to wild type (100%, n=2) and heterozygous MEF cells (68%, n=2) (Fig. 3.9). Taken together, our data demonstrated that *Rnaseh2b*$^{KOF/KOF}$ MEFs were not completely devoid of wild type *Rnaseh2b* transcripts, but expressed low levels of the RNase H2 enzyme. This residual enzyme activity of about 6% leads to prolonged embryonic development compared to *Rnaseh2c*$^{-/-}$ mice. However, our data concomitantly showed that 6% residual RNase H2 activity did not allow further development and adult life.

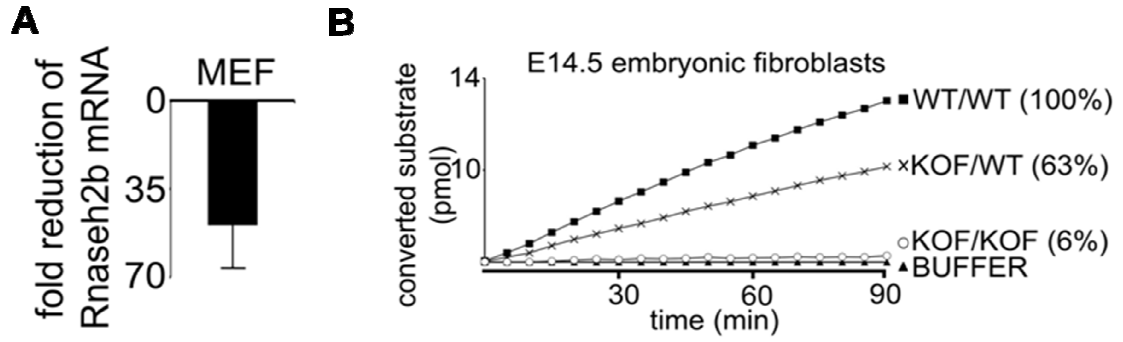

Figure 3.9: Identification of residual wild type transcript levels and RNase H2 enzyme activity in *Rnaseh2b*$^{KOF/KOF}$ MEFs. (A) Wild type transcript levels were determined in total RNA from E14.5 *Rnaseh2b*$^{KOF/KOF}$ MEFs and littermate controls by quantitative real time PCR (qRT PCR). Using primers annealing downstream of the reporter cassette, only wild type transcripts could be detected. Fold change was calculated by pair wise comparison and normalization to the housekeeping gene beta actin. **(B)** Residual enzyme activity was calculated by an RNase H2-specific enzyme activity assay. Cleavage of an RNase H2-specific oligonucleotide substrate led to fluorescence emission that was detected over time. Fluorescence was used to calculate the converted substrate (pmol) over time. Residual RNase H2 activity in *Rnaseh2b*$^{KOF/KOF}$ MEFs (KOF/KOF, n=2) was reduced to 6% of wild type MEFs (WT/WT, n=2), whereas residual activity in *Rnaseh2b*$^{KOF/WT}$ MEFs (KOF/WT, n=2) was reduced to 67%.

During the cultivation of MEFs from *Rnaseh2b*$^{KOF/KOF}$ embryos we observed impaired proliferation and increased cell sizes, when compared to control MEFs. A ^{3}H-thymidine incorporation assay confirmed that observation. One week after cultivation start, *Rnaseh2b*$^{KOF/KOF}$ MEFs (48127 ± 5430 counts per minute (cpm), n=3) showed twofold less incorporation of radioactively-labeled thymidine in comparison to control MEFs encompassing wild type as well as heterozygous MEFs (100798 ± 12577 cpm, n=9) (Fig. 3.10). Whereas the proliferation of control MEFs remained constant over a period of four weeks, proliferation of *Rnaseh2b*$^{KOF/KOF}$ MEFs exacerbated during this time and four weeks after cultivation start, proliferation in knockout MEFs was reduced by factor five (16164 ± 11494 cpm, n=3) when compared to the controls (94836 ± 34885 cpm, n=6) (Fig. 3.10), indicating that RNase H2 deficiency likely caused cell-intrinsic problems that led to impaired proliferation. We subsequently performed DNA content analysis, aiming to elucidate whether impaired proliferation was a consequence of impaired cell cycle progression in *Rnaseh2b*-deficient cells. We generated MEFs from E14.5 Rnaseh2b KOF embryos and determined the DNA content after one and four weeks of cultivation. After one week, wild type MEF cells were predominantly in G1, with a few cells being in S or G2/M phase of the cell cycle. After four weeks the number of cells in G2/M mildly increased, with most of the cells still in G1 (Fig. 3.10). In contrast, more RNase H2-deficient cells were in G2/M of the cell cycle already after the first week of cultivation. Moreover, the number of RNase H2-deficient MEFs dramatically increased after four weeks with almost half of the cells in G2/M of the cell cycle. When MEF cells were

generated from E18.5 embryos, the number of cells in G2/M further increased in *Rnaseh2b*$^{KOF/KOF}$ MEFs. After four weeks, most of the cells accumulated in G2/M of the cell cycle. This data showed that RNase H2 is important for cell cycle progression and cell proliferation, while absence leads to slow progression or accumulation of cells in the G2/M phase of the cell cycle. Together with the data from the ^{3}H-thymidine incorporation assay, we concluded that RNase H2 deficiency caused major cell-intrinsic problems, leading to impaired proliferation rates and slow progression or accumulation of MEF cells in the G2/M phase of the cell cycle. Since the number of accumulated cells in G2/M gradually increased, we speculated that the cell-intrinsic problem accumulated with every cell division, although the species of the cell-intrinsic problem is so far unknown and needs to be elucidated.

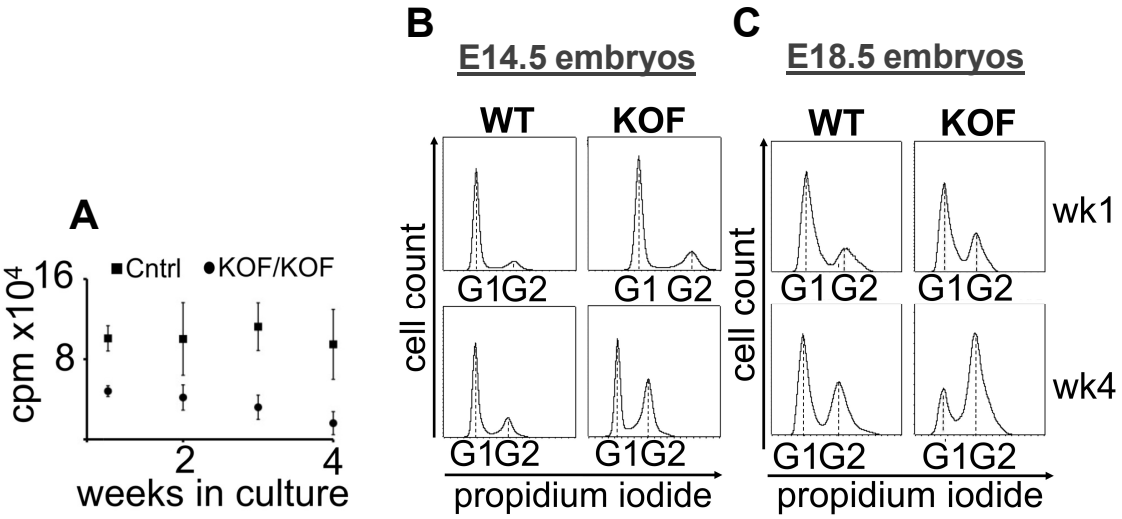

Figure 3.10: RNase H2-deficient mouse embryonic fibroblasts (MEFs) from E14.5 embryos show impaired proliferation rates and slow progression through G2/M phase of the cell cycle. (A) ^{3}H-thymidine incorporation assay to detect MEF cell proliferation. MEFs generated from E14.5 *Rnaseh2b*$^{KOF/KOF}$ embryos display twofold less proliferation rates with cultivation start that further gradually exacerbated. After four weeks of cultivation, proliferation of *Rnaseh2b*$^{KOF/KOF}$MEFs (n=3) was fivefold decreased when compared to control MEFs (Cntrl, n=9). **(B/C)** DNA content analysis showed increased numbers of RNase H2-deficient cells in the G2/M phase of the cell cycle already after one week of cultivation. After four weeks, almost half of the cells were already in G2/M. **(C)** MEF cells generated from E18.5 *Rnaseh2b*$^{KOF/KOF}$ embryos accumulated almost entirely in the G2/M phase of the cell cycle after four weeks.

3.2.2 p53-mediated DNA damage response in fetal liver cells from *Rnaseh2b*$^{KOF/KOF}$ embryos

Since mouse embryonic fibroblasts from E14.5 *Rnaseh2b*$^{KOF/KOF}$ embryos displayed reduced proliferation rates and slow progression through the G2/M phase of the cell cycle, we hypothesized that RNase H2 deficiency might have caused DNA damage that

activated a DNA damage response (DDR) and triggered checkpoint activation in G2/M. To prevent the propagation of mutated genomic information to the progeny, DNA is first repaired before it is distributed to the daughter cells. DNA damage elicits a DNA damage response that causes checkpoint activation and cell cycle arrest to allow for the repair of the damage (Jackson and Bartek, 2009). To obtain maximal information about the consequences of RNase H2 deficiency, we performed a microarray-based gene expression analysis of E14.5 fetal liver cells from *Rnaseh2b*$^{KOF/KOF}$ versus wild type littermate embryos. Upon pair-wise comparison of *Rnaseh2b*$^{WT/WT}$ (n=3) and *Rnaseh2b*$^{KOF/KOF}$ (n=3) E14.5 fetal liver cells, 882 genes were found to be at least twofold de-regulated (Fig. 3.11) (GEO database accession no. GSE36687). Of the 882 de-regulated genes, 748 were found to be down-regulated and 134 to be up-regulated. The most down-regulated gene was the *Rnaseh2b* gene (18.5 fold, $p = 2.78^{-5}$) demonstrating the reliability of the microarray analysis. Looking for prototypic DNA damage response genes, we did not observe deregulation of the genes encoding for the kinases ATM/ATR or CHEK1/CHEK2. Although we did not observe the upregulation of these DNA damage response (DDR) genes, we detected the upregulation of genes that are activated by the tumor suppressor gene *TP53* (*p53*). p53 is an immediate target gene of the DNA damage repair pathways upon DNA double- and single-strand breaks, thus implicating the presence of a DNA damage response in RNase H2-deficient fetal liver cells of E14.5 embryos. Four p53-activated genes (*Phlda3*, *Isg15* and *Zmat3*) could be found among the top seven up-regulated genes, with the cyclin-dependent kinase inhibitor 1a (*Cdkn1a*/*p21*) being the most up-regulated gene (10.2 fold, $p = 8.49^{-5}$). Microarray data was subsequently verified by quantitative real-time PCR (Fig. 3.11).

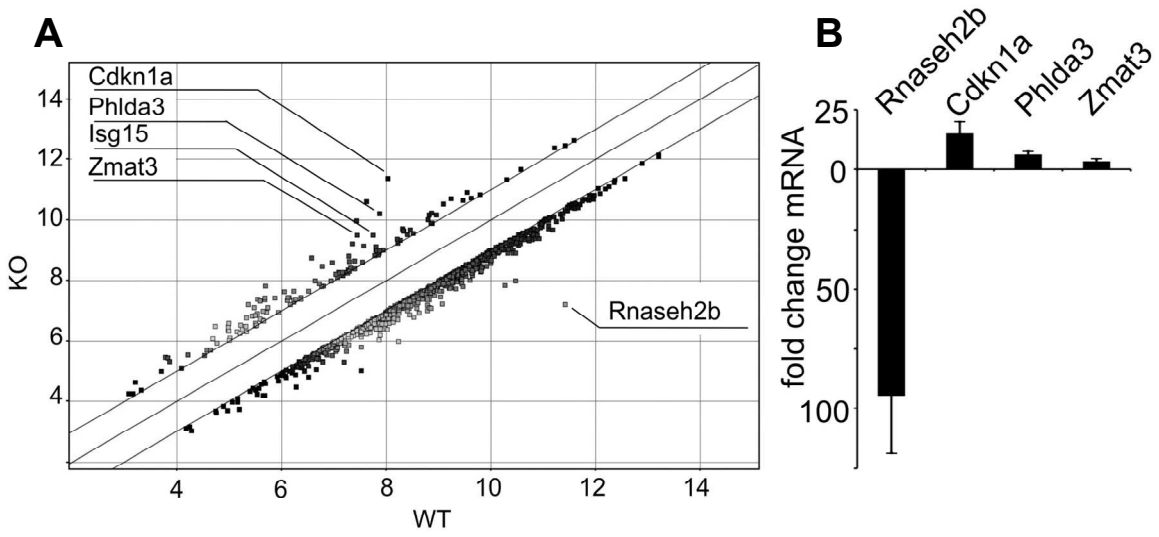

Figure 3.11: Microarray-based gene expression profile of E14.5 *Rnaseh2b*$^{KOF/KOF}$ fetal liver cells revealed upregulation of p53-inducible genes. (A) Pair wise comparison of RNA from three Rnaseh2b$^{KOF/KOF}$ (KO) fetal livers versus three wild type fetal livers (WT) demonstrated deregulation of 882 genes. Each dot in the figure represents a single gene with at least twofold deregulation. Genes with less deregulation are not displayed leaving the empty diagonal. Dots above the diagonal are found to up-regulated whereas dots below the diagonal are down-regulated in the *Rnaseh2b*$^{KOF/KOF}$ fetal liver. Among the top seven up-regulated genes, four are described to be p53-inducible with *Cdkn1a* being the most up-regulated gene. **(B)** Increased transcript levels of the *Rnaseh2b*, *Cdkn1a*, *Phlda3* and the *Zmat3* gene was confirmed by qRT PCR of total RNA from fetal livers.

Although we demonstrated that the lethal phenotype of *Rnaseh2b*-deficient mice was not mediated by type I interferon (Fig. 3.8), we found four type I interferon-stimulated genes (ISGs) to be up-regulated, e.g. interferon regulatory factor 7 (*Irf7*) and the 2`-5`oligoadenylate synthetase 1a (*Oas1a*). However, to investigate if p53 activation was caused by a DNA damage response to DNA strand breaks, we stained E18.5 fetal liver and thymus cells for phosphorylated histone H2AX (γH2AX), a marker for double- and single strand breaks (Rogakou et al., 1998). Repair of DNA strand breaks is mediated by a plethora of DNA repair proteins that need to have access to the DNA strand break. Phosphorylation of serine 139 of the histone H2AX initiates the unwinding of the chromatin and subsequent binding of the repair proteins to the DNA. Since large complexes are subsequently formed, γH2AX bound to the chromatin of damaged cells can be detected as distinct foci. Staining E18.5 fetal liver and thymus cells for phosphorylated histone H2AX elucidated increased numbers of foci in RNase H2-deficient cells when compared to cells from littermate controls (Fig. 3.12). Whereas the majority of control cells displayed 0 - 2 foci per cell, cells from RNase H2-deficient embryos contained more than 2 foci with the majority of cells containing more than five foci. Collectively, our data showed that RNase H2 deficiency likely caused DNA strand breaks that might have triggered a p53-mediated DNA damage response as well as

checkpoint activation and proliferation arrest in G2/M of the cell cycle. However, based on our observations we cannot specify the exact species of the DNA damage, since phosphorylated histone H2AX as well as the p53-mediated DNA damage can be detected upon DNA double-strand and single-strand breaks.

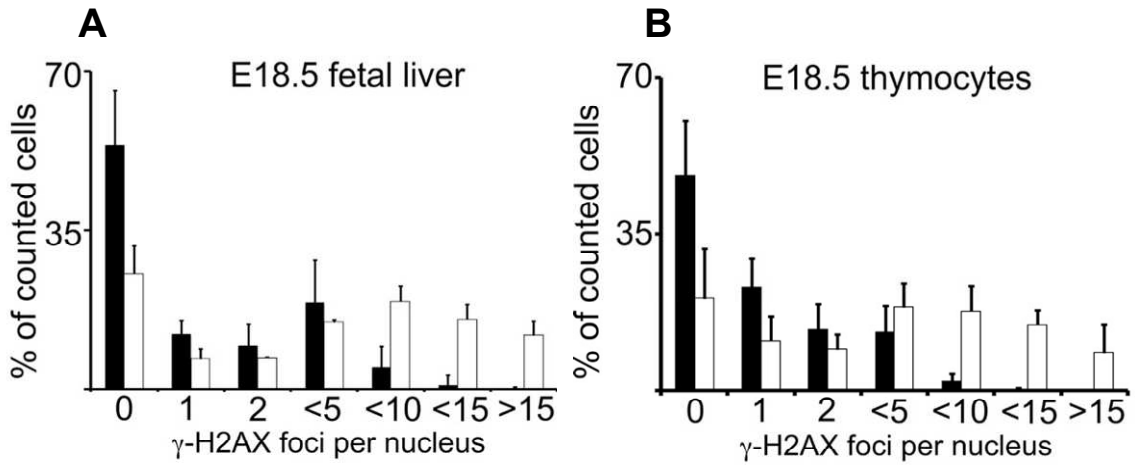

Figure 3.12: Immunostaining for the DNA strand break-specific marker γH2AX in E18.5 fetal liver and thymus cells revealed increased DNA damage in RNase H2-deficient cells. γH2AX foci were counted in **(A)** *Rnaseh2b*$^{KOF/KOF}$ (white columns, n=4) and control (black columns, n=9) fetal liver cells as well as in **(B)** *Rnaseh2b*$^{KOF/KOF}$ (white, n=4) and control (black, n=9) fetal thymus cells of E18.5 *Rnaseh2b KOF* embryos. Increased numbers of γH2AX foci could be detected in E18.5 fetal liver as well as in fetal thymus cells. 400 cells per sample were counted in a blinded fashion.

3.2.3 Increased ribonucleotide incorporation into the genome of RNase H2-deficient mice

McElhinny et al. were the first to show in the yeast strain *Saccharomyces cerevisiae* (*S. cerevisiae*) that RNase H2 deficiency (rnh201Δ) caused increased genomic ribonucleotide loads (Nick McElhinny et al., 2010). Using a yeast strain possessing a mutated leading strand DNA polymerase ε (M644G Pol ε) that frequently incorporated ribonucleotides when compared to wild type polymerase ε, they could show even increased loads of genomic ribonucleotides. Due to their reactive 2`hydroxyl group, ribonucleotides render the genomic DNA sensitive to hydrolysis, a property that was used to detect genomic ribonucleotide levels (Joyce, 1997). Alkaline treatment of DNA containing ribonucleotides causes hydrolysis of the DNA at positions of persistent ribonucleotides and subsequent gel electrophoresis separates DNA fragments. While DNA containing ribonucleotides fragments upon alkaline treatment, ribonucleotide-free DNA remains stable.

Since the alkaline assay to detect genomic ribonucleotides did not work in our hands, we developed a new method to detect ribonucleotide incorporation that was based on the nick translation assay (Fig. 3.13). The nick translation assay was traditionally used to generate radioactively-labeled DNA probes. To this end, PCR products were randomly nicked using the endonuclease DNase I. Subsequent incubation with polymerase I in the presence of radioactively-labeled desoxyribonucleotides caused incorporation of radioactive label. Instead of using DNase I to nick the DNA template randomly, we employed the bacterial RNase HII from *Escherichia coli* (*E. coli*) to specifically introduce nicks 5` of genomic ribonucleotides. As in the traditional nick translation assay, RNase HII-digested DNA was subsequently incubated with *E. coli* DNA polymerase I in the presence of radioactive label. To elucidate ribonucleotide incorporation, RNase HII- and polymerase I-treated DNA was first separated by gel electrophoresis and label was subsequently detected by autoradiography.

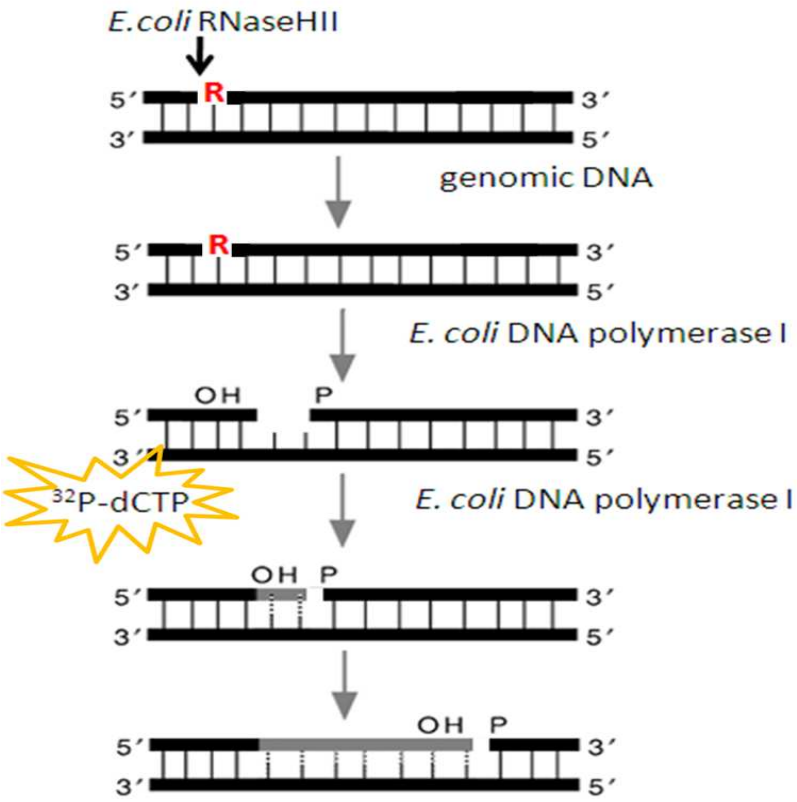

Figure 3.13: Modification of the nick translation assay to detect the presence of genomic ribonucleotides. Genomic DNA is isolated and digested with *E.coli* RNase HII to specifically nick the DNA 5` of genomic ribonucleotides. Subsequent incubation with *E.coli* polymerase I in the presence of radioactively-labeled desoxyribonucleotides, leads to the incorporation of radioactive label at positions of genomic ribonucleotides. Labeled DNA is separated from excessive nucleotides by gel electrophoresis and radioactivity is detected by autoradiography.

We established the modified nick translation assay using wild type and RNase H2-deficient (rnh201Δ) yeast DNA that was already described to contain genomic ribonucleotides (kindly provided by Thomas Kunkel, National Institute of Environmental Health Sciences, North Carolina). Optimal reaction conditions were found for digestion of 200 ng DNA with 0.5 u *E.coli* RNase HII for two and a half hours and subsequent treatment with 5 u *E. coli* polymerase I for 35 min at 16℃. (25012012). Figur e 3.14 shows dose-dependent increase of radioactive label in RNase HII-digested DNA from the yeast strain rnh201Δ. A similar increase could not be detected for RNase HII-digested DNA from wild type yeast (Ctrl).

To test ribonucleotide incorporation in RNase H2-deficient mice, we isolated DNA from E10.5 embryos completely deficient for the RNase H2 enzyme (RNaseh2c$^{-/-}$ and Rnaseh2b$^{\Delta/\Delta}$) as well as from littermate controls. To this end, timed breedings were set and embryos were collected at E10.5 upon caesarian section. The DNA was carefully isolated to avoid any shearing of the DNA and either digested with or without *E. coli* RNase HII enzyme.

As shown in Fig. 3.14, RNase HII-digested DNA from RNaseh2c$^{-/-}$ (n=3) and Rnaseh2b$^{\Delta/\Delta}$ (n=2) embryos consistently showed increased ribonucleotide loads when compared with digested DNA from wild type littermates (Ctrl, n=2 and n=2, respectively) in all samples tested. This data clearly demonstrated increased genomic ribonucleotides in the DNA of RNase H2-deficient mouse embryos. Surprisingly, we could hardly detect any incorporation of radioactive label into the DNA of wild type littermate controls. Although, we do not know the sensitivity of our assay to detect genomic ribonucleotide loads, this data might indicate that endogenous RNase H2 activity efficiently removes incorporated ribonucleotides in the wild type mouse DNA. However, the absence of the RNase H2 enzyme caused massive accumulation of genomic ribonucleotides in the mouse DNA and either the ribonucleotides themselves or the resulting DNA damage (DNA single- or double-strand breaks) cause a DNA damage response that leads to the activation of DNA repair pathways via the tumor suppressor p53. The phosphorylation of histone H2AX might thus occur as a direct consequence of the DNA damage. The presence of radioactive label in undigested DNA samples from RNase H2-deficient embryos might reflect the process of denaturing and resorption of the dying embryo, but might also indicate that persistent genomic ribonucleotides might cause DNA strand breaks, potentially due to the reactive 2` OH group of the ribonucleotide.

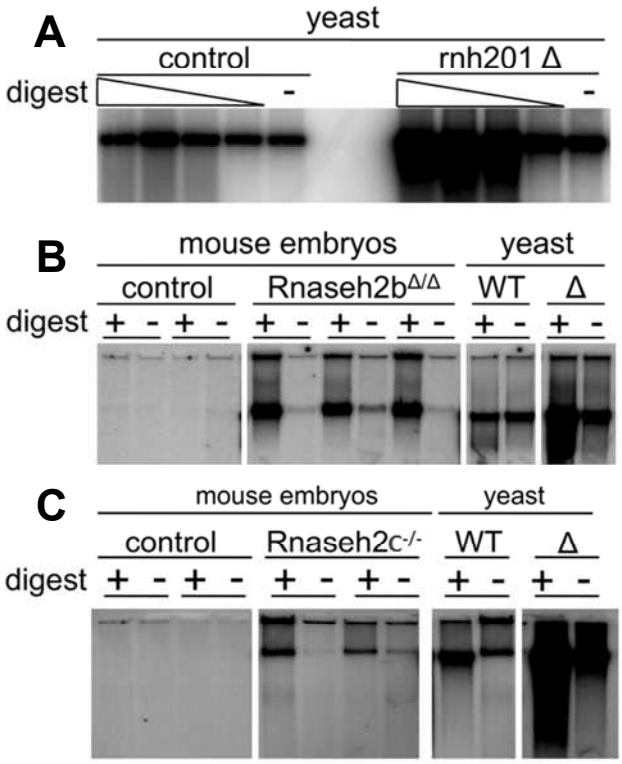

Figure 3.14: Increased ribonucleotide incorporation in genomic DNA from RNase H2-deficient mice. (A) Increased incorporation of radioactive label in a dose-dependent manner (1 – 10 mU/µl) into DNA from RNase H2-deficient yeast (rnh201 Δ). An increased incorporation was not detectable in RNase HII-digested DNA from wild type yeast (control). **(B/C)** DNA from RNase H2-deficient mouse embryos (*Rnaseh2c*$^{-/-}$ and *Rnaseh2b*$^{Δ/Δ}$) showed massive incorporation of label, demonstrating increased ribonucleotide levels in these embryos. In contrast to DNA from knockout embryos, no label could be detected in in DNA from wild type mouse embryos (WT). Undigested DNA from *Rnaseh2c*$^{-/-}$ and *Rnaseh2b*$^{Δ/Δ}$ embryos displayed label incorporation, indicating that DNA from RNase H2-deficient embryos might either contain DNA strand-breaks as a consequence of RNase H2 deficiency or DNA was fragmented in the course of the degradation and resorption of the dying embryo.

3.3 Generation of cell type-specific Rnaseh2b knockouts

To bypass early embryonic lethality of *Rnaseh2b*$^{KOF/KOF}$ mice, we generated cell type-specific knockouts of the *Rnaseh2b* gene. Thus, we first generated the *Rnaseh2b*^{FLOX} mouse line by breeding the *RNaseh2b KOF* mouse with the *Flpe* mouse (Rodriguez et al., 2000)(Fig. 3.15). The *Flpe* mouse strain expresses an enhanced version of the flip recombinase that recognizes and specifically deletes DNA sequences that are flanked by *FRT* sites. Upon mating of both mouse lines, the *FRT*-flanked genetrap cassette was excised and the *Rnaseh2b*^{FLOX} mouse line was generated (Fig. 3.15). Subsequent *Cre*-mediated deletion of exon 5 leads to a frameshift mutation and a premature stop codon that either causes nonsense mediated decay of the transcript or a truncated, non-functional protein (Fig. 3.15).

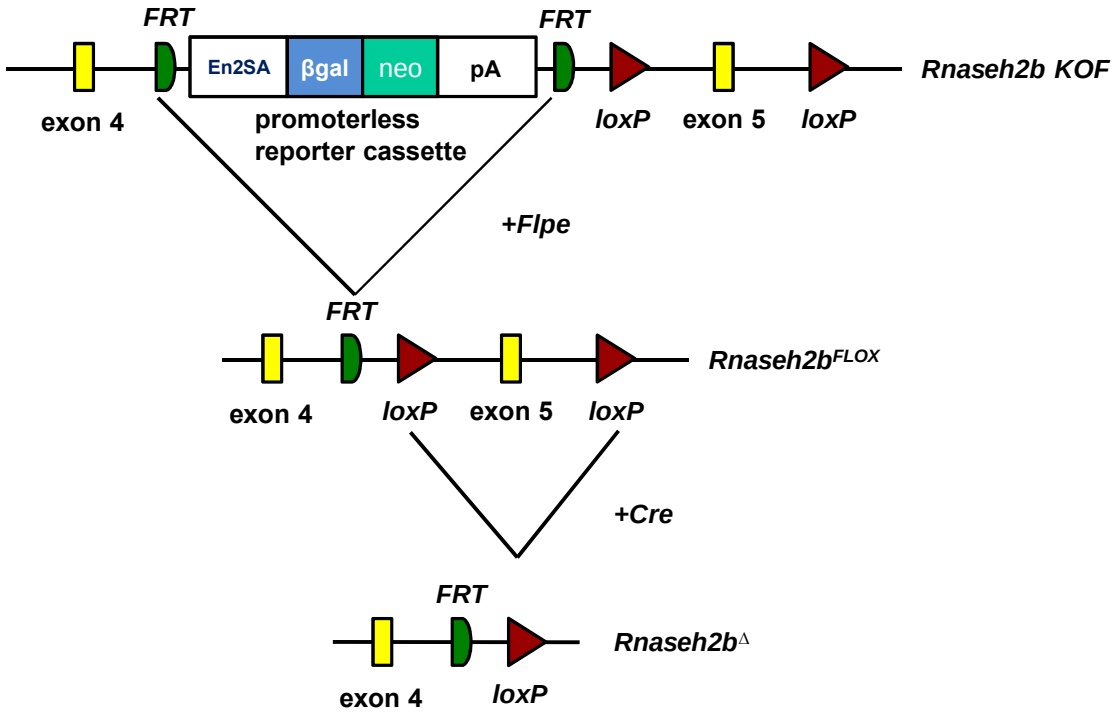

Figure 3.15: Generation of the *Rnaseh2b*^{FLOX} and *Rnaseh2b*$^{\Delta\Delta}$ allele. Flip recombinase (*Flpe*) expression leads to site-specific deletion of the *FRT*-flanked gene trap cassette used to inactivate the *Rnaseh2b* allele, leaving exon 5 of the *Rnaseh2b* gene flanked by *loxP* sites (*Rnaseh2b*^{FLOX}) that allow for cell type-specific or inducible Cre-mediated deletion of exon 5. Deletion of exon 5 causes complete inactivation of the *Rnaseh2b* gene (*Rnaseh2b*$^{\Delta\Delta}$) due to a frameshift mutation and premature transcriptional stop.

Since *Cre*-mediated deletion efficiency is dependent on the accessibility of the respective gene locus (Schmidt-Supprian and Rajewsky, 2007), we first tested the efficiency to delete the *Rnaseh2b* gene by breeding the *Rnaseh2b*^{FLOX} mouse line to the *PGK-Cre* mouse line that is characterized by ubiquitous Cre recombinase expression. We found the litter of this breeding to recapitulate the phenotype of *Rnaseh2c*$^{-/-}$ mice. *Rnaseh2b*$^{\Delta\Delta}$ mice were not detectable at weaning day and embryos died around day E10.5. This data demonstrated the functionality of the *lox*P-flanked *Rnaseh2b* allele, thus allowing for cell type-specific deletion of the *Rnaseh2b* gene.

Aiming to delete the *Rnaseh2b* gene in a cell type of the hematopoietic system we decided to generate a B cell-specific *Rnaseh2b* knockout and crossed the *Rnaseh2b*^{FLOX} mouse line with the *CD19-Cre* mouse line (Rickert et al., 1997) that is reported to efficiently delete *loxP*-flanked alleles in bone marrow-derived pre-B cells (75–80%) and in splenic B cells (90–95%) (Rickert et al., 1997). In contrast to the *Rnaseh2b KOF* mouse line, offspring of this breeding was viable and born at Mendelian ratios. B cell-specific knockouts of the *Rnaseh2b* gene did not display a macroscopic phenotype and numbers of B220^{+} CD19^{+} B cells in *CD19-Cre*$^{+}$ *Rnaseh2b*$^{FLOX/FLOX}$ mice (KO, 34.37 ± 13.17 x10^{7}, n = 6) were not altered when compared to B cell numbers from *CD19-Cre*$^{-}$

Rnaseh2b$^{FLOX/FLOX}$ or *CD19-Cre*$^{+}$ *Rnaseh2b*$^{WT/FLOX}$ mice (Ctrl, 37.39 ± 15.54 x10^{7}, n = 6) (Fig. 3.16).

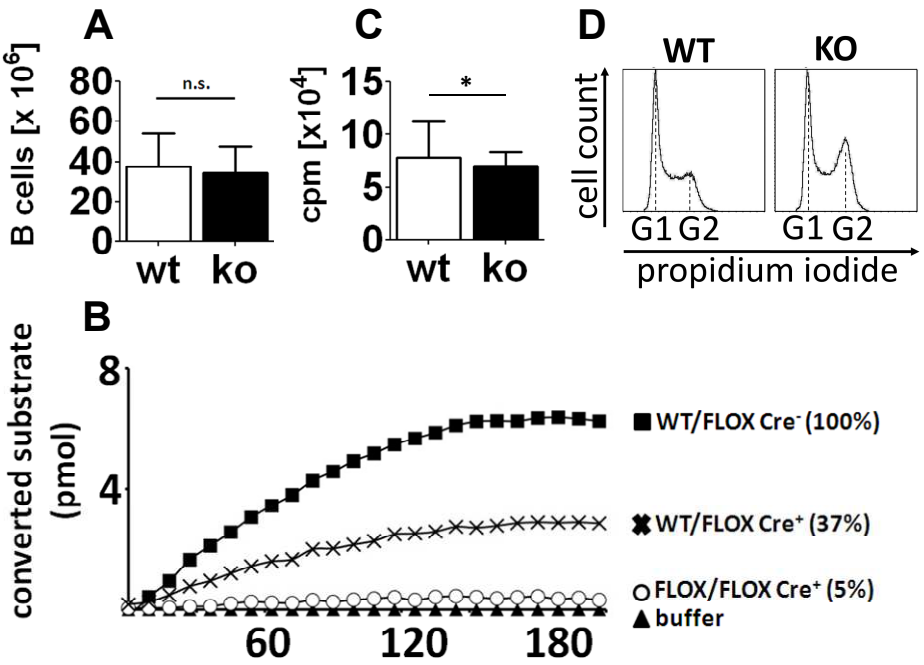

Figure 3.16: B cells of *CD19Cre*$^{+}$ *Rnaseh2b*$^{FLOX/FLOX}$ mice showed a mild proliferation defect when stimulated with LPS *in vitro*. (A) Absolute B cell numbers in B cell-specific *Rnaseh2b* knockout mice (KO, n=6) were unaltered when compared to B cell numbers of wild type mice (WT, n=6). **(B)** FACS-sorted B cells from *CD19Cre*$^{+}$ *Rnaseh2b*$^{FLOX/FLOX}$ mice (FLOX/FLOX Cre^{+}, n=2) showed reduced residual RNase H2 activity of 5% compared with RNase H2 activity of control mice (WT/FLOX Cre^{-}, n=2). B cells with a heterozygous mutation of the Rnaseh2b gene displayed 37% residual activity (WT/FLOX Cre+, n=2) **(C/D)** Upon *in vitro* LPS-stimulation, **(C)** B cells from *CD19Cre*$^{+}$ *Rnaseh2b*$^{FLOX/FLOX}$ mice (KO, n=9) showed a mild, but significant proliferation defect in comparison to control B cells (WT, n=9). **(D)** DNA content analysis revealed that an increased portion of RNase H2-deficient B cells (KO, n=6) accumulated in the G2/M phase of the cell cycle when compared to wild type (WT, n=6) control B cells.

To investigate the deletion efficiency upon *CD19Cre*-mediated deletion of exon 5, we tested the residual activity in FACS-sorted B cells from knockout and control cells. RNase H2 activity was found to be reduced to 5% of wild type activity in *CD19-Cre*$^{+}$ *Rnaseh2b*$^{FLOX/FLOX}$ B cells (Fig. 3.16). Considering the sorting purity between 96.5 and 97.7%, the residual activity of 5% was likely caused by contaminating cells, indicating complete RNase H2 deficiency in B cell-specific knockout mice. To investigate if the number of cell divisions might determine the phenotypic outcome, we stimulated B cells with the lipopolysaccharide (LPS) of gram-negative bacteria *in vitro*. LPS induces class switch recombination (Kracker and Radbruch, 2004) accompanied by massive B cell proliferation. ^{3}H thymidine incorporation assay of LPS-stimulated B cells displayed a slight, but significant difference between *CD19-Cre*$^{+}$ *Rnaseh2b*$^{FLOX/FLOX}$ B cells and

control B cells (Fig. 3.16) Knockout B cells showed impaired proliferation when compared to control B cells and DNA content analysis further demonstrated accumulation of B cells in G2/M of the cell cycle, similar to the data generated from E14.5 *Rnaseh2b*$^{KOF/KOF}$ MEFs (Fig. 3.16 and Fig. 3.10). Collectively, our data showed that RNase H2 deficiency in B cells does not cause a phenotype under steady-state conditions. *Rnaseh2b*-deficient B cells display a slight but significant proliferation defect upon *in vitro* LPS-stimulation, however, the defect was less severe compared to the massive proliferation defect detected in MEF cells from E14.5 and E18.5 *Rnaseh2b*$^{KOF/KOF}$ embryos. Still, this data supported our idea that the impact of RNase H2 deficiency is very much determined by the numbers of cell divisions.

Due to the moderate effect of RNase H2 deficiency in B cells we decided to delete the *Rnaseh2b* gene in a cell population outside the hematopoietic system aiming to induce a phenotype comparable to that of MEF cells from E14.5 and E18.5 *Rnaseh2b*$^{KOF/KOF}$ embryos. We thus generated an epidermis-specific knockout by crossing the *Rnaseh2b*^{FLOX} mouse to the *K14Cre* mouse line (Vasioukhin et al., 2001) in which Cre-expression is driven by the keratin 14 promoter and deleting at embryonic day E8.5. Keratin 14 is specifically expressed in cells of the epidermal basal membrane, thus resulting in deletion of the *Rnaseh2b* gene in the entire epidermis. Our first aim was to determine the deletion-efficiency of the *Rnaseh2b* gene and calculated *Rnaseh2b* transcript levels in the cells of epidermis from newborn *K14Cre*$^{+}$ *Rnaseh2b*$^{FLOX/FLOX}$ mice. We isolated total RNA from the entire epidermis of newborn pups and performed quantitative real-time PCR (qRT PCR). We detected a 7.88 ± 3.01 fold reduction of the *Rnaseh2b* transcript in the knockout epidermis (n = 4) when compared to littermate controls (n = 4)(Fig. 3.17). We additionally determined the residual activity of the RNase H2 enzyme in FACS-sorted keratinocytes from the epidermis of newborn pups to verify the above findings. We observed significant reduction of the RNase H2 activity in keratinocytes from *K14Cre*$^{+}$ *Rnaseh2b*$^{FLOX/FLOX}$ mice (n= 3) to 11% of transcript levels of littermate controls (n = 4, 100%)(Fig. 3.17).

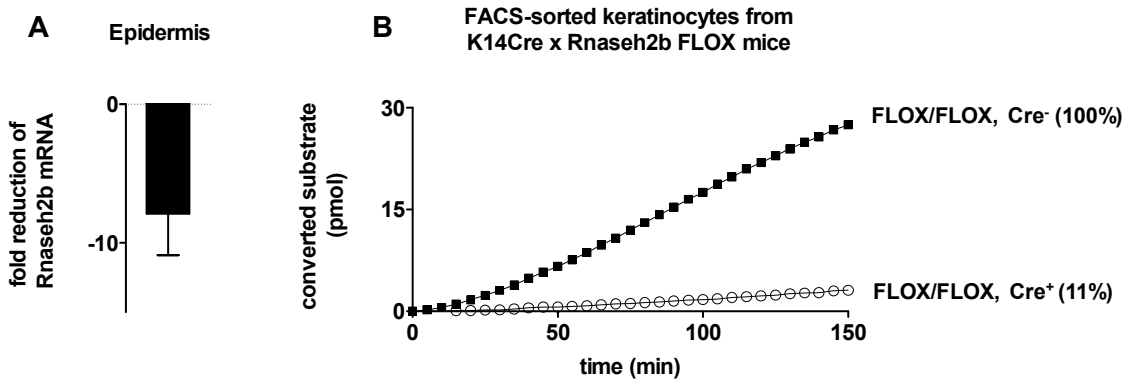

Figure 3.17: *K14Cre*$^{+}$ *Rnaseh2b*$^{FLOX/FLOX}$ mice display decreased RNase H2 activity in epidermal keratinocytes. FACS-sorted keratinocytes were analyzed for the expression of the *Rnaseh2b* transcript **(A)** and for the residual activity of the RNase H2 enzyme **(B)**. **(A)** *K14Cre*$^{+}$ *Rnaseh2b*$^{FLOX/FLOX}$ mice (n = 4) displayed an eightfold reduction in *Rnaseh2b* transcript levels when compared to control mice (n = 4). **(B)** Mean (without SD) RNase H2 enzyme activity of FACS-sorted keratinocytes from four control mice (FLOX/FLOX, Cre^{-}, n = 4, 100%) and the mean RNase H2 activity of FACS-sorted keratinocytes from *K14Cre*$^{+}$ *Rnaseh2b*$^{FLOX/FLOX}$ mice (FLOX/FLOX, Cre^{+}, n = 3, 11%) were plotted.

K14Cre^{+} *Rnaseh2b*$^{FLOX/FLOX}$ mice were born at Mendelian ratios, but within two weeks after birth, knockout pups were clearly distinguishable from their littermates due to hyperpigmented skin at the ears, paws and tail (3.18). Upon weaning, *K14Cre*$^{+}$ *Rnaseh2b*$^{FLOX/FLOX}$ mice displayed less bright fur and rudimental whiskers as well as signs of dermatitis that manifested as reddish and tight skin (3.18). Starting with about ten weeks of age, *K14Cre*$^{+}$ *Rnaseh2b*$^{FLOX/FLOX}$ mice gradually lost hair and were almost entirely hair less with 25 weeks of age (Fig. 3.21).

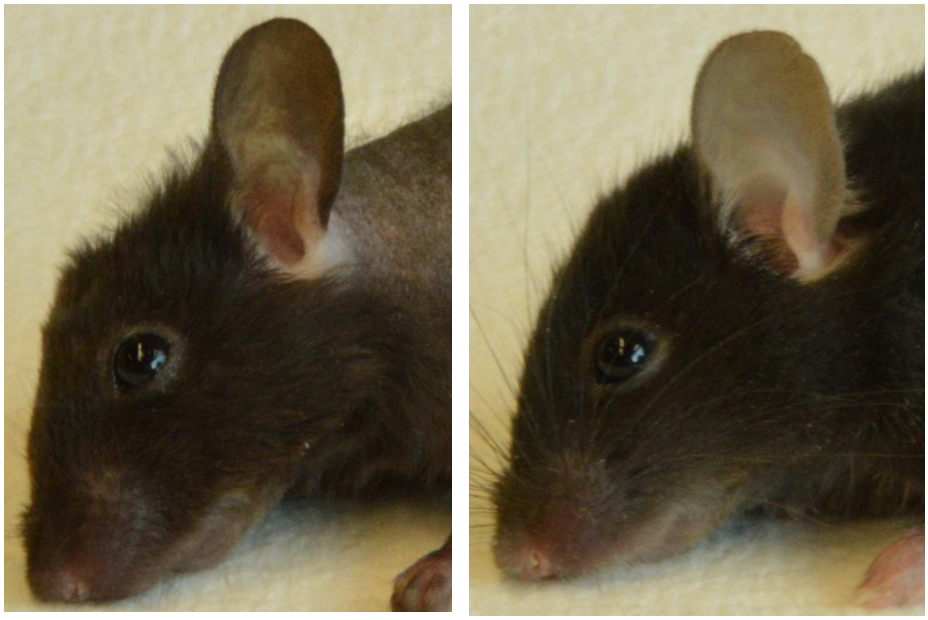

***K14Cre*$^{+}$ *Rnaseh2b*$^{FLOX/FLOX}$** **Control**

Figure 3.18: *K14Cre*$^{+}$ *Rnaseh2b*$^{FLOX/FLOX}$ mice display severe skin pathology. Mice deficient for the RNase H2 enzyme in the entire epidermis display a massive skin phenotype soon after birth. With the beginning of pigmentation, knockout mice reveal hyperpigmentation that becomes obvious at the ears, tails and paws. Moreover, the fur is less bright as in littermate controls and the whiskers are only present as rudiments.

To investigate the microscopic consequences of RNase H2 deficiency in the skin of *K14Cre*$^{+}$ *Rnaseh2b*$^{FLOX/FLOX}$ mice, we performed hematoxylin & eosin (H&E) staining of paraffin sections from dorsal skin biopsies of 9 week-old mice (Fig. 3.19). In comparison to the epidermis from wild type littermate controls, the epidermis of knockout mice was moderately thickened along the entire epidermis and the epidermal cell layers were less well organized as in control mice. Moreover, massive focal acanthosis could be observed in some areas of the RNase H2-deficient epidermis. To investigate whether increased epidermal thickness was a consequence of increased cell proliferation, we stained dorsal skin sections for the proliferation marker Ki67 that labels cycling cells (Scholzen and Gerdes, 2000). In control skin, proliferating cells were only detectable in the basal membrane of the epidermis. This was expected, since the only proliferating cell population of the epidermis, the epidermal stem cells, are located in the basal membrane (Fuchs, 2008). Ki67-staining of skin sections from *K14Cre*$^{+}$ *Rnaseh2b*$^{FLOX/FLOX}$ mice revealed an overall increase in cell proliferation in the entire epidermis. Moreover, Ki67-positive cells were also detectable in suprabasal layers of the epidermis (Fig. 3.19).

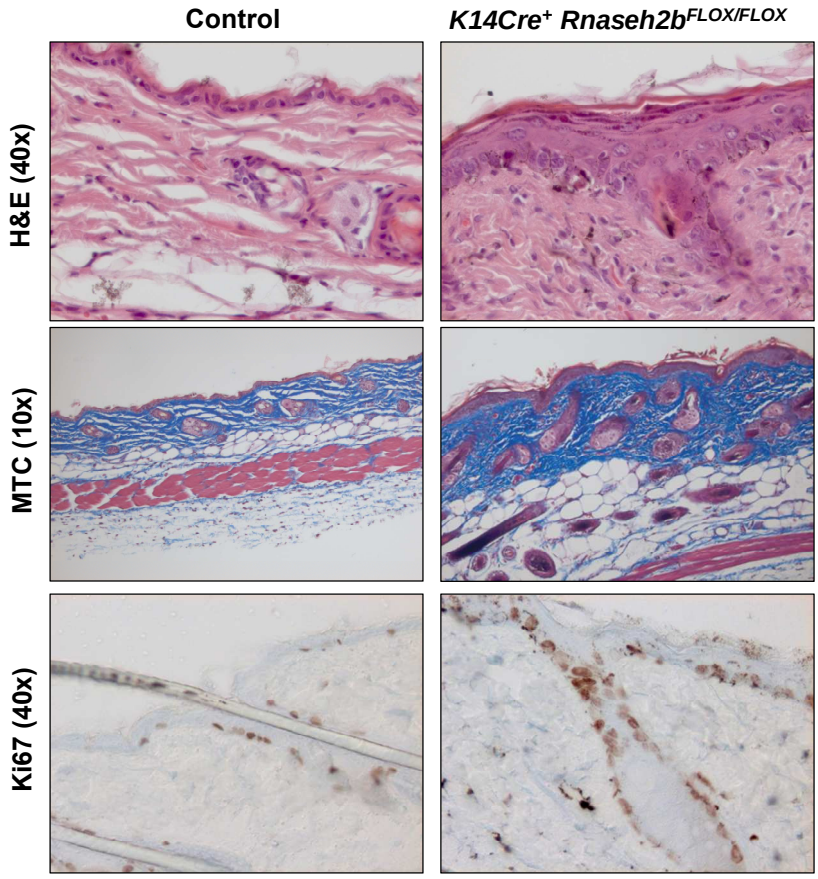

Figure 3.19: Hematoxylin and eosin (H&E), Masson`s trichrome and Ki67 staining of dorsal skin from 9 week old *K14Cre*$^{+}$ *Rnaseh2b*$^{FLOX/FLOX}$ and littermate control mice (Control). H&E staining of dorsal skin from 9 week-old *K14Cre*$^{+}$ *Rnaseh2b*$^{FLOX/FLOX}$ displayed moderate thickening of the epidermis interrupted by spots of focal acanthosis. Staining for the proliferation marker Ki67 demonstrated massive suprabasal cell proliferation in the epidermis that was absent in the dermis. The dermis completely lost basket work-like structure and showed increased infiltration of nucleated cells. Masson`s trichrome staining for collagen showed revealed increased collagen deposition in the knockout dermis.

The dermis of control skin sections showed basket work-like structure and only few nucleated cells were detectable. In contrast to control skin, skin sections from *K14Cre*$^{+}$ *Rnaseh2b*$^{FLOX/FLOX}$ mice did not display basket work-like organization. The dermis in knockout mice appeared massively thickened and tightly packed with a concomitant infiltration of nucleated cells (Fig. 3.19), reminiscent of the pathology of fibrotic diseases. Since dermal fibrosis is associated with increased collagen deposition, we performed Massson`s trichrome staining (MTC). We could detect increased collagen deposition in the dermis of *K14Cre*$^{+}$ *Rnaseh2b*$^{FLOX/FLOX}$ mice (Fig. 3.19) when compared to the dermis of control mice, indicating that the absence of the RNase H2 enzyme in the epidermis likely caused fibrosis in the underlying dermal tissue. We subsequently quantified total skin thickness by measuring the dorsal skin fold at various time points in order to determine the increase in skin thickness upon collagen deposition and observed increased skin thickness in *K14Cre*$^{+}$ *Rnaseh2b*$^{FLOX/FLOX}$ mice that significantly peaked

between week 10 and 20 (Fig. 3.20). Surprisingly, skin thickness decreased thereafter and *K14Cre*$^{+}$ *Rnaseh2b*$^{FLOX/FLOX}$ mice older than 30 weeks displayed skin thickness similar to that of control mice.

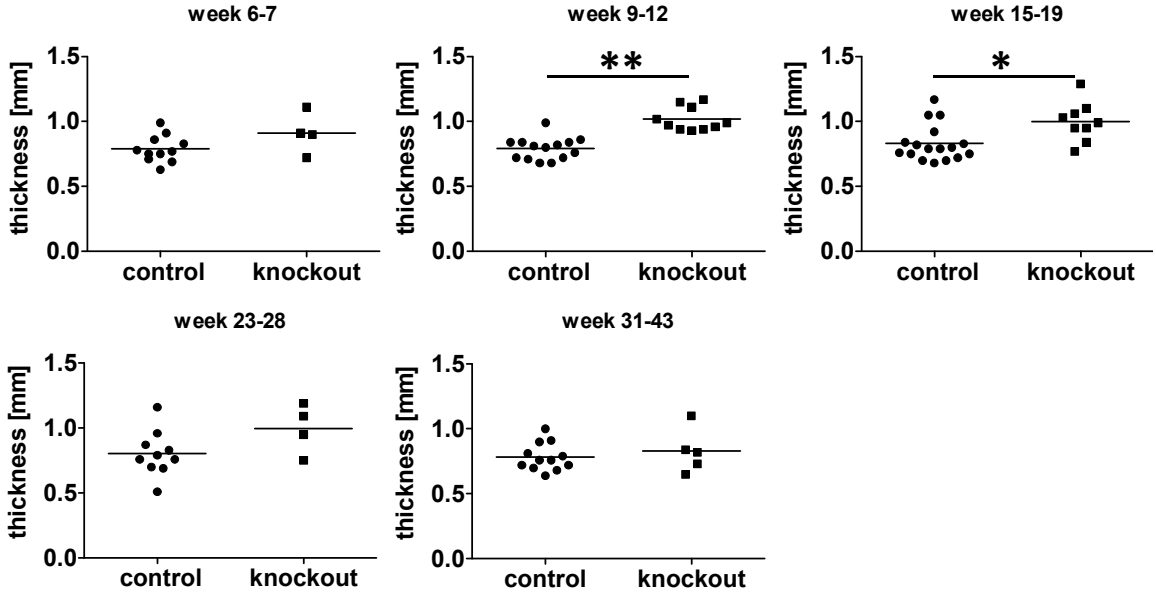

Figure 3.20: Maximum thickness of dorsal skin from *K14Cre*$^{+}$ *Rnaseh2b*$^{FLOX/FLOX}$ mice between 10 and 20 weeks of age. Dorsal thickness of *K14Cre*$^{+}$ *Rnaseh2b*$^{FLOX/FLOX}$ (knockout) and littermate controls (control) were determined at various time points, beginning at six weeks of age. Skin thickness gradually increased, peaked around week 12 and declined thereafter to control levels again.

K14Cre^{+} *Rnaseh2b*$^{FLOX/FLOX}$ mice gradually lost the entire fur and developed spontaneous ulcerations in the neck area of the dorsum beginning with the age of 20 weeks (Fig. 3.21). Ulcerations developed as a consequence of massive scratching and were thus limited to the neck area of the mouse. So far, we were not able to identify the reason for extensive scratching, but we hypothesize that RNase H2 deficiency might likely cause a barrier defect due to impaired function of RNase H2-deficient keratinocytes. This idea is supported by the fibrotic changes and the infiltration of nucleated cells into dermis that might also be a direct consequence of a barrier defect. We subsequently performed H&E staining of dorsal skin sections from 35 week-old mice that were taken from dorsal skin that did not display ulcerations. Surprisingly, we observed the amelioration of the microscopic skin alterations. The epidermal thickness was reduced in 35 week-old mice compared to epidermal thickness of younger mice, although skin thickness was still not comparable to control skin (Fig. 3.21). The dermis displayed basket work-like structure and the number of nucleated cells were comparable to that of wild type dermis. However, all adnexal structures of the skin were absent in the skin of *K14Cre*$^{+}$

Rnaseh2b$^{FLOX/FLOX}$ mice, indicating that hair loss was caused by the loss of the adnexal structures and not by impaired hair growth.

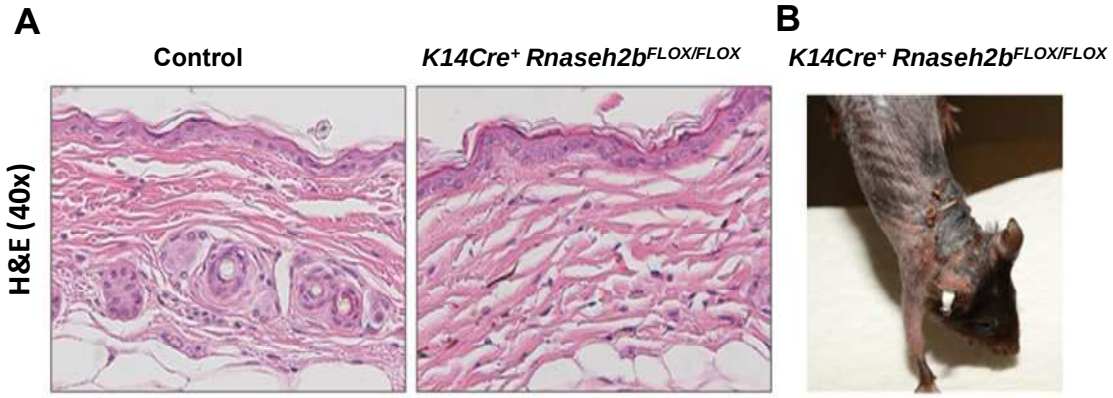

Figure 3.21: Amelioration of the dermal and epidermal pathology did not prevent spontaneous skin ulcerations. (A) Dorsal skin from 35 week-old *K14Cre*$^{+}$ *Rnaseh2b*$^{FLOX/FLOX}$ was undistinguishable from skin of age-matched littermate controls (Control). Epidermis and dermis were reduced in thickness and dermis showed basket work-like structure and normal numbers of nucleated cells. Adnexal structures were completely absent in the skin of knockout mice. **(B)** Although amelioration of the skin pathology was observed, *K14Cre*$^{+}$ *Rnaseh2b*$^{FLOX/FLOX}$ mice developed spontaneous ulcerations mostly in the neck area of the dorsum starting with the age of 20 weeks.

Since the loss of the adnexal structures of the skin represents the end point of a gradual process, we checked for the presence of epidermal stem cells in 12 week-old *K14Cre*$^{+}$ *Rnaseh2b*$^{FLOX/FLOX}$ mice. We stained epidermal stem cells according to Jensen et al. (Jensen et al., 2010) and detected a significant decrease of hair follicle stem cells, while no changes could be detected for interfollicular epidermal cells (Fig. 3.22). Detailed FACS analysis revealed a specific decrease of hair follicle stem cells and suprabasal hair follicle stem cells, while stem cells of the isthmus and the junctional zone were unaltered (data not shown). This data might indicate that the gradual loss of hair follicle stem cells might lead to the loss of the entire hair follicle.

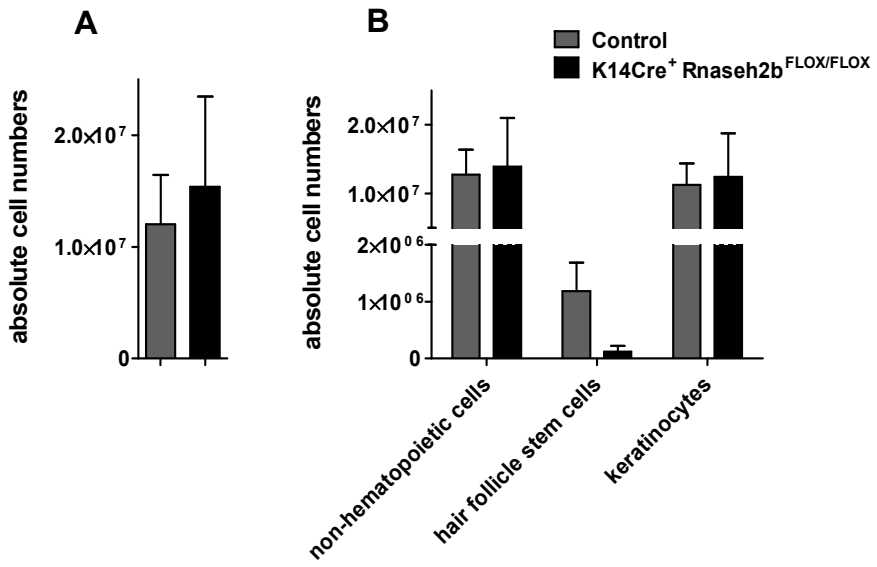

Figure 3.22: Massive reduction of hair follicle stem cells in the epidermis of *K14Cre*$^{+}$ *Rnaseh2b*$^{FLOX/FLOX}$ mice. (A) A mild increase of absolute epidermal cells numbers could be observed in *K14Cre*$^{+}$ *Rnaseh2b*$^{FLOX/FLOX}$ mice, likely attributing to epidermal hyperproliferation. **(B)** FACS analysis of epidermis cells revealed constant cell numbers of non-hematopoietic as wells as keratinocytes in wild type and knockout mice. In contrast, a drastic decrease in hair follicle stem cells could be observed in the epidermis from *K14Cre*$^{+}$ *Rnaseh2b*$^{FLOX/FLOX}$ mice.

In order to characterize the dermal infiltrate of nucleated cells from *K14Cre*$^{+}$ *Rnaseh2b*$^{FLOX/FLOX}$ mice, we collaborated with Prof. Jörg Wenzel from the university hospital in Bonn who stained dorsal skin sections for the leukocyte cell surface marker CD45. Staining for CD45 could confirm that the infiltrating nucleated cells were indeed CD45-positive leukocytes (Fig. 3.23). Moreover, detailed microscopic analysis of dorsal skin sections from 7 week-old *K14Cre*$^{+}$ *Rnaseh2b*$^{FLOX/FLOX}$ mice revealed skin pathology associated with a group of diseases, termed interface dermatitis that comprises the diseases lichen planus, dermatomyositis and the cutaneous lupus erythematosus (CLE) (Sontheimer, 2009a)(Fig. 3.23).

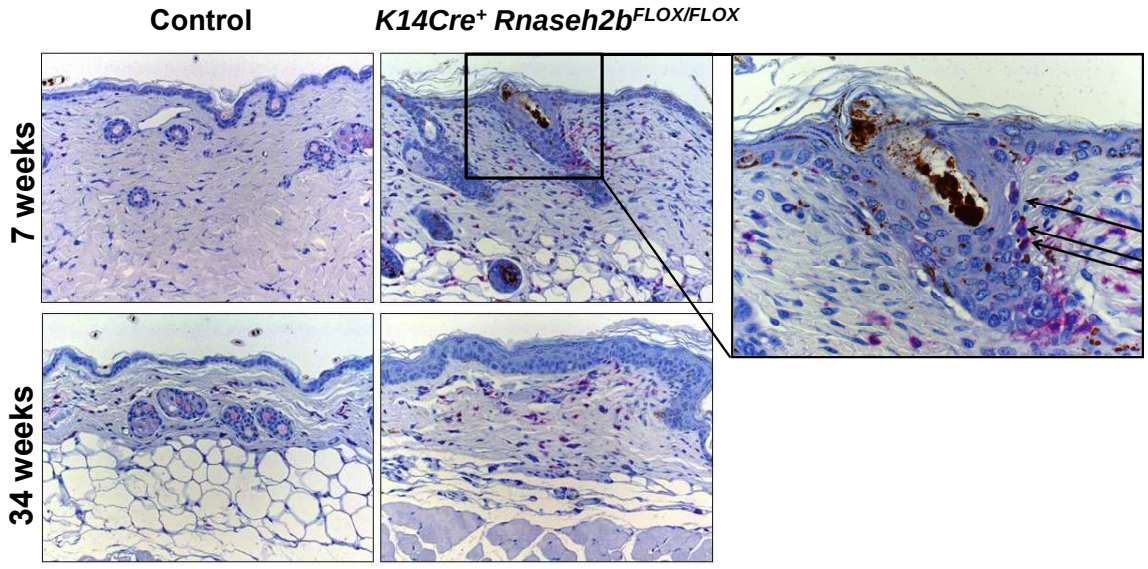

Figure 3.23: CD45-staining in *K14Cre*$^{+}$ *Rnaseh2b*$^{FLOX/FLOX}$ mice revealed poor leukocyte infiltration and interface dermatitis. Dorsal skin sections of 7 week and 34 week-old *K14Cre*$^{+}$ *Rnaseh2b*$^{FLOX/FLOX}$ mice and littermate controls (Control) were stained for the hematopoietic cell marker CD45. Skin from mice with an epidermis-specific knockout of the *Rnaseh2b* gene showed mild leukocyte infiltration at 7 weeks and 34 weeks. CD45-staining also revealed interface dermatitis at the bulge region of hair follicles. (black arrows label interaction of CD45^{+} cells with epidermal cells of the hair follicle)

Interface dermatitis manifests at the dermo-epidermal junction of the skin while inflammatory cells mediate pathology. Inflammatory cell-mediated vacuolization of basal cells and the induction of apoptosis in keratinocytes cause the obscuring of the dermo-epidermal junction, the characteristic feature of interface dermatitis. Figure 3.23 shows the infiltration of inflammatory cells into the dermo-epidermal junction and the resulting vacuolization that can be identified as white spots adjacent to the leukocyte infiltrate. As in human CLE patients, leukocyte infiltration in *K14Cre*$^{+}$ *Rnaseh2b*$^{FLOX/FLOX}$ mice is localized to the bulge region of the hair follicle. The observed interface dermatitis at the bulge region of the hair follicle and the associated destruction of the dermo-epidermal junction might likely explain the decrease in the numbers of hair follicle stem cells while numbers of other epidermal cells, like interfollicular epidermis cells, remained unaltered.

The pathology of interface dermatitis is characteristic but not specific for CLE. However, since CLE is caused by an unbalanced type I interferon response (Farkas et al., 2001), we subsequently analyzed skin from *K14Cre*$^{+}$ *Rnaseh2b*$^{FLOX/FLOX}$ mice for the presence of a type I interferon response. We performed FACS analysis of epidermal cells of eight to ten week old *K14Cre Rnaseh2b*^{FLOX} mice and stained for the cell surface marker Sca1 that is supposed to be up-regulated upon type I interferon encounter (Hartner et al., 2009). We could detect considerable upregulation of Sca1 expression on CD45-positive cells of the epidermis from *K14Cre*$^{+}$ *Rnaseh2b*$^{FLOX/FLOX}$ mice, implicating that pathology in

K14Cre^{+} *Rnaseh2b*$^{FLOX/FLOX}$ mice could be mediated by the expression of type I interferon. To test this hypothesis we next performed gene expression analysis of total skin from eight week-old *K14Cre Rnaseh2b*^{FLOX} mice using quantitative real time PCR (qRT PCR). Pairwise comparison of RNA from three to four knockouts versus littermate controls showed a five-fold downregulation of the *Rnaseh2b* gene, showing the reliability of the method. Further expression analysis of type I interferon-inducible genes (ISGs) *Isg15*, *Oas1a*, *Rsad2* and *Ifi44* revealed upregulation of all four ISGs. However, while *Isg15* and *Oas1a* revealed a mean upregulation by 4 fold, *Rsad2* and *Ifi44* showed a mean upregulation by 1.5 fold (Fig. 3.24). Considering that most fold changes were substantially decreased by a single outlier (blue symbol) and that epidermal transcript levels were diluted by the transcripts of dermal cells, we hypothesized that skin pathology *K14Cre*$^{+}$ *Rnaseh2b*$^{FLOX/FLOX}$ mice was at least partly mediated by type I interferon.

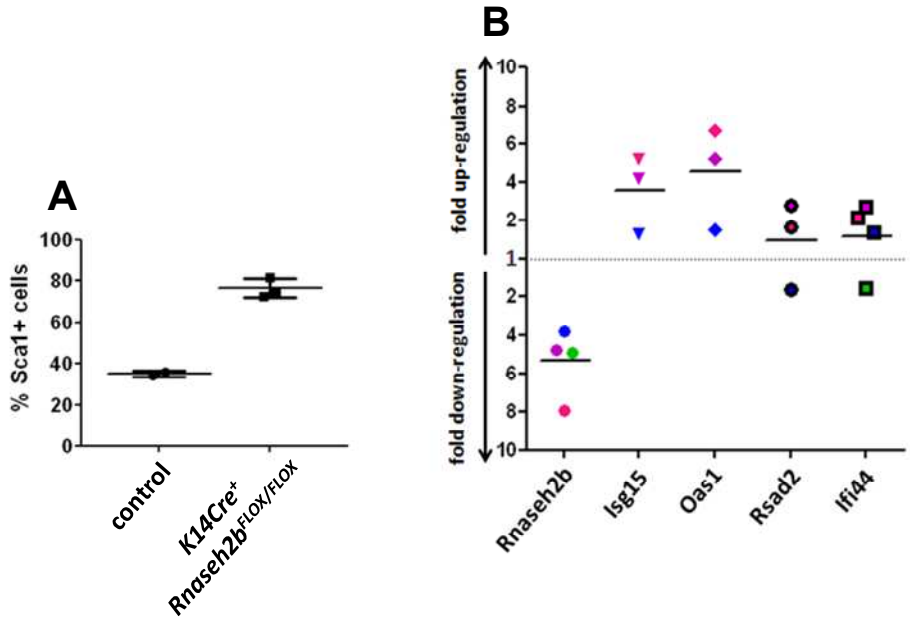

Figure 3.24: Type I Interferon signature in epidermal CD45^{+} cells and in skin of *K14Cre*$^{+}$ *Rnaseh2b*$^{FLOX/FLOX}$ mice. (A) FACS analysis of CD45+ epidermal cells revealed increased expression of the type I interferon-induced Sca1 marker in eight week old *K14Cre*$^{+}$ *Rnaseh2b*$^{FLOX/FLOX}$ mice (n=3) when compared to littermate controls (control, n=2). **(B)** Quantitative real time PCR (qRT PCR) of RNA from total skin of *K14Cre*$^{+}$ *Rnaseh2b*$^{FLOX/FLOX}$ mice revealed the upregulation of the type I interferon-inducible genes Isg15, Oas1a, Rsad2 and Ifi44 by at least 1.5 fold. At the same time, transcripts of the *Rnaseh2b* gene were fivefold down-regulated, confirming the reliability of the qRT PCR data. Fold change was determined by pairwise comparison of qRT PCR data from *K14Cre*$^{+}$ *Rnaseh2b*$^{FLOX/FLOX}$ mice and control mice (n=3-4). Each color represents data of a single individual.

To confirm our hypothesis that pathology in *K14Cre*$^{+}$ *Rnaseh2b*$^{FLOX/FLOX}$ mice was at least partially mediated by increased type I interferon expression, we performed a microarray-based gene expression analysis of RNA from total skin of 7 week-old *K14Cre*

Rnaseh2b$^{FLOX/FLOX}$ mice. Pair-wise comparison of four knockouts versus four wild type littermate controls revealed significant deregulation of 331 genes (fold change ≥ 1.5, p = 0.05). 31 genes were found to be down-regulated, whereas 286 genes were up-regulated (Table 6.1).

In contrast to our previous data, microarray-based gene expression analysis of RNA from total skin of 8 week-old *K14Cre*$^{+}$ *Rnaseh2b*$^{FLOX/FLOX}$ mice did not display increased expression of type I interferon-inducible genes (ISGs). The interferon-inducible genes *Isg15* (1.7), *Oas1a* (1.43), *Rsad2* (1.0), *Ifi44* (1.0) were not as deregulated as in the previous qRT PCR analysis (Fig. 3.24). However, since the *Rnaseh2b* gene displayed a 2.7 fold down-regulation (compared to the more than fivefold downregulation measured by qRT PCR), we think that the differences between both methods may be a result of the quenching effects that are described for microarray analysis (Ramdas et al., 2001).

However, since gene expression analysis of total skin did not reveal a type I interferon response in *K14Cre*$^{+}$ *Rnaseh2b*$^{FLOX/FLOX}$ mice, we subsequently performed a cluster analysis using the Ingenuity Pathway Analyzer (Krämer et al., 2014) and identified the cluster “Cell cycle: G2/M DNA damage checkpoint regulation” to contain the greatest set of de-regulated genes in our array (Table 6.2). The cluster comprised genes like *Chek1*, *Chek2* and *Brca1*. These genes encode for well-known members of the DNA damage repair pathway that is activated upon DNA double-strand or single strand breaks. Additionally, the p53-signalling cluster was also shown to contain de-regulated genes of our array. Hence, the gene expression profile of total skin from *K14Cre Rnaseh2b*^{FLOX} mice was very similar to the gene expression profile of E14.5 fetal liver cells from *Rnash2b*$^{KOF/KOF}$ embryos, since both arrays predominantly display a DNA damage-mediated p53 response. In line with the phenotypic observations made in the *K14Cre*$^{+}$ *Rnaseh2b*$^{FLOX/FLOX}$ mice, the “Eumelanin Biosynthesis” cluster could also be detected among the top gene clusters. The upregulation of this cluster very well correlated with the hyperpigmentation on the skin of ears, paws and tail of *K14Cre*$^{+}$ *Rnaseh2b*$^{FLOX/FLOX}$ mice.

Due to the finding that RNase H2 deficiency leads to the activation of a p53-mediated DNA damage response and based on data from several studies that describe the tumor suppressor p53 as an important mediator for pathologies associated with hair loss and hyperpigmentation (Sotiropoulou et al., 2013; Cui et al., 2007), we crossed the *K14Cre*$^{+}$ *Rnaseh2b*$^{FLOX/FLOX}$ mouse on a p53-deficient background aiming to rescue the skin pathology. Preliminary data confirmed our hypothesis and *K14Cre*$^{+}$ *Rnaseh2b*$^{FLOX/FLOX}$ mice with a heterozygous deletion of the p53 gene already showed amelioration of the skin phenotype. These mice showed intermediate pigmentation and did not lose hair at least until the age of 30 weeks. Moreover, these mice did not develop spontaneous

ulcerations compared with age-matched *K14Cre*$^{+}$ *Rnaseh2b*$^{FLOX/FLOX}$ mice. *K14Cre*$^{+}$ *Rnaseh2b*$^{FLOX/FLOX}$ *p53*$^{ko/ko}$ mice showed complete reversion of the skin phenotype and were very similar to RNase H2-proficient littermate controls. In slight contrast to the littermate controls, double knockout mice displayed scrubby fur. However, with about 10 to 12 weeks of age mice started to lose hair in the dorsal neck region due to extensive scratching, while hair loss could not be observed at any other region of the mouse body. Subsequent histological analysis of the *K14Cre*$^{+}$ *Rnaseh2b*$^{FLOX/FLOX}$ *p53*$^{-/-}$ mouse line will provide detailed information about the underlying mechanism that cause the macroscopic phenotype. Anyway, preliminary data from *K14Cre*$^{+}$ *Rnaseh2b*$^{FLOX/FLOX}$ *p53*$^{wt/ko}$ and *K14Cre*$^{+}$ *Rnaseh2b*$^{FLOX/FLOX}$ *p53*$^{ko/ko}$ might also indicate that RNase H2 deficiency might cause the formation of cancer. Both mouse lines demonstrated hyperplastic tissue that could be found in mice that were RNase H2-proficient, but p53-deficient. Further studies of *K14Cre*$^{+}$ *Rnaseh2b*$^{FLOX/FLOX}$ *p53*$^{-/-}$ mice will show whether we can provide evidence that RNase H2 deficiency increases the susceptibility for cancer formation, as it was already predicted in earlier studies (Crow et al., 2006b).

3.4 Generation and analysis of bone marrow chimera

In parallel to the generation of cell type-specific knockout mice, we also generated bone marrow chimera. For the generation of chimera, mice are irradiated with a lethal dosage of gamma irradiation that causes the destruction of the radio-sensitive hematopoietic system, including the hematopoietic stem cells. Lethality of irradiated mice is subsequently rescued by reconstitution with either bone marrow cells of adult mice or with embryonic liver cells, since embryonic hematopoiesis takes place in the fetal liver (Golub and Cumano, 2013). To allow the discrimination between residual cells of the irradiated recipient and transplanted cells of the donor, cells of syngenic mouse strains are transferred that express variants of the hematopoietic cell surface protein CD45. Whereas hematopoietic cells from C57BL/6 mice express the CD45.2 variant, hematopoietic cells from SJL mice express CD45.1. The F1 generation of C57BL/6 and SJL mice expresses both variants at an equal ratio (CD45.1/2) (Figure 3.25). In order to determine the donor cell contribution, the chimerism is regularly (every four weeks) determined in peripheral blood polymorphonuclear cells (PMNs), B cells and T cells using flow cytometry. PMNs are characterized by a short life time of only about 14 days and need to be replenished by hematopoietic stem and progenitor cells to maintain the PMN pool. Thus peripheral blood chimerism is used as a marker for bone marrow chimerism. While various progenitor cells, multipotent progenitors and short-term hematopoietic stem cells can deliver short-term reconstitution, long term reconstitution

for longer than 16 weeks can only be achieved by the activity of long-term hematopoietic stem cells (Morrison and Weissman, 1994; Purton and Scadden, 2007).

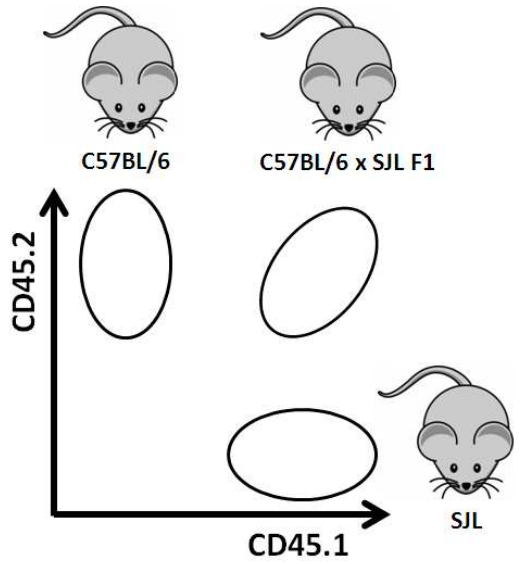

Figure 3.25: Discrimination between donor and recipient hematopoietic cells by the cell surface marker CD45. The surface marker CD45 is expressed on all hematopoietic cells and allows for the discrimination between cells from syngenic mouse lines. Cells of common C57BL/6 mice express CD45.2, whereas syngenic SJL mice express CD45.1. The F1 litter of C57BL/6 and SJL mice expresses CD45.2 and CD45.1.

3.4.1 Non-competitive transfer of E14.5 fetal liver cells

To investigate the role of RNase H2-deficient hematopoietic cells in the pathology of *Rnaseh2b*$^{KOF/KOF}$ mice, we generated bone marrow chimera by transplanting E14.5 fetal liver cells of *Rnaseh2b*$^{WT/WT}$ and *Rnaseh2b*$^{KOF/KOF}$ embryos into irradiated recipient SJL mice. In a first experiment, 2.5×10^5 (1,25 x radio protection dosage, (Morrison et al., 1995)) viable fetal liver cells of E14.5 *Rnaseh2b*$^{WT/WT}$ and *Rnaseh2b*$^{KOF/KOF}$ embryos were transferred into five and six irradiated (7Gy) recipient SJL mice, respectively. Within the first two weeks after transfer, both irradiation controls (irradiated, but not reconstituted with fetal liver cells) and mice that were either reconstituted with wild type (1) or knockout (4) fetal liver cells died. Analysis of the remaining recipient mice four weeks after the transfer showed high-level chimerism of about 98% in mice that were reconstituted with *Rnaseh2b*$^{WT/WT}$ fetal liver cells. However, recipient mice that were reconstituted with *Rnaseh2b*$^{KOF/KOF}$ fetal liver cells showed low-level chimerism of 24% and 0.37%, respectively (data not shown). We suggested that low-level chimerism was either a consequence of technical problems during the retro-orbital cell transfer of fetal liver cells, reduced overall stem cell numbers in the fetal liver of *Rnaseh2b*$^{KOF/KOF}$

embryos or impaired stem cell function. To investigate if the low-level chimerism was caused by reduced stem cell numbers or impaired stem cell function in RNase H2-deficient embryos, we performed a second experiment with a 20 fold radioprotection dosage and transferred 4×10^6 fetal liver cells of E14.5 *Rnaseh2b*$^{WT/WT}$ and *Rnaseh2b*$^{KOF/KOF}$ embryos into lethally irradiated (7Gy) F1 recipients (Fig. 3.26).

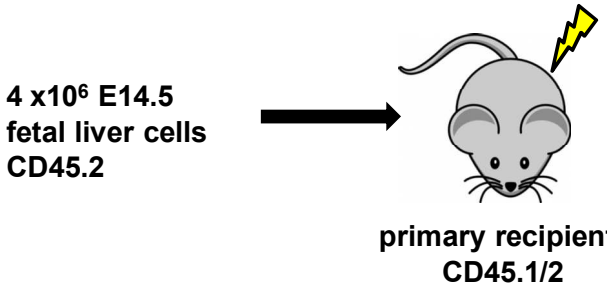

donor cells	survival
Rnaseh2b$^{WT/WT}$	3/3
Rnaseh2b$^{KOF/KOF}$	3/3

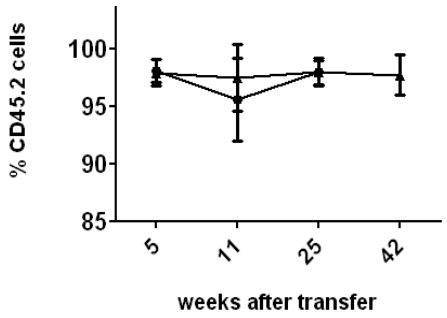

Figure 3.26: 4x10^6 E14.5 fetal liver cells of *Rnaseh2b*$^{KOF/KOF}$ embryos could successfully reconstitute primary recipients for at least 42 weeks. 4x10^6 fetal liver cells of E14.5 *Rnaseh2b*$^{WT/WT}$ (n=3, black circles) and *Rnaseh2b*$^{KOF/KOF}$ (n=3, black triangles) embryos were transplanted into lethally irradiated (7Gy) recipients. Stable high-level donor cell chimerism (%CD45.2 cells) in polymorphonucleated (PMNs) cells showed that fetal liver cells of wild type and RNase H2-deficient embryos were capable of reconstituting recipients for at least 42 weeks.

Four weeks after transplantation, all recipient mice were viable and displayed high-level chimerism. Mice reconstituted with knockout fetal liver cells showed a chimerism of 97.9 ± 1.1% in the PMN cell population, while mice that were reconstituted with wild type fetal liver cells displayed a chimerism of 97.5 ± 1.0%. High-level chimerism remained stable in mice reconstituted with RNase H2-deficient fetal liver cells, even after 25 (97.9 ± 1.2%) and 44 weeks (97.7 ± 1.3%). Since long-term reconstitution (≥ 16 weeks, (Morrison and Weissman, 1994; Purton and Scadden, 2007)) is completely dependent on the activity and proper function of LT-HSCs, this data likely indicated that the failure of RNase H2-deficient fetal liver cells to reconstitute irradiated mice in the first experiment was likely caused by the technical problems or reduced stem cell numbers and not by non-functional stem cells. However, transplantation of high cell numbers of knockout fetal liver cells might have compensated for reduced cell numbers. To address this question, we subsequently determined hematopoietic stem cell numbers in E14.5 fetal livers from *Rnaseh2b*$^{WT/WT}$, *Rnaseh2b*$^{WT/KOF}$ and *Rnaseh2b*$^{KOF/KOF}$ embryos.

Hematopoietic stem cells are defined by the absence of lineage-determining markers (lineage$^-$, lin$^-$) and the concomitant expression of the stem cell growth factor receptor (c-Kit, CD117) and the stem cell antigen 1 (Sca1). The Kit$^+$, Sca1$^+$ and lineage$^-$ (KSL) cell population comprises diverse stem cell populations that differ in respect to their self-renewal capacity and the spectrum of progenitor cells they can give rise to. Using the signaling lymphocyte activation markers (SLAM) CD48 and CD150, KSL cells can be subdivided into multipotent progenitors (MPPs, CD48$^+$ CD150$^-$), short-term hematopoietic stem cells (ST-HSCs, CD48$^+$ CD150$^+$) and long-term hematopoietic stem cells (LT-HSCs, CD48$^-$ CD150$^+$). LT-HSCs possess the highest self-renewal capacity and the potential to give rise to any cell type of the hematopoietic system, whereas MPPs have no self-renewal capacity with only limited potential. ST-HSCs display an intermediate phenotype with limited self-renewal capacity (Morrison and Weissman, 1994; Wilson et al., 2007) (Fig. 3.27).

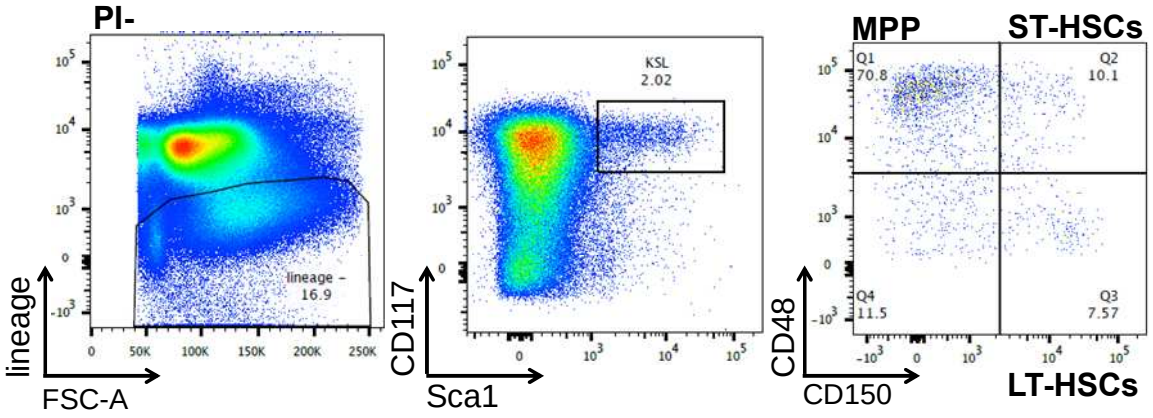

Figure 3.27: Gating strategy for the definition of hematopoietic stem cells by flow cytometry. KSL cells were defined as propidium iodide (PI)-negative and lineage-negative cells that concomitantly expressed the cell surface markers CD117 and Sca1. KSL cells could be further subdivided into MPPs, ST-HSCs and LT-HSCs using the SLAM markers CD48 and CD150, with LT-HSCs having the highest self-renewal capacity and the potency to give rise to any cell of the hematopoietic system.

According to the small size of the fetal liver from E14.5 *Rnaseh2b*$^{KOF/KOF}$ embryos, absolute cell numbers of RNase H2-deficient fetal liver cells were also dramatically reduced (4.88 ± 0.72 x10^6, n = 8) when compared to fetal liver cells of wild type (14.62 ± 3.57 x10^6, n = 12) and heterozygous embryos (16.84 ± 3.92 x10^6, n = 7) (Fig.3.28). KSL SLAM staining of E14.5 fetal liver cells displayed only moderate changes in relative terms (data not shown). However, due to the massive reduction in total cell numbers, all hematopoietic cell populations in *Rnaseh2b*$^{KOF/KOF}$ embryos were massively reduced in absolute numbers. While the lineage-negative (lin$^-$) population displayed the mildest reduction of about 20 fold, LT-HSCs showed the strongest reduction of more than 75

fold. LT-HSC numbers in fetal livers of *Rnaseh2b*$^{KOF/KOF}$ embryos were reduced to 0.032 ± 0.019 x 10^4 cells (n=8), compared to 2.134 ± 0,996 x 10^4 wild type cells (n=12) and 2.822 ± 1.127 x 10^4 fetal liver LT-HSCs from *Rnaseh2b*$^{WT/KOF}$ embryos (n=7). However, as a consequence of reduced stem cell numbers in the fetal liver of RNase H2-deficient embryos, LT-HSC frequencies were also twofold reduced (1 LT-HSC / 1525 cells, 0.065%), compared to frequencies from wild type (1 LT-HSC / 686 cells, ~0.15%) and heterozygous embryos (1 LT-HSC / 597 cells, ~0.17%). Considering the calculated mean LT-HSC frequency of 0.065% in the fetal liver of E14.5 *Rnaseh2b*$^{KOF/KOF}$ embryos, we transferred approximately 150 LT-HSCs into lethally irradiated recipients during the first transfer experiment, a number that is reported to be sufficient to generate stable chimerism (Morrison et al., 1995). Together with the observation that RNase H2-defcient fetal liver cells can reconstitute irradiated recipients as long as enough donor cells are transplanted, we conclude that the low-level chimerism in the first experiment was caused by technical problems during the retro-orbital injection. Therefore, we transferred cell numbers smaller 4 x 10^6 in the following experiments.

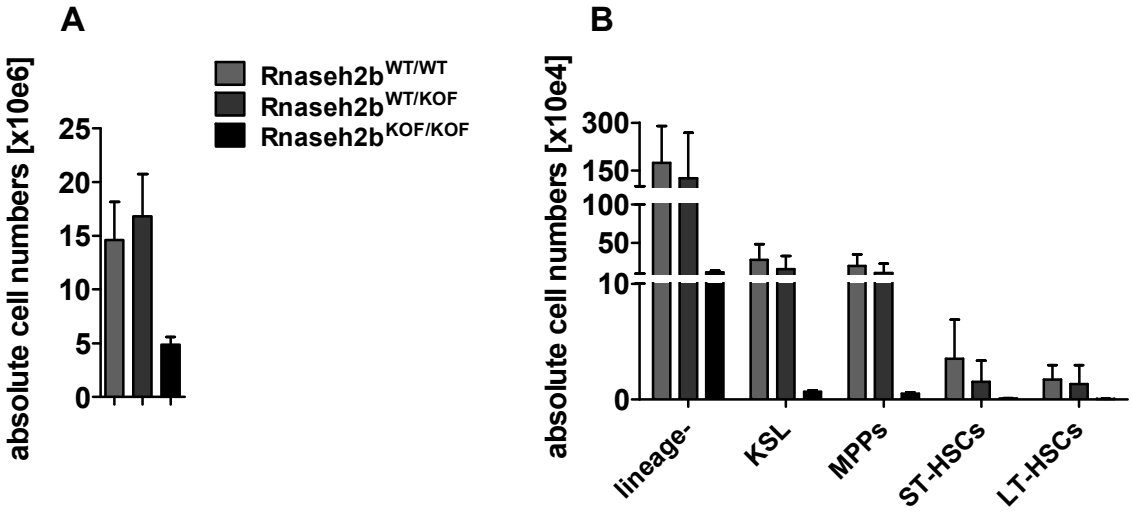

Figure 3.28: Reduced absolute cell numbers in E14.5 *Rnaseh2b*$^{KOF/KOF}$ mice. (A) Absolute cell numbers were found to be fourfold reduced in E14.5 fetal liver cells of *Rnaseh2b*$^{KOF/KOF}$ (black bars, n=8) embryos when compared to *Rnaseh2b*$^{WT/WT}$ (light grey bars, n=12) and *Rnaseh2b*$^{WT/KOF}$ (dark grey bars, n=7) embryos. **(B)** Although relative numbers of most cell compartments in *Rnaseh2b*$^{KOF/KOF}$ embryos were only mildly altered, decreased absolute cell numbers in *Rnaseh2b*$^{KOF/KOF}$ fetal liver caused reduced overall cell numbers in various bone marrow cell compartments. Calculating the ratio of one LT-HSC per total cells also revealed a twofold reduction in the frequency of LT-HSC cells.

3.5.1 Secondary transfer of Rnaseh2b KOF bone marrow cells

Since bone marrow chimera did not display a macroscopic phenotype after reconstitution with RNase H2-deficient fetal liver cells, we wondered if these cells were also competent to reconstitute secondary recipients in a serial transfer experiment. To this end, bone marrow cells of primary recipients were transplanted into lethally irradiated secondary recipients. The secondary transfer represents massive stress for the cells of the hematopoietic system, in particular, hematopoietic stem cells, since the reconstitution of a secondary recipient requires massive proliferation of these cells. In case RNase H2 deficiency causes a defect that is determined by the number of cell divisions, we hypothesized that RNase H2-deficient fetal liver cells fail to repeatedly reconstitute recipient mice. To test this hypothesis, we first generated primary recipients by reconstituting irradiated (7Gy) F1 hybrid mice with 1×10^6 E14.5 *Rnaseh2b*$^{KOF/KOF}$ fetal liver cells and 0.5×10^6 E14.5 *Rnaseh2b*$^{WT/WT}$ and *Rnaseh2b*$^{WT/KOF}$ fetal liver cells, respectively. We used twice as much fetal liver cells from RNase H2-deficient mice in order to compensate for the decreased stem cell frequency in fetal livers from *Rnaseh2b*$^{KOF/KOF}$ embryos. Although we transplanted fourfold less cell numbers when compared with the previous transfer experiment, almost all recipient mice survived (Fig. 3.29). Moreover, all recipients demonstrated stable high-level chimerism in the PMN-, B cell- and T cell compartment during 36 weeks (Fig. 3.29), independent of the genotype of the donor fetal liver cells. This data showed that the five-fold radioprotection dosage or transfer of 1×10^6 RNase H2-deficent fetal liver cells were sufficient to long-term reconstitute irradiated recipients.

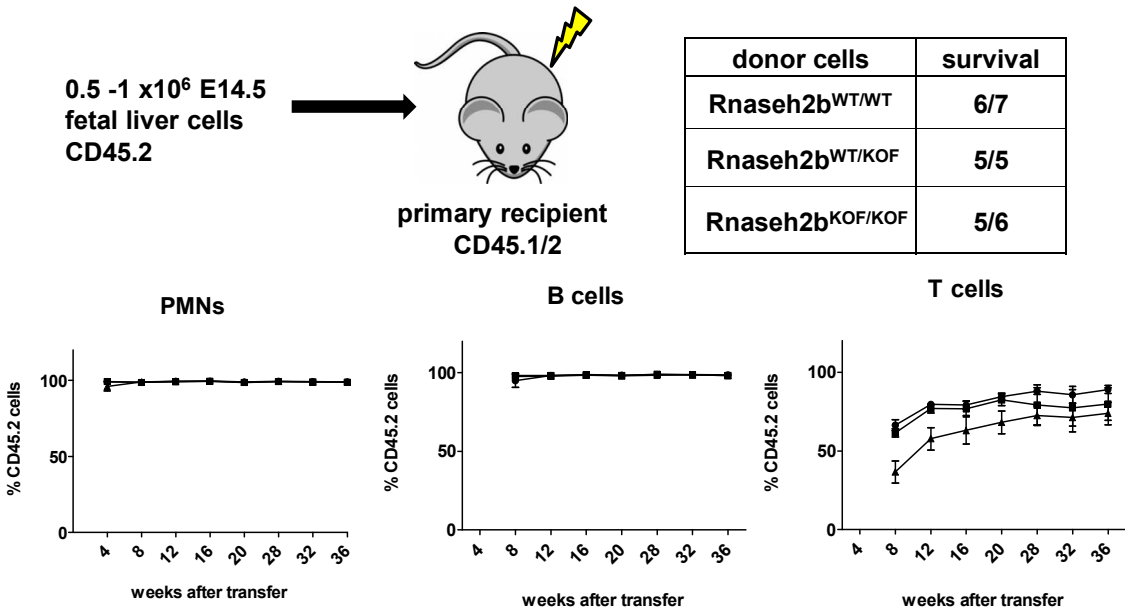

donor cells	survival
Rnaseh2b$^{WT/WT}$	6/7
Rnaseh2b$^{WT/KOF}$	5/5
Rnaseh2b$^{KOF/KOF}$	5/6

Figure 3.29: 1x10^6 E14.5 fetal liver cells of *Rnaseh2b*$^{KOF/KOF}$ embryos stably reconstituted lethally irradiated recipient mice. Irradiated (7Gy) F1 recipients were either reconstituted with 0.5 x 10^6 fetal liver cells from *Rnaseh2b*$^{WT/WT}$ (black circles) and *Rnaseh2b*$^{WT/KOF}$ (black boxes) embryos or with 1 x 10^6 fetal liver cells from *Rnaseh2b*$^{KOF/KOF}$ (black triangles) embryos to compensate for twofold less LT-HSC frequency in RNase H2-deficient fetal liver cells. Stable chimerism was detected in the PMN-, B cell- and T cell compartment for 36 weeks.

In preparation of the secondary transfer of bone marrow cells, we determined absolute bone marrow cell numbers of primary recipients and determined the chimerism of various bone marrow cell populations by FACS analysis (Fig. 3.30). We could not detect any difference in absolute bone marrow cell numbers between mice that were either reconstituted with wild type, heterozygous or knockout fetal liver cells. Differences could also not be observed in absolute numbers of MPPs, ST-HSCs and LT-HSCs and also the chimerism in all these cell populations was close to 100% (98.7 – 99.7%). The even absolute cell numbers and the high-level chimerism in the bone marrow of primary recipients allowed us to use these cells in a subsequent secondary transfer experiment.

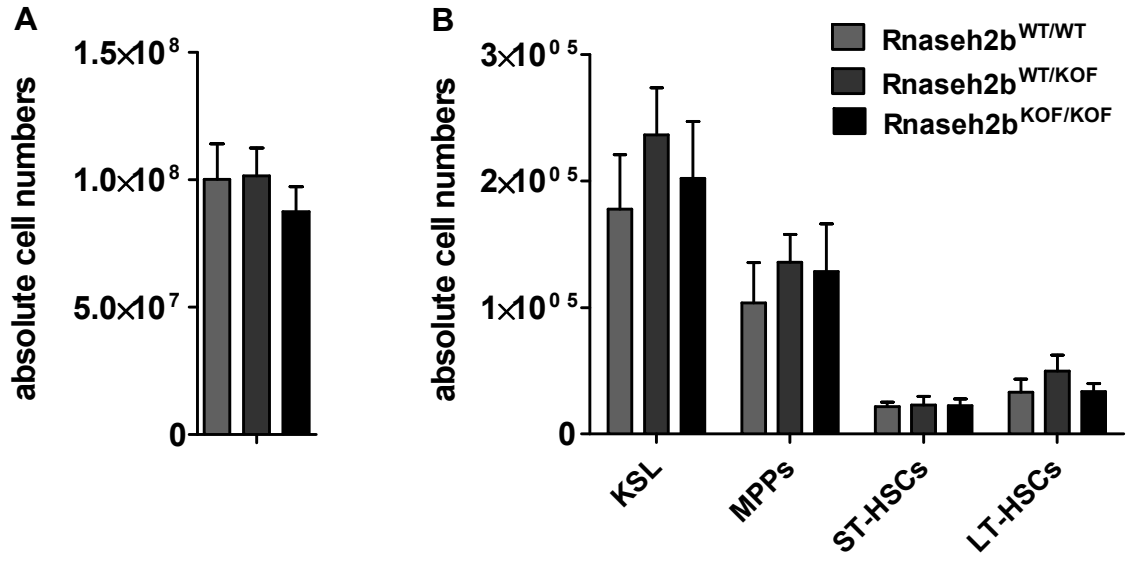

Figure 3.30: Similar absolute numbers of bone marrow cells in primary recipients. (A) Absolute bone marrow cell numbers of primary recipients were determined and no differences could be observed between recipients that were either reconstituted with wild type (light grey bars, n=6), heterozygous (dark grey bars, n=3) or knockout (dark bars, n=3) E14.5 fetal liver cells. **(B)** Staining for various bone marrow stem cells did not show different absolute cell numbers for KSL cells, MPPs, ST-HSCs and LT-HSCs.

In order to eliminate contaminating cells of the primary recipient (CD45.1/2), we subsequently FACS-sorted CD45.2$^+$ CD117$^+$ bone marrow cells of primary recipients and finally transplanted 5 x 10^4 CD45.2+ CD117+ cells into lethally irradiated (8Gy) recipient SJL mice. Progenitor cell populations within the CD117+ cell compartment delivered short-term radioprotection. Two recipient mice died within the first two weeks, while most recipient mice survived until the end of the experiment (Fig. 3.31). Four weeks after the transfer, chimerism was determined by FACS analysis. High-level chimerism could be observed in peripheral blood PMNs and B cells. The slightly reduced chimerism of peripheral blood PMNs of mice reconstituted with RNase H2-deficient bone marrow (84.7 ± 30.4%) was likely caused by low-level chimerism of a single recipient (30%). However, eight weeks after the transfer, the chimerism of peripheral blood PMNs and B cells of recipients that received *Rnaseh2b*$^{KOF/KOF}$ bone marrow displayed a gradual decline of the chimerism to 17.55 ± 19.44% and 31.64 ± 22.17%, respectively, after 32 weeks. In contrast to the chimerism of recipients that were reconstituted with knockout bone marrow, the chimerism of recipients that were reconstituted with wild type or heterozygous bone marrow showed stable, high-level chimerism for 32 weeks. The T cell chimerism of all recipients was found to be initially very low and slowly increased four weeks after the transfer. While the T cell chimerism increased to about 50 – 60% in recipients that were reconstituted with *Rnaseh2b*$^{WT/WT}$ and *Rnaseh2b*$^{WT/KOF}$ bone marrow from primary recipients, the T cell chimerism of recipients that were reconstituted with

Rnaseh2b$^{KOF/KOF}$ bone marrow also gradually decreased to a level of 15.67 ± 7.66% after 32 weeks (Fig. 3.31).

Final analysis of secondary recipients displayed the greatest cellularity in recipients that were reconstituted with *Rnaseh2b*$^{KOF/KOF}$ bone marrow when compared with mice reconstituted with wild type and heterozygous bone marrow. However, these mice showed low level chimerism in the peripheral blood. Staining for bone marrow stem cells demonstrated reduced absolute KSL, MPP, ST-HSC and LT-HSC cell numbers. Thus, low level chimerism of peripheral blood cells was a likely consequence of reduced stem cell numbers in the bone marrow of secondary recipients. Surprisingly, reduced stem cell numbers could also be observed in the bone marrow of secondary recipients that were reconstituted with Rnaseh2bKOF/KOF bone marrow from primary recipients. Although these mice displayed intermediate absolute cell numbers, the peripheral blood chimerism remained stable and comparable to that of the wild type.

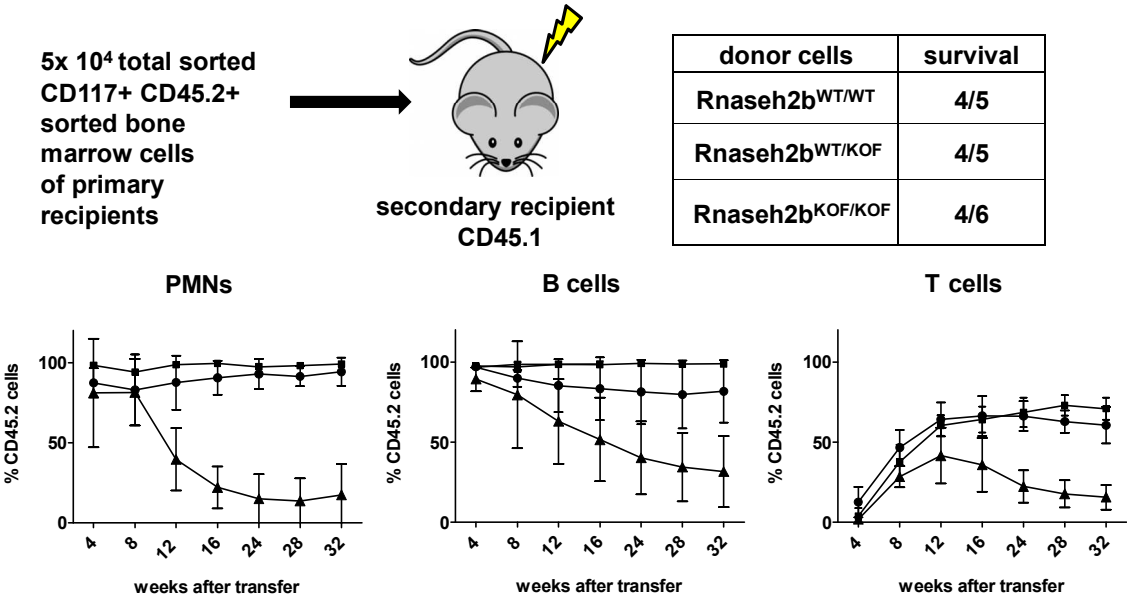

donor cells	survival
Rnaseh2b$^{WT/WT}$	4/5
Rnaseh2b$^{WT/KOF}$	4/5
Rnaseh2b$^{KOF/KOF}$	4/6

Figure 3.31: RNase H2-deficient bone marrow from primary recipients cannot reconstitute secondary recipients. Lethally irradiated (8Gy) secondary recipients were reconstituted with 5x10^4 sorted CD45.2$^+$ CD117$^+$ bone marrow cells from primary recipients. Whereas bone marrow from primary recipients that were either reconstituted with *Rnaseh2b*$^{WT/KOF}$ (n=4, black boxes) or *Rnaseh2b*$^{WT/WT}$ (n=4, black circles) fetal liver cells could stably reconstitute secondary recipients for 32weeks, bone marrow cells from primary recipients that were reconstituted with *Rnaseh2b*$^{KOF/KOF}$ (n=4, black triangles) fetal liver cells failed to reconstitute secondary recipients. Chimerism (% CD45.2 cells) in secondary recipients declined in the PMN-, B cell- and T cell-compartment at different time points, with the most dramatic decline in the population of PMNs that finally dropped to about 15%.

As hypothesized, our data showed that bone marrow cells of primary recipients that were initially reconstituted with RNase H2-deficient E14.5 fetal liver cells did not have the capacity to reconstitute recipients in a secondary transfer experiment. This data clearly

supported our hypothesis that the impact of RNase H2 deficiency is directly linked to the number of cell divisions. So far we cannot conclude what caused the failure to reconstitute recipients in a secondary transfer experiment. Based on our previous data generated from *Rnaseh2b*$^{KOF/KOF}$ embryos, RNase H2 deficiency might have caused increased DNA damage and subsequent cell death in the stem cell compartment. However, increased DNA damage and cell death might have occurred in stem cell progenitor cells leading to increased stem cell activity and subsequent stem cell exhaustion in a chronic setting.

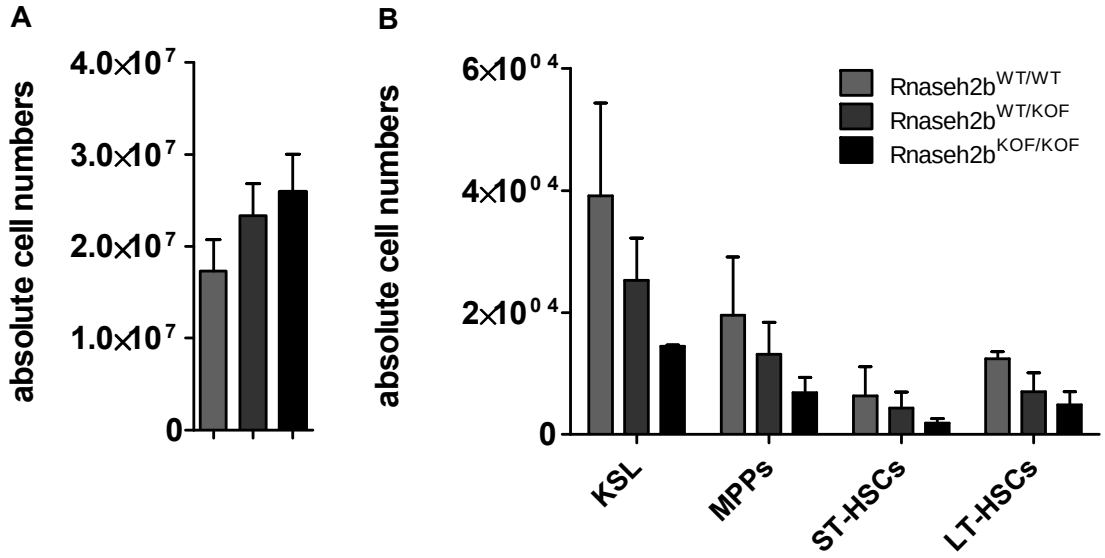

Figure 3.32: Secondary recipients that were reconstituted with knockout bone marrow from primary recipients displayed increased bone marrow cellularity but reduced stem cell numbers. (A) Absolute bone marrow cell numbers per femur were determined of secondary recipients that were either reconstituted with wild type (light grey bars, n = 3), heterozygous (dark grey bars, n = 3) or knockout (black bars, n = 3) bone marrow of primary recipients. **(B)** FACS staining for bone marrow stem cells demonstrated reduced absolute stem cell numbers in mice reconstituted with *Rnaseh2b*$^{KOF/KOF}$ bone marrow of primary recipients.

4 Discussion

4.1 RNase H2-deficient mice do not develop an autoimmune pathology.

The aim of this project was to generate a mouse model for the human encephalopathy Aicardi-Goutières syndrome (AGS) that is caused by mutations in at least seven genes. Three of them encode for the subunits of the heterotrimeric RNase H2 enzyme, while the others encode for TREX1, SAMHD1, ADAR and IFIH1 (MDA5) (Crow et al., 2006a; Crow et al., 2006b; Rice et al., 2009; Rice et al., 2012; Oda et al., 2014; Diamond, 2014). While null mutations can be found in AGS patients with mutations in TREX1 and SAMHD1, mutations in the other genes were rather found to cause a partial loss-of-function or a gain-of-function instead of causing complete deficiency. RNase H2, TREX1 and SAMHD1 were described to possess nuclease activity with different nucleic acid-specificity, while ADAR is a RNA-editing enzyme with deaminase activity. In contrast, the *Ifih1* gene encodes for a RIG I-like helicase MDA5 that senses long double-stranded RNA. However, all share the common feature that mutations in these genes cause the *de-novo* synthesis of type I interferon, a hallmark of the Aicardi-Goutières syndrome. Chronic type I interferon production in AGS patients causes massive inflammation in the brain, dramatic physical and mental retardation and often lethality in early childhood. The current hypothesis is that nucleic acids accumulate in patients with partial loss-of-function mutations in RNase H2, TREX1, SAMHD1 and ADAR that leads to an uncontrolled type I interferon response and subsequent AGS pathology. The gain-of-function mutations in the *IFIH1* gene cause constitutive activity and enhanced ligand-sensitivity, respectively, that leads also to uncontrolled type I interferon expression.

A mouse model for TREX1 deficiency was shown to recapitulate most of the clinical and molecular features of human AGS patients and greatly contributed to the elucidation of AGS pathomechanisms. *Trex1*-deficient mice show multi-organ inflammation (except for the brain) and die of circulatory failure caused by a myocarditis (Morita et al., 2004; Stetson et al., 2008; Gall et al., 2012). However, lethality of *Trex1*-deficient mice could be completely rescued by concomitant *Ifnar1*-, *Irf3*- and *Rag1*-deficiency, showing the important impact of the type I interferon response and lymphocytes on the onset of the disease. Moreover, it could be shown that Trex1 deficiency caused the accumulation of a nucleic acid species that is detected by the nucleic acid sensor cyclic GMP/AMP synthase (cGAS) that activates STING (Stimulator of interferon genes) via the second messenger cGMP/AMP. STING in turn induces the expression of type I interferon via the mediator TBK1 (Tank binding kinase 1) and the transcription factor IRF3 (Ablasser et al., 2014). Yet, the origin of the nucleic acid species is still discussed, either deriving from

DNA replication and repair (Lan et al., 2014) or from retrotransposition of endogenous retroelements (Stetson et al., 2008; Beck-Engeser et al., 2011). *Samhd1*- and *Adar*-deficient mice also display a spontaneous type I interferon response, although *Samhd1* knockout mice do not develop any pathology (Behrendt et al., 2013; Rehwinkel et al., 2013) and lethality of *Adar* knockout mice could only be postponed by few days upon concomitant *Ifnar1*-deficiency (Hartner et al., 2009; Mannion et al., 2014). Concomitant deficiency for the adaptor protein Mavs postponed lethality of Adar-deficient mice to birth

To elucidate the pathomechanism in human AGS patients with mutations in the genes encoding for the RNase H2 enzyme, we generated RNase H2-deficient mice by inactivating one of the three murine genes encoding for the RNase H2 enzyme. We generated mice with ubiquitous deletion of the *Rnaseh2b* and *Rnaseh2c* gene, respectively. However, mice with complete RNase H2 deficiency (*Rnaseh2c*$^{-/-}$ *and* *Rnaseh2b*$^{\Delta/\Delta}$) died during early embryonic development around day 10.5. Knockout mice with hypomorphic RNase H2 expression (*Rnaseh2b*$^{KOF/KOF}$), showing 5% residual enzyme activity, died perinatally or were stillborn (Hiller et al., 2012; Reijns et al., 2012). In line with early embryonic lethality in mice with ubiquitous RNase H2 deficiency, homozygous null mutations have never been observed in AGS patients with mutations in the genes encoding for the RNase H2 enzyme (Rice et al., 2007). All mutations in the genes encoding for the RNase H2 enzyme are missense mutations, implicating that complete RNase H2 deficiency might cause lethality in early mammalian development (Rice et al., 2007). In contrast to the data from mammals, a yeast strain deficient for the RNase H2 enzyme (*rnh201Δ*) did not display lethality or impaired viability, indicating that RNase H2 is not essential during homeostasis in lower eukaryotes (Arudchandran et al., 2000). Even the concomitant deletion of the RNase H1 enzyme in yeast did not cause lethality. Impaired growth of RNase H2-deficient yeast could only be detected upon treatment with DNA-damaging agents, like hydroxyurea (HU) (Arudchandran et al., 2000) Since hydroxyurea prevents the *de novo* synthesis of desoxyribonucleotides by blocking the ribonucleotide reductase, impaired growth was likely caused by increased incorporation and accumulation of ribonucleotides into the genomic DNA.

As a consequence of ubiquitous deletion of RNase H2-encoding genes, knockout mice did not show any (*Rnaseh2c*$^{-/-}$ *and* *Rnaseh2b*$^{\Delta/\Delta}$) or maximal 5% residual activity (*Rnaseh2b*$^{KOF/KOF}$). In contrast to the complete deficiency for the RNase H2 enzyme in mice, overexpression studies have shown that the most frequent human AGS mutations in the B subunit (A177T, V185G) and the C subunit (R69W) are partial loss-of-function mutations with no consequences for the RNase H2 enzyme activity. The G37S mutation in the A subunit was the only mutation shown to reduce RNase H2 activity by directly

affecting the active center of the enzyme (Perrino et al., 2009; Reijns et al., 2011). Since most mutations in the genes encoding for the RNase H2 enzyme do not alter residual enzyme activity, mutations in AGS patients must have other consequences on RNase H2 function. By determining the crystal structure of the human RNase H2 enzyme, Reijns et al. could show that seven mutations (A subunit: R291H; B subunit: A177T; C subunit: R69W, P76L, P138L, K143I and P151S) that are found in AGS patients, affect amino acids located at the interface between the three subunits (Reijns et al., 2011). They could also demonstrate that all seven AGS mutations caused reduced thermal stability of the RNase H2 enzyme and concomitant reduced RNase H2 enzyme activity for almost all mutations. However, the A177T as well as the P138L mutation did not affect enzyme activity again. The authors thus speculated that the A177T and P138L mutation may lead to reduced total RNase H2 protein levels and therefore cause impaired cellular activity (Reijns et al., 2011). A recent publication investigated if AGS mutations might render the localization or the recruitment of the RNase H2 enzyme to sites of DNA damage and repair but could not find any differences for the common A177T and R69W mutation when compared to the wild type RNase H2. Again, only the G37S mutation showed delayed recruitment to DNA damage repair foci (Kind et al., 2014).

Histology of E18.5 or stillborn *RNaseh2b*$^{KOF/KOF}$ mice did not show leukocyte infiltration, neither in the brain nor in any other tissue, clearly demonstrating the absence of an immune response that might have caused lethality. Accordingly, early lethality could not be rescued by additional deficiency for IFNAR1 or RAG1, eliminating the possibility that lethality in *RNaseh2b*$^{KOF/KOF}$ mice was driven by type I interferon or lymphocytes (Hiller et al., 2012). Yeast experiments showed that RNase H2 deficiency caused increased genomic loads of ribonucleotides (Nick McElhinny et al., 2010). Using our own assay to detect the incorporation of ribonucleotides into genomic DNA, we were able to detect increased ribonucleotide loads in knockout cells, however, based on our data we were unable to determine whether single ribonucleotides or stretches of ribonucleotides were incorporated in the absence of the RNase H2 enzyme. Since ribonuclease H1 (RNase H1) is competent to degrade the RNA moiety in RNA:DNA hybrids and can also cleave at positions of at least four subsequent ribonucleotides, RNase H2 deficiency likely caused the accumulation of single ribonucleotides or short stretches of maximal three ribonucleotides in the genomic DNA (Cerritelli and Crouch, 2009). How the presence of single or short stretches of ribonucleotides in genomic DNA cause DNA damage is only incompletely understood. Desoxyribonucleotide triphosphates (dNTPs) and ribonucleotide triphospahtes (rNTPs) differ only at the 2-prime carbon atom (C_2) of the

sugar ring, with the carbon bound to hydrogen in dNTPs while it is bound to a hydroxyl-group in rNTPs. It was described that the nucleophilicity of this particular hydroxyl group renders the DNA more susceptible to strand breaks (Joyce, 1997; Williams and Kunkel, 2014). Although incorporation of ribonucleotides likely cause single-strand breaks, DNA double-strand breaks can result in case two ribonucleotides are in close proximity located on opposing DNA strands or in case the replication fork runs into an unrepaired single-strand break. Kim et al. could also show in yeast that topoisomerase IB is also competent to remove ribonucleotides from genomic DNA in the absence of the RNase H2 enzyme (Kim et al., 2011). However, topoisomerase IB-mediated removal of ribonucleotides is only partial and imperfect, leading to the generation of unligatable 2`, 3`- cyclic phosphate ends. Repair of these ends was shown to cause 2-5 bp deletions, increased dNTP-levels and accumulation of cells in S and G2/M of the cell cycle (Kim et al., 2011; Williams et al., 2013). Collectively, complete RNase H2 deficiency in the mouse rather leads to the accumulation of ribonucleotides in genomic DNA that likely cause DNA single- and double-strand breaks and the activation of a DNA damage response, than causing a type I interferon- and lymphocyte-mediated immune response.

Although we could not specify the DNA damage that arose from the persistent ribonucleotide load in the genomic DNA, we were able to detect the activation of downstream molecules of a DNA damage response upon DNA strand breaks. Thus, a p53 signature could be detected in the gene expression analysis of fetal liver cells from E14.5 *RNaseh2b*$^{KOF/KOF}$ embryos and of total skin from eight week-old *K14Cre*$^{+}$ *Rnaseh2b*$^{FLOX/FLOX}$ mice. The most prominent p53 signature was observed in fetal liver cells from *RNaseh2b*$^{KOF/KOF}$ embryos with the cell cycle inhibitor *Cdkn1a* (*p21*) being the most up-regulated gene of the array and likely explaining the growth arrest in MEF cultures from *Rnaseh2b*-defcient embryos. Fetal liver and fetal thymus cells from E18.5 *RNaseh2b*$^{KOF/KOF}$ embryos also displayed increased numbers of γH2AX foci, a well-known marker for DNA strand breaks (Hiller et al., 2012). Eventually, we also observed transcriptional up-regulation of *Chek1* and *Chek2* in the gene expression analysis of skin from *K14Cre*$^{+}$ *Rnaseh2b*$^{FLOX/FLOX}$ mice. Both markers are important mediators in the DNA damage response pathway, located downstream of the kinases ATM and ATR that are activated upon DNA damage. In theory, double-strand breaks are sensed by ATM while ATR detects single-strand breaks. But since single-strand breaks naturally occur as byproducts during the repair of double-strand breaks, ATR activation cannot exclusively assigned to the repair pathway of single-strand breaks. However, since the described DNA damage response pathway is regulated post-transcriptionally by phosphorylation, we cannot conclude if the transcriptional upregulation of the *Chek1* and *Chek2* gene

represents the activation of the DNA damage response pathway. But it might well be that the transcriptional upregulation might be a consequence of the increased need for the two proteins in the DNA damage response pathway.

Collectively, our data shows that the absence of the RNase H2 enzyme leads to the accumulation of single or short stretches of ribonucleotides in the genomic DNA. These persistent ribonucleotides might in turn cause DNA single- and/or double-strand breaks that trigger a p53-mediated DNA damage response. According to our data, Reijns et al. published similar findings. They could also demonstrate increased genomic ribonucleotides and using the alkaline assay to detect ribonucleotide incorporation they were able to estimate that a single ribonucleotide is incorporated into the DNA every 7600 nucleotides. Moreover, they could also show increased phosphorylation of histone H2AX (γ-H2AX) and the presence of micronuclei and chromosomal rearrangements in *Rnaseh2b*$^{-/-}$ *p53*$^{-/-}$ double knockout cells. This additional data might indicate that RNase H2 deficiency may lead to DNA double-strand breaks that facilitate gross chromosomal rearrangements (Reijns et al., 2012).

4.2 RNase H2-deficient mice likely die of the accumulation of an unknown DNA damage-species.

We showed that mice completely deficient for the RNase H2 enzyme die in early embryogenesis, independent of an immune response involving type I interferon and lymphocytes. Instead, we and others could show that complete RNase H2 deficiency caused the accumulation of ribonucleotides in the genomic DNA that initiated a p53-mediated DNA damage response (Hiller et al., 2012; Reijns et al., 2012).

To bypass this early embryonic lethality, we generated cell type-specific knockout mice. We first deleted the *Rnaseh2b* gene in various cell types of the hematopoietic system. Surprisingly, a B cell-specific knockout of the *Rnaseh2b* gene (*CD19Cre*$^{+}$ *Rnaseh2b*$^{FLOX/FLOX}$) did not show any impact on B cell-homeostasis. Mice were born at Mendelian ratios and B cell numbers from these mice were comparable to B cell numbers from littermate control mice. The same observations were made in mice with a knockout of the *Rnaseh2b* gene in dendritic cells (*CD11cCre*) as well as in monocytes, macrophages and granulocytes (*LysMCre*) (data not shown). LPS-stimulation of *Rnaseh2b*-deficient B cells *in vitro* caused reduced proliferation and impaired progression of B cells through G_2/M of the cell cycle. However, in comparison to mouse embryonic fibroblasts (MEFs) from E14.5 or E18.5 *Rnaseh2b*$^{KOF/KOF}$ embryos, impaired proliferation and accumulation in G_2/M was much milder. In very contrast to the

CD19Cre-specific knockout, a *VavCre*-specific knockout (Stadtfeld and Graf, 2005) of the *Rnaseh2b* gene had a tremendous impact on cell viability. As a consequence of the *VavCre*-specific deletion, all stem cell-derived cells, i.e. all cells of the hematopoietic system, are deficient for the *Rnaseh2b* gene from the very first developmental stage.

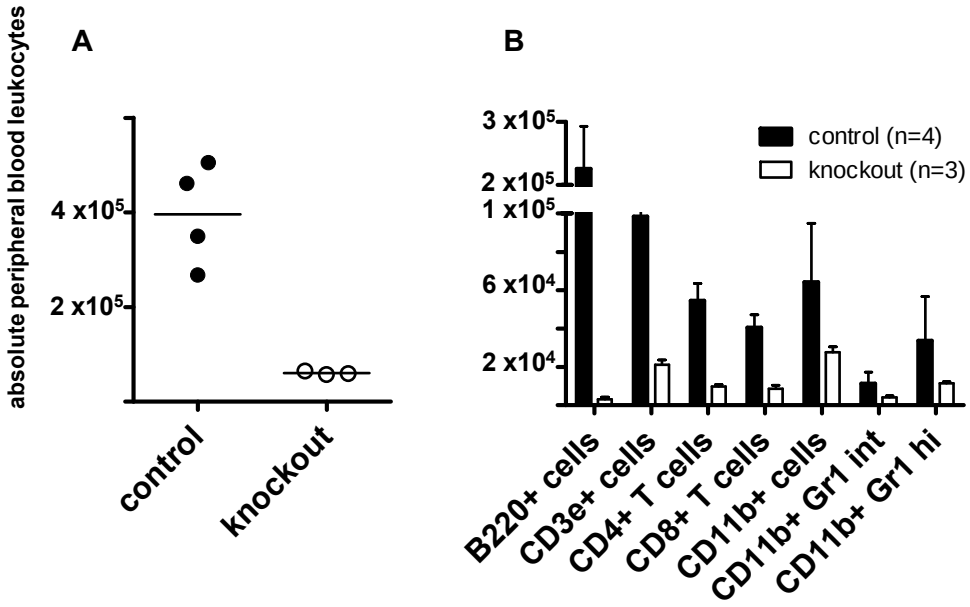

Figure 4.1: Deletion of the *Rnaseh2b* gene in the early hematopoietic stem cell caused massive impact on viability of various cell lineages. Upon *VavCre*-mediated deletion of the *Rnaseh2b* gene in early hematopoietic stem cells, **(A)** total leukocyte numbers in the peripheral blood decreased more than tenfold in knockout mice (open circles, n=3) compared to control littermates (black circles, n=4). **(B)** Flow cytometric analysis of peripheral blood leukocytes showed reduced cell numbers for all investigated cell lineages in knockout mice (white bars, n=3) in comparison to control mice (black bars, n=4). Lymphoid cells appeared more affected than myeloid cells, with B cells displaying the strongest decrease in absolute cell numbers.

VavCre^{+} *Rnaseh2b*$^{FLOX/FLOX}$ mice showed a more than tenfold reduction in peripheral blood leukocyte numbers (Figure 4.1). Analysis of the different leukocyte populations demonstrated a general reduction of cell numbers for all cell types, with lymphoid cells being slightly more affected than myeloid cells. B cells showed the strongest reduction of a hundred fold. We don`t know yet why lymphoid cells seem to be more affected than myeloid cells and why deletion of the *Rnaseh2b* gene in B cells had the strongest impact on cell viability. Based on our previous findings, we think that the number of cell divisions might directly determine the impact of RNase H2 deficiency. Compared to myeloid cells, lymphoid B and T cells are characterized by increased numbers of cell divisions attributed to their unique feature of expressing a surface B and T cell receptor, respectively. This hypothesis might also explain the dramatic differences observed between *CD19Cre*$^{+}$ *Rnaseh2b*$^{FLOX/FLOX}$ and *VavCre*$^{+}$ *Rnaseh2b*$^{FLOX/FLOX}$ mice. While *VavCre* deletes in the very early hematopoietic stem cell, *CD19Cre* deletes rather late in

the pro-B cell stage of B cell development (Figure 4.2) (Stadtfeld and Graf, 2005). Thus, B cells in *CD19Cre*$^{+}$ *Rnaseh2b*$^{FLOX/FLOX}$ mice are characterized by less numbers of cell divisions in the absence of the RNase H2 enzyme compared to B cells from *VavCre*$^{+}$ *Rnaseh2b*$^{FLOX/FLOX}$ mice. Taken together, the observations made in cell type-specific *Rnaseh2b* knockouts might implicate that the number of cell divisions in the absence of the RNase H2 enzyme determines the strength of the phenotypic outcome, i.e. the impact on cell viability.

This idea was further supported by our data obtained from MEF cells from E14.5 *RNaseh2b*$^{KOF/KOF}$ embryos that showed impaired proliferation and progression through G_2/M when compared to control cells. Moreover, impaired proliferation exacerbated with cultivation time, and MEF cells generated from E18.5 *RNaseh2b*$^{KOF/KOF}$ embryos showed an even stronger phenotype with most of the cells already in G2/M phase of the cell cycle (Hiller et al., 2012).

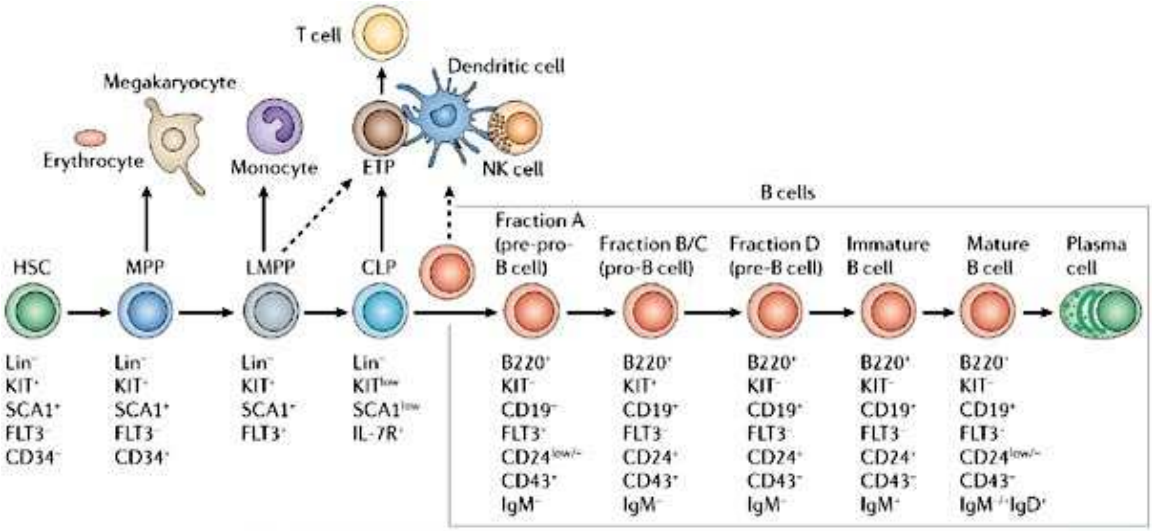

Figure 4.2: B cell development starting from the hematopoietic stem cell (adopted from Nagasawa T., *Nature Reviews Immunology* 6 (107-116), 2006, (Nagasawa, 2006))
The hematopoietic stem cells (HSC), residing in particular niches of the bone marrow maintain the hematopoietic system by their self-renewal capacity, giving rise to a daughter cell that can differentiate to any cell type of the hematopoietic system, while the remaining daughter cell keeps the potency. During differentiation and maturation, cells lose their capability to differentiate to all cells of the hematopoietic system. While multi potent progenitors (MPPs) can give rise to cells of the lymphoid and myeloid compartment, common lymphoid progenitors (CLPs) can only give rise to lymphoid cells. B cells are derived from the CLPs but undergo several additional maturation steps characterized by the expression of different cell surface markers. CD19 is expressed in the pro-B cell that is situated later in B cell development compared to the expression of the *Vav* gene that takes place in the early hematopoietic stem cell (HSC).

In line with the above findings are also the observations made in the transfer experiments to obtain bone marrow chimera. Our data showed that RNase H2-deficient fetal liver cells from E14.5 *RNaseh2b*$^{KOF/KOF}$ embryos were competent to reconstitute

lethally irradiated mice, either in a non-competitive or competitive setting (data not shown). Primary recipients in the non-competitive setting that were reconstituted with RNase H2-deficient fetal liver cells or control fetal liver cells showed a chimerism of about 100% that remained stable during the entire experiment. However, bone marrow cells from these primary recipients were not competent to reconstitute irradiated mice in a secondary bone marrow transfer experiment. Failure to reconstitute secondary recipients could be observed as dramatic decrease in peripheral blood chimerism in B cells, T cells and polymorphonucleated cells (PMNs). B cell- and PMN- chimerism rapidly decreased, while T cell-chimerism dropped after a short period of latency. The different kinetics of the peripheral blood chimerism can well be explained by the different turnover of the cells. PMNs, showing the most rapid decrease, are characterized by the shortest turnover of about 14 days (Bainton et al., 1971). In contrast, T cells are long-lived, radio-resistant cells that have a monthly turnover (Jameson, 2002). Finally, our data demonstrate that *Rnaseh2b*-deficient stem and progenitor cells have only a limited capacity to reconstitute irradiated mice when compared to stem and progenitor cells from wild type and *Rnaseh2b*$^{WT/KOF}$ mice. This limited capacity does not allow for repetitive transfer of bone marrow cells. Again, this failure to stably reconstitute secondary recipient mice might be directly linked to the number of cell divisions. To reconstitute the empty niche space in primary recipients, donor hematopoietic stem cells and commited progenitor cells (common lymphoid (CLPs) and common myeloid progenitors (CMPs)) have to proliferate massively. When these cells are used to reconstitute secondary recipients, donor hematopoietic stem and committed progenitor cells have to proliferate massively again.

Based on our previous observations made in cell type-specific knockout mice and in MEF cells from E14.5 and E18.5 *Rnaseh2b*$^{KOF/KOF}$ embryos, we suggest that the reduced capacity to reconstitute secondary recipient mice was a consequence of a particular DNA damage species that accumulated during massive cell proliferation. We think that the deficiency for the RNase H2 enzyme and the concomitant increased loads of ribonucleotides might lead to the accumulation of DNA damage with every cell division. In the absence of the RNase H2 enzyme, ribonucleotides that are incorporated during replication cannot be removed and persist in the genomic DNA (Rydberg and Game, 2002; Reijns et al., 2012; Hiller et al., 2012). However, the most important question that came up from these observations was what kind of DNA damage might have been generated in the absence of the RNase H2 enzyme? Why can`t the damage be efficiently repaired? And why does its nature allow for a certain number of cell divisions before cells die?

Because of the semiconservative replication of the genomic DNA it seems unlikely that it is the number of ribonucleotides that increased with rounds of proliferation, accounting for the observed phenotype. During each round of replication one DNA strand serves as a template for the complementary DNA strand to be newly synthesized. Therefore, ribonucleotides are only incorporated into one DNA strand while the other remains unaltered. Thus, the number of ribonucleotides can only increase during the first two replication rounds, whereas the number of ribonucleotides remains largely stable during every subsequent replication, considering that ribonucleotides are incorporated with the same probability during each replication. Therefore, ribonucleotide accumulation cannot explain the immediate proliferation defect after several rounds of normal proliferation. There is the possibility that ribonucleotide incorporation may lead to a different distribution pattern of ribonucleotides in the genomic DNA. Random incorporation might cause the localization of two ribonucleotides in close proximity on complementary DNA strands, facilitating the generation of DNA double-strand breaks. Again, this hypothesis would not explain the observations above that the proliferation defect suddenly occurred after a period of normal growth and proliferation. The accumulation of RNase H2-deficient cells in G2/M of the cell cycle might indicate checkpoint activation upon the detection of single- and/or double-strand breaks in the newly synthesized DNA. However, this kind of damage would be immediately repaired since it poses a big threat to the genomic information and all cells are well equipped with multiple DNA repair pathways to be able to fix various types of common DNA damage (Harper and Elledge, 2007). If the damage could not be repaired, these cells would likely be immediately erased by apoptosis.

Since this is true for all human and mouse somatic cells, stem cells behave different and are equipped with additional features that help to maintain and to propagate the correct genomic information. In contrast to somatic cells, hematopoietic stem cells are quiescent cells that rarely cycle and are mainly in G_0 of the cell cycle. As described above, while one daughter maintains full stem cell potency, the other daughter cell can differentiate to all cells of the hematopoietic system. The maintenance of the hematopoietic system mainly relies on the totipotency of the stem cells and the high proliferation rate of stem cell-derived cells. Together with a unique DNA damage repair pathway these properties prevent the generation of mutations, their propagation and the development of cancer. If persistent genomic ribonucleotides would cause the generation of a new species of strand breaks that cannot be immediately repaired, damaged cells would likely undergo apoptosis to prevent mutations and their propagation or would re-enter quiescence. Since the accumulation of DNA damage in hematopoietic stem cells is rather unlikely

due to their unique properties, failure of RNase H2-deficient bone marrow cells to reconstitute secondary recipients might be caused as a secondary effect in response to increased damage in stem cell-derived hematopoietic cells. If increased DNA damage in these cells would cause increased apoptosis, hematopoietic stem cells are enforced to enter the cell cycle and replenish the lost cells to maintain the function of the hematopoietic system. However, the capacity to cycle is limited in hematopoietic stem cells and chronic activation might cause their exhaustion. This hypothesis is well supported by the findings in *K14Cre*$^{+}$ *Rnaseh2b*$^{FLOX/FLOX}$ mice that lose hair as a consequence of exhaustion and loss of hair follicle stem cells.

As was shown for yeast and human, topoisomerase I could cleave at sites where ribonucleotides were inserted (Sekiguchi and Shuman, 1997; Kim et al., 2011). But topoisomerase I-mediated cleavage was shown to cause 2-5 bp deletions, increased dNTP levels and accumulation in the S and G2/M phase of the cell cycle. The consequences of topoisomerase I-mediated cleavage of ribonucleotides could not yet be shown for higher eukaryotes. It might likely be that topoisomerase I-mediated cleavage might generate a so far unknown DNA damage that allows for a limited number of cell divisions until a certain threshold of damage is reached that does not allow for further proliferation.

4.3 The *K14Cre*$^{+}$ *Rnaseh2b*$^{FLOX/FLOX}$ mouse could be a valuable mouse model for the investigation of SLE pathomechanisms

Besides deletion of the *Rnaseh2b* gene in cells of the hematopoietic system, we also bred the *Rnaseh2b*^{FLOX} mouse to a *K14Cre*-expressing mouse line. Keratin 14 (K14) is expressed in cells of the epidermal basal membrane, causing Cre-mediated deletion of the *Rnaseh2b* gene in the entire epidermis starting at day E12 of embryonic development (Vasioukhin et al., 2001). Unlike *Rnaseh2b*$^{KOF/KOF}$ mice, *K14Cre*$^{+}$ *Rnaseh2b*$^{FLOX/FLOX}$ mice were viable and born at Mendelian ratios. *K14Cre*$^{+}$ *Rnaseh2b*$^{FLOX/FLOX}$ mice soon developed a severe skin phenotype, manifesting as hyperpigmented skin limited to the tail, paws and ears, loss of hair and spontaneous skin ulcerations. Microscopically, increased thickness of the epidermis and dermis could be detected. While the epidermis was only modestly affected, *K14Cre*$^{+}$ *Rnaseh2b*$^{FLOX/FLOX}$ mice displayed massive dermal alterations with interface dermatitis and fibrotic changes. In order to elucidate the molecular cause that accounted for the dramatic pathological changes in the skin of *K14Cre*$^{+}$ *Rnaseh2b*$^{FLOX/FLOX}$ mice, like hyperpigmentation, hair loss

and fibrosis, we studied the literature and found data describing similar pathology for mouse models that were associated with DNA damage.

Cui et al. investigated the regulative role of the tumor suppressor gene *p53* in the process of hyperpigmentation upon UV light exposure (Cui et al., 2007), a phenomenon known as suntan response. They could demonstrate that UV light exposure caused DNA damage in the skin of mice, leading to DNA damage-induced activation of p53. DNA damage-induced activation of p53 led to its translocation into the nucleus where it activated the *Pomc* gene encoding for the melanin precursor pro-opiomelanocortin. As a consequence of increased pro-opiomelanocortin expression and the subsequent *de novo* synthesis of melanin, the skin of mice that were exposed to UV light became hyperpigmented. Sotiropoulou et al. generated a K14Cre-specific knockout of the *Brca1* gene (Sotiropoulou et al., 2013) . Breast cancer 1 (*Brca1*) encodes for an important transducer in the DNA damage repair pathway that is activated upon DNA double-strand breaks (Roy et al., 2011). BRCA1 mediates homologous recombination in the S and G2/M phase of the cell cycle (Moynahan et al., 1999). Mice deficient for the *Brca1* gene in the epidermis were born hairless. Sotiropoulou et al. could demonstrate that BRCA1 deficiency caused elevated p53 levels and increased DNA damage and apoptosis in the hair follicle of $K14Cre^{+}$ $Brca1^{FLOX/FLOX}$ mice. Surprisingly, pathology could only be observed in the matrix cells of the lower hair follicle, while the pathology was absent in the upper hair follicle, the isthmus and the interfollicular epidermis (IFE). The authors concluded that increased apoptosis in *Brca1*-deficient matrix cells has led to the chronic activation of hair follicle stem cells that caused their exhaustion and subsequent hair loss (Sotiropoulou et al., 2013). Most importantly, p53-mediated hyperpigmentation as well as hair loss could both be prevented by concomitant deficiency for the *p53* gene in both experimental settings, indicating the important role of the tumor suppressor gene *p53* in the pathology associated to DNA damage. While p53-deficient mice did not display hyperpigmentation upon UV light exposure, $K14Cre^{+}$ $Brca1^{FLOX/FLOX}$ $p53^{-/-}$ mice did not show any hair loss (Cui et al., 2007; Sotiropoulou et al., 2013). Based on the data from the literature and our own previous data we think that the pathology of $K14Cre^{+}$ $Rnaseh2b^{FLOX/FLOX}$ mice might also be mediated by the tumor suppressor p53. Gene expression analysis of total skin from eight week-old $K14Cre^{+}$ $Rnaseh2b^{FLOX/FLOX}$ mice revealed a profound p53 signature, as well as the upregulation of mediators of the DNA damage repair pathway (*Chek1*, *Chek2* and *Brca1*). Concomitantly, genes clustering to the eumelanin synthesis pathway were significantly up-regulated. This data might indicate that hyperpigmentation in $K14Cre^{+}$ $Rnaseh2b^{FLOX/FLOX}$ mice was also caused by a p53-mediated DNA damage response and hyperpigmentation in these mice can

therefore be regarded as a mimic of the suntan response observed in mice exposed to UV light. However, we cannot conclude if hyperpigmentation in the skin of *K14Cre*$^{+}$ *Rnaseh2b*$^{FLOX/FLOX}$ mice was caused by increased melanin biosynthesis of residual melanocytes or whether it was caused by elevated numbers of melanocytes. Subsequent staining for melanocytes in skin sections from *K14Cre*$^{+}$ *Rnaseh2b*$^{FLOX/FLOX}$ mice is needed to answer this question. Although we believe that RNase H2 deficiency caused systemic p53 activation, hyperpigmentation could only be observed in the skin of the tail, ears and paws. This observation can likely be explained by the restricted presence of melanocytes in the IFE of skin that is not covered with fur (Quevedo and Fleischmann, 1980). Due to their function to protect the deep skin layers from harmful radiation, melanocytes are completely absent in the IFE of skin that is protected from light by the fur. Therefore, systemic p53 activation in the skin of *K14Cre*$^{+}$ *Rnaseh2b*$^{FLOX/FLOX}$ mice did not cause increased melanin biosynthesis outside the skin of the tail, ears and paws.

Increased DNA damage and the p53 signature in *K14Cre*$^{+}$ *Rnaseh2b*$^{FLOX/FLOX}$ mice might also explain the loss of hair in these mice. So far we were unable to detect increased DNA damage or elevated apoptosis rates in the skin of *K14Cre*$^{+}$ *Rnaseh2b*$^{FLOX/FLOX}$ mice. However, FACS analysis of epidermal cells from 11-13 week-old *K14Cre*$^{+}$ *Rnaseh2b*$^{FLOX/FLOX}$ mice revealed massive reduction of hair follicle stem cells and suprabasal hair follicle stem cells. So far we do not know whether reduction was caused by stem cell exhaustion in response to increased apoptosis of a certain hair follicle cell population.

In line with the important role of p53, hyperpigmentation and hair loss was completely prevented by concomitant deletion of the *p53* gene, indicating that the pathology in *K14Cre*$^{+}$ *Rnaseh2b*$^{FLOX/FLOX}$ mice was mediated by p53 activity. *K14Cre*$^{+}$ *Rnaseh2b*$^{FLOX/FLOX}$ mice with a heterozygous knockout of the *p53* gene (*K14Cre*$^{+}$ *Rnaseh2b*$^{FLOX/FLOX}$ *p53*$^{+/-}$) showed intermediate pigmentation when compared to *K14Cre*$^{+}$ *Rnaseh2b*$^{FLOX/FLOX}$ mice and wild type mice, showing that half levels of p53 caused already an amelioration of the skin phenotype in respect to the hyperpigmentation. *K14Cre*$^{+}$ *Rnaseh2b*$^{FLOX/FLOX}$ *p53*$^{-/-}$ mice (n=4) that were so far born were almost indistinguishable from their wild type littermate controls within the first few weeks of age. With about 12 weeks, *K14Cre*$^{+}$ *Rnaseh2b*$^{FLOX/FLOX}$ *p53*$^{-/-}$ mice appeared sick and showed macroscopical skin alterations (n=3) and the development of cancer (n=1). *K14Cre*$^{+}$ *Rnaseh2b*$^{FLOX/FLOX}$ *p53*$^{-/-}$ mice did not display massive hair loss until the age of 12 weeks, at a time point where *K14Cre*$^{+}$ *Rnaseh2b*$^{FLOX/FLOX}$ mice have already lost most of the dorsal fur. However, selective loss of hair could be observed in the neck, most likely as a

consequence of increased scratching. We could also observe tumor formation in *K14Cre*$^{+}$ *Rnaseh2b*$^{FLOX/FLOX}$ *p53*$^{+/-}$ mice, appearing in older mice and significant incidence. Therefore, our data might show for the first time that RNase H2 deficiency may promote tumor formation as it was already suggested due to the mutator phenotype observed in RNase H2-deficient yeast (Crow et al., 2006b). Further studies, will provide information about kinetics and incidences of tumor formation as well as a detailed description of the tumor species.

According to our data, reduced hair follicle stem cells and suprabasal hair follicle stem cells might also be a consequence of the interface dermatitis observed in the skin of 7 week-old *K14Cre*$^{+}$ *Rnaseh2b*$^{FLOX/FLOX}$ mice. The pathology of interface dermatitis manifests at the dermo-epidermal junction and is caused by a leukocyte infiltration (mainly cytotoxic T lymphocytes) that leads to apoptosis of keratinocytes and vacuolization of basal cells (Joshi, 2013). Therefore, leukocyte infiltration located in proximity of the bulge region of the hair follicle might cause the destruction of the hair follicle stem cells in the bulge region. This discrete leukocyte infiltration restricted to the hair follicle and consisting of only few numbers of infiltrating leukocytes (cell-poor infiltrate) is typically observed but not specific for human patients suffering from cutaneous lupus erythematosus (CLE) (Sontheimer, 2009b). Together with the data showing a possible type I interferon response (see Figure 3.20) in the skin of *K14Cre*$^{+}$ *Rnaseh2b*$^{FLOX/FLOX}$ mice, our data might show for the first time a lupus-like phenotype in a mouse model for RNase H2 deficiency. However, since gene expression analysis of total skin from eight week-old mice did not reveal the upregulation of type I interferon-stimulated genes further investigations are needed to prove this hypothesis. Since we detected increased Sca1 surface expression on epidermal leukocytes, epidermal leukocytes might be a promising target of detailed analysis to test for the expression of a type I interferon response. Due to their low frequency in the epidermis, a type I interferon signature deriving from these cells might be likely diluted by the large number epidermal keratinocytes. Moreover, type I interferon expression might be limited to only a certain cell type of epidermal hematopoietic cells, like Langerhans cells, that have a very low frequency of total epidermal cells and type I interferon of these cells might likely be even more diluted and therefore even more difficult to detect.

Along with hyperpigmentation and loss of hair, *K14Cre*$^{+}$ *Rnaseh2b*$^{FLOX/FLOX}$ mice displayed fibrosis characterized by increased dermal thickness and concomitant tight package of dermal structures. Immunohistochemistry demonstrated increased collagen deposition and leukocyte infiltration in the dermis. We wondered why the deficiency for the RNase H2 enzyme in the epidermis caused fibrosis in the dermis. Data from human

patients suffering from idiopathic pulmonary fibrosis provided important insights in understanding the molecular mechanisms that could have caused fibrosis in *K14Cre*$^{+}$ *Rnaseh2b*$^{FLOX/FLOX}$ mice. Idiopathic pulmonary fibrosis belongs to a family of diseases that is collectively termed 'telomere syndromes' and that further encompasses diskeratosis congenita and aplastic anemia (Armanios and Blackburn, 2012). Pathology in 'telomere syndromes' is caused by mutations in the genes encoding for the telomerase reverse transcriptase (*TERT*), the RNA component (*TR*) as well as dyskerin (*DKC1*). Collectively, the products of these three genes represent important components of the telomerase complex, an important enzyme that maintains the DNA-protein complex at the chromosomal ends, termed the telomere (Nandakumar and Cech, 2013). Due to the inability of the replication machinery to duplicate the DNA at the chromosomal ends, replication would inevitably cause the shortening of those. Thus, telomerase activity prevents the shortening of the telomeres by adding tandem repeats of six nucleotides (TTAGGG) during S and G2 phase of the cell cycle. Deficiency for the telomerase enzyme was shown trigger replicative senescence, a state in which cells maintain metabolic functions but remain in G_0 of the cell cycle. Moreover, telomere-initiated senescent cells display a DNA damage response similar to the DNA damage response observed in cells treated with ionizing radiation (d'Adda di Fagagna et al., 2003). It is characterized by phosphorylation of the DNA damage sensors ATM and ATR, the downstream signal transducers CHK1 and CHK2 as well as the mediator histone 2AX (H2AX). It is believed that the chronic DNA damage response in telomere-initiated senescent cells might cause increased stem cell activation and subsequent exhaustion of those, due their limited proliferation capacity. Senescence and apoptosis of epidermal cells in IPF patients stimulate remodeling of the lung tissue that manifests as fibrosis. However, mice with short telomeres did not initially display lung disease or fibrosis and a second hit (i.e. exposure to cigarette smoke) was necessary to induce lung fibrosis (Armanios, 2012). The need for the second hit might indicate that increased cell proliferation, i.e. a high cell turnover, is needed in addition to the shortened telomeres for the development of fibrosis (Pardo and Selman, 2002)

According to the pathology in IPF patients, fibrosis in *K14Cre*$^{+}$ *Rnaseh2b*$^{FLOX/FLOX}$ mice might be a consequence of increased DNA damage and subsequent apoptosis of RNase H2-deficient epidermal cells. As discussed earlier, so far we could not detect increased DNA damage or elevated apoptosis in these cells, but reduction of hair follicle stem cell numbers might be a consequence of increased DNA damage in these cells. As in IPF patients, DNA damage and apoptosis might likely cause stem cell exhaustion. Therefore, RNase H2 deficiency might also cause exhaustion of interfollicular epidermis stem cells

and subsequent remodeling of the underlying dermis. We cannot conclude whether a second trigger for the generation of fibrosis was needed in *K14Cre*$^{+}$ *Rnaseh2b*$^{FLOX/FLOX}$ mice. It might be that the DNA damage response itself, being stronger than the DNA damage response in telomere-initiated senescent cells, might have caused fibrosis and a second hit was not necessary. Finally, it might be that there was already an unknown second trigger for the generation of fibrosis, like a barrier defect. Pathologic changes in the dermis could also be a consequence of an impaired barrier function of the epidermis in *K14Cre*$^{+}$ *Rnaseh2b*$^{FLOX/FLOX}$ mice. Reduced barrier function of the epidermis might result from impaired keratinocyte function that is caused by the chronic DNA damage and apoptosis. To develop and maintain the barrier function of the skin, it is important that epidermal keratinocytes have the capability to differentiate from the epidermal stem cell that is located in the basal membrane to cells of the stratum granulosum and cells of the stratum corneum that represent the outer most body layers and thus have an important protective function. In order to maintain barrier function, cells of the stratum granulosum need to form tight junctions to adjacent cells, creating a strong physical and mechanical barrier for invading pathogens and other substances but also to avoid transepidermal water loss. Reduced barrier function in *K14Cre*$^{+}$ *Rnaseh2b*$^{FLOX/FLOX}$ mice could therefore be a result of the inability of DNA damage-containing keratinocytes to differentiate to cells of the stratum granulosum and stratum corneum, but also by impaired formation of tight junctions between keratinocytes in the stratum granulosum.

Based on the above findings, we propose the *K14Cre x Rnaseh2b*^{FLOX} mouse line as a new model for fibrotic diseases (Fig. 4.3). Central to this model is the epidermis-specific deletion of the *Rnaseh2b* gene that leads to increased ribonucleotide loads in the genomic DNA causing a chronic p53-mediated DNA damage response. However, we do not know yet, why the deficiency for the RNase H2 enzyme in the epidermis leads to massive alterations in the dermis.

We hypothesize that the DNA damage response in RNase H2-deficient epidermal keratinocytes leads to increased apoptosis of these cells. As one potential consequence, quiescent, non-cycling epidermal stem cells might be activated in order to compensate for dying cells and to maintain skin function. Due to the chronicity of the DNA damage and the subsequent persistent apoptosis of RNase H2-deficient cells, epidermal stem cells might exhaust, causing the remodeling of the underlying tissue as in IPF patients. Concomitant leukocyte infiltration might be independent of the remodeling in this setting. As another consequence of the chronic DNA damage and persistent apoptosis in RNase H2-deficient epidermal cells, epidermis might lose its important barrier function. Loss of

the barrier function would allow for the penetration of pathogens or other stimulatory substances that could elicit an inflammatory immune response. Chronic inflammation could subsequently result in the remodeling of the dermis induced by increased collagen production by dermal fibroblasts. As another possibility, fibrosis of the dermis could be a consequence of the interface dermatitis. Although the exact origin for the development of interface dermatitis is not yet completely understood, interface dermatitis goes along with inflammation. Leukocyte infiltration in the bulge region of the hair follicle might cause T cell-mediated destruction of hair follicle stem cells and the loss of hair. Collectively, leukocyte infiltration and stem cell destruction might cause remodeling of the dermis. However, subsequent studies will help to elucidate the pathomechanisms that causes dermal fibrosis in response to the deficiency for the RNase H2 enzyme in the epidermis.

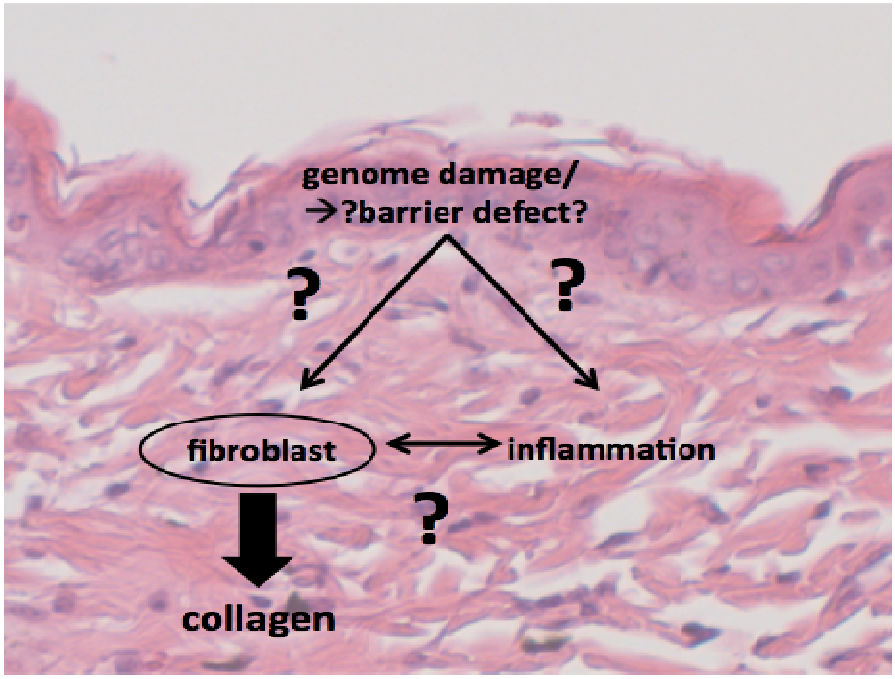

Figure 4.3: The *K14Cre*$^{+}$ *Rnaseh2b*$^{FLOX/FLOX}$ mouse, a new mouse model for fibrosis. Deficiency for the RNase H2 in the epidermis causes the accumulation of genomic ribonucleotides that induces a p53-mediated DNA damage response. As a consequence, massive alterations occur in the dermis that manifest as dermal fibrosis, characterized by increased collagen deposition and concomitant mild inflammation. However, the origins of the phenotypic changes detected in the skin of *K14Cre*$^{+}$ *Rnaseh2b*$^{FLOX/FLOX}$ mice are not completely understood so far. Several pathomechanisms could in theory lead to the fibrotic changes of the dermis and further studies are needed for their elucidation.

4.4 Future perspectives

Our data has shown that deficiency for the RNase H2 enzyme leads to the accumulation and persistence of ribonucleotides in the genomic DNA. By rendering the DNA sensitive

to DNA strand breaks, by the imperfect removal mediated by the topoisomerase I or by a so far unknown mechanism, ribonucleotides cause a p53-mediated DNA damage response. Our data implicates that the impact of RNase H2 deficiency is linked to the number of cell divisions, suggesting that a so far unknown DNA damage species accumulates during each round of proliferation. One important future aim will be to characterize this DNA damage species. So far we were just able to detect the consequences of the DNA damage that are caused by the persistence of genomic ribonucleotides. Our future experiments will therefore focus on the elucidation of the initial damage and the DNA damage repair pathway that is activated upon the damage. To this end, we would like to perform Western Blot analysis of total proteins obtained from cells that display impaired proliferation, loss of function and lethality after a period of normal growth and function. As mentioned above, since members of the different DNA damage repair pathways are regulated by posttranscriptional modifications, we would like to stain for phosphorylated members of distinct DNA repair pathways. Western Blot analysis should help us to elucidate whether persistent ribonucleotides cause the generation of single-strand breaks, double-strand breaks or any other species of DNA damage. We hope that the species of DNA damage might help us to understand how this damage can accumulate and why it is not efficiently repaired or why it is not repaired at all. Knowing the exact DNA damage would allow the investigation of the respective DNA damage checkpoint, whether it is active or inactive. To address the same question we would also like to perform gene expression analysis of the same cells. Although, gene expression analysis can only provide information about the deregulation of genes and is not suitable to detect posttranscriptional modifications, it provides information about the transcriptional regulation of the entire genome. This large overview might allow for the detection of deregulated genes that are not member of a DNA damage repair pathway, but might play a role in the pathology.

Another future aim will be to elucidate the pathology in *K14Cre*$^{+}$ *Rnaseh2b*$^{FLOX/FLOX}$ mice. So far we do not know why the absence of the RNase H2 enzyme in keratinocytes causes the complex pathology in the skin of these mice. Beside massive alterations in the epidermis, we also detected massive transformation of the dermis. Although we performed gene expression analysis of RNA from total skin of eight week-old *K14Cre*$^{+}$ *Rnaseh2b*$^{FLOX/FLOX}$ mice and of RNA from the epidermis of *K14Cre*$^{+}$ *Rnaseh2b*$^{FLOX/FLOX}$ newborn mice, we do not know yet the mechanism that is responsible for the pathology. Gene expression analysis of the epidermis from newborn mice demonstrated that RNase H2 deficiency has yet only a mild effect on the homeostasis of the epidermis, indicated by a low number of deregulated genes and the absence of a DNA damage response that

could be observed so far in all other assays. Genes with functions in cell metabolism and the *de novo* synthesis of melanin were found to be up-regulated, most likely reflecting increased proliferation and hyperpigmentation of the skin. Gene expression analysis of total skin from *K14Cre*$^{+}$ *Rnaseh2b*$^{FLOX/FLOX}$ mice provided more information, displaying a p53-mediated DNA damage response similar that found in the gene expression profile of fetal liver cells from *Rnaseh2b*$^{KOF/KOF}$ mice. As discussed above, we could also found genes to be up-regulated that are important mediators of a DNA damage response upon DNA single- and double-strand breaks. Due to their overlap and their posttranscriptional regulation, we cannot conclude if their transcriptional upregulation is reflecting their activation, but hope to answer this question by Western Blot analysis. The fibrotic phenotype in the dermis of *K14Cre*$^{+}$ *Rnaseh2b*$^{FLOX/FLOX}$ mice might also be a consequence of a barrier defect caused by the p53-mediated DNA damage response. Future experiments will focus on the detection of trans-epidermal water loss as indication of a barrier defect. So far, we could not detect increased trans-epidermal water loss in newborn *K14Cre*$^{+}$ *Rnaseh2b*$^{FLOX/FLOX}$ mice, but we suggest detecting increased trans-epidermal water loss in older mice that already display massive epidermal changes like hair loss and spontaneous ulcerations. In this case we will have to demonstrate what causes the barrier defect. To this end, we will check for the layer-specific expression of various keratins and loricrin by staining of histological skin sections. This staining furthermore allows for the evaluation of the proper expression and function of the different epidermal cell layers. Additionally, we will also determine the cell death rate in the epidermis. Since we have observed a massive increase in cell proliferation by Ki67 staining, we are also expecting higher levels of cell death to compensate for increased cell proliferation. In case cell death exceeds cell proliferation, increased rates of cell death would likely explain a barrier defect and the spontaneous ulcerations. Of particular value will also be *K14Cre*$^{+}$ *Rnaseh2b*$^{FLOX/FLOX}$ *p53*$^{-/-}$ mice, since they will demonstrate the consequences of RNase H2 deficiency independent of a p53-mediated DNA damage response. As one double knockout already showed, hyperpigmentation and hair loss are completely absent in these mice and microscopical alterations are less pronounced as in *K14Cre*$^{+}$ *Rnaseh2b*$^{FLOX/FLOX}$ mice. Moreover, concomitant deletion of the Rnash2b gene and the p53 gene in the epidermis caused cancer formation, indicating that RNase H2 deficiency could render mice prone to develop cancer, as it was already suggested from studies in yeast. However, to evaluate the consequences of concomitant p53 deficiency needs further investigation of more double knockout mice.

Finally, we aim to investigate the consequences of heterozygous deletion of the *Rnaseh2b* and *Rnaseh2c* gene, respectively. As described earlier for human AGS

patients, mutations in any of the three genes encoding for the RNase H2 enzyme cause a partial loss of function instead of the complete inactivation. Therefore we hope that a reduction of the transcript levels of the *Rnaseh2b* and *Rnaseh2c* gene by 50% might be a better mouse model for AGS. Although we have not observed any spontaneous phenotype in these mice, we still think that these mice could be a valuable tool to study AGS pathology. Based on our recent findings we think that cells of *Rnaseh2b*$^{WT/KOF}$ or *Rnaseh2c*$^{+/-}$ mice need to be challenged by increased proliferation rates to display AGS pathology. Therefore we aim to perform repetitive transfers of bone marrow from *Rnaseh2b*$^{WT/KOF}$ or *Rnaseh2c*$^{+/-}$ mice versus control mice. A pilot experiment already showed a growth disadvantage of *Rnaseh2c*$^{+/-}$ bone marrow cells after the third repetitive transfer, when compared to wild type controls. These cells would also be a valuable tool to investigate by Western Blot analysis or gene expression analysis.

5 References

Ablasser A, Bauernfeind F, Hartmann G, Latz E, Fitzgerald KA, Hornung V. 2009. RIG-I-dependent sensing of poly(dA:dT) through the induction of an RNA polymerase III-transcribed RNA intermediate. Nat Immunol 10:1065-1072.

Ablasser A, Hemmerling I, Schmid-Burgk JL, Behrendt R, Roers A, Hornung V. 2014. TREX1 deficiency triggers cell-autonomous immunity in a cGAS-dependent manner. J Immunol 192:5993-5997.

Agmon-Levin N, Mosca M, Petri M, Shoenfeld Y. 2012. Systemic lupus erythematosus one disease or many? Autoimmun Rev 11:593-595.

Aguilera A, Garcia-Muse T. 2012. R loops: From transcription byproducts to threats to genome stability. Mol Cell 46:115-124.

Aicardi J, Goutieres F. 1984. A progressive familial encephalopathy in infancy with calcifications of the basal ganglia and chronic cerebrospinal fluid lymphocytosis. Ann Neurol 15:49-54.

Akira S, Uematsu S, Takeuchi O. 2006. Pathogen recognition and innate immunity. Cell 124:783-801.

Alarcon-Riquelme ME. 2006. Nucleic acid by-products and chronic inflammation. Nat Genet 38:866-867.

Armanios M. 2012. Telomerase and idiopathic pulmonary fibrosis. Mutat Res 730:52-58.

Armanios M, Blackburn EH. 2012. The telomere syndromes. Nat Rev Genet 13:693-704.

Arudchandran A, Cerritelli S, Narimatsu S, Itaya M, Shin DY, Shimada Y, Crouch RJ. 2000. The absence of ribonuclease H1 or H2 alters the sensitivity of saccharomyces cerevisiae to hydroxyurea, caffeine and ethyl methanesulphonate: Implications for roles of RNases H in DNA replication and repair. Genes Cells 5:789-802.

Bainton DF, Ullyot JL, Farquhar MG. 1971. The development of neutrophilic polymorphonuclear leukocytes in human bone marrow. J Exp Med 134:907-934.

Bakkenist CJ, Kastan MB. 2003. DNA damage activates ATM through intermolecular autophosphorylation and dimer dissociation. Nature 421:499-506.

Beck-Engeser GB, Eilat D, Wabl M. 2011. An autoimmune disease prevented by anti-retroviral drugs. Retrovirology 8:91-4690-8-91.

Behrendt R, Schumann T, Gerbaulet A, Nguyen LA, Schubert N, Alexopoulou D, Berka U, Lienenklaus S, Peschke K, Gibbert K, Wittmann S, Lindemann D, Weiss S, Dahl A, Naumann R, Dittmer U, Kim B, Mueller W, Gramberg T, Roers A. 2013. Mouse SAMHD1 has antiretroviral activity and suppresses a spontaneous cell-intrinsic antiviral response. Cell Rep 4:689-696.

Bowie AG, Unterholzner L. 2008. Viral evasion and subversion of pattern-recognition receptor signalling. Nat Rev Immunol 8:911-922.

Broz P, Monack DM. 2013. Newly described pattern recognition receptors team up against intracellular pathogens. Nat Rev Immunol 13:551-565.

Bubeck D, Reijns MA, Graham SC, Astell KR, Jones EY, Jackson AP. 2011. PCNA directs type 2 RNase H activity on DNA replication and repair substrates. Nucleic Acids Res 39:3652-3666.

Cerritelli SM, Crouch RJ. 2009. Ribonuclease H: The enzymes in eukaryotes. FEBS J 276:1494-1505.

Cerritelli SM, Frolova EG, Feng C, Grinberg A, Love PE, Crouch RJ. 2003. Failure to produce mitochondrial DNA results in embryonic lethality in Rnaseh1 null mice. Mol Cell 11:807-815.

Chabes A, Georgieva B, Domkin V, Zhao X, Rothstein R, Thelander L. 2003. Survival of DNA damage in yeast directly depends on increased dNTP levels allowed by relaxed feedback inhibition of ribonucleotide reductase. Cell 112:391-401.

Chen J, Baig E, Fish EN. 2004. Diversity and relatedness among the type I interferons. J Interferon Cytokine Res 24:687-698.

Chitrabamrung S, Rubin RL, Tan EM. 1981. Serum deoxyribonuclease I and clinical activity in systemic lupus erythematosus. Rheumatol Int 1:55-60.

Chiu YH, Macmillan JB, Chen ZJ. 2009. RNA polymerase III detects cytosolic DNA and induces type I interferons through the RIG-I pathway. Cell 138:576-591.

Chomczynski P, Sacchi N. 2006. The single-step method of RNA isolation by acid guanidinium thiocyanate-phenol-chloroform extraction: Twenty-something years on. Nat Protoc 1:581-585.

Chon H, Vassilev A, DePamphilis ML, Zhao Y, Zhang J, Burgers PM, Crouch RJ, Cerritelli SM. 2009. Contributions of the two accessory subunits, RNASEH2B and RNASEH2C, to the activity and properties of the human RNase H2 complex. Nucleic Acids Res 37:96-110.

Claverys JP, Lacks SA. 1986. Heteroduplex deoxyribonucleic acid base mismatch repair in bacteria. Microbiol Rev 50:133-165.

Crow YJ. 2011. Type I interferonopathies: A novel set of inborn errors of immunity. Ann N Y Acad Sci 1238:91-98.

Crow YJ. 2014. Type I interferonopathies: Mendelian type I interferon up-regulation. Curr Opin Immunol 32C:7-12.

Crow YJ, Hayward BE, Parmar R, Robins P, Leitch A, Ali M, Black DN, van Bokhoven H, Brunner HG, Hamel BC, Corry PC, Cowan FM, Frints SG, Klepper J, Livingston JH, Lynch SA, Massey RF, Meritet JF, Michaud JL, Ponsot G, Voit T, Lebon P, Bonthron DT, Jackson AP, Barnes DE, Lindahl T. 2006a. Mutations in the gene encoding the 3'-5' DNA exonuclease TREX1 cause aicardi-goutieres syndrome at the AGS1 locus. Nat Genet 38:917-920.

Crow YJ, Leitch A, Hayward BE, Garner A, Parmar R, Griffith E, Ali M, Semple C, Aicardi J, Babul-Hirji R, Baumann C, Baxter P, Bertini E, Chandler KE, Chitayat D, Cau D, Dery C, Fazzi E, Goizet C, King MD, Klepper J, Lacombe D, Lanzi G, Lyall H, Martinez-Frias ML, Mathieu M, McKeown C, Monier A, Oade Y, Quarrell OW, Rittey CD, Rogers RC, Sanchis A, Stephenson JB, Tacke U, Till M, Tolmie JL, Tomlin P, Voit T, Weschke B, Woods CG, Lebon P, Bonthron DT, Ponting CP, Jackson AP. 2006b. Mutations in genes encoding ribonuclease H2 subunits cause aicardi-goutieres syndrome and mimic congenital viral brain infection. Nat Genet 38:910-916.

Crow YJ, Livingston JH. 2008. Aicardi-goutieres syndrome: An important mendelian mimic of congenital infection. Dev Med Child Neurol 50:410-416.

Crow YJ, Rehwinkel J. 2009. Aicardi-goutieres syndrome and related phenotypes: Linking nucleic acid metabolism with autoimmunity. Hum Mol Genet 18:R130-6.

Cui R, Widlund HR, Feige E, Lin JY, Wilensky DL, Igras VE, D'Orazio J, Fung CY, Schanbacher CF, Granter SR, Fisher DE. 2007. Central role of p53 in the suntan response and pathologic hyperpigmentation. Cell 128:853-864.

d'Adda di Fagagna F, Reaper PM, Clay-Farrace L, Fiegler H, Carr P, Von Zglinicki T, Saretzki G, Carter NP, Jackson SP. 2003. A DNA damage checkpoint response in telomere-initiated senescence. Nature 426:194-198.

D'Amours D, Jackson SP. 2002. The Mre11 complex: At the crossroads of dna repair and checkpoint signalling. Nat Rev Mol Cell Biol 3:317-327.

Darnell JE,Jr, Kerr IM, Stark GR. 1994. Jak-STAT pathways and transcriptional activation in response to IFNs and other extracellular signaling proteins. Science 264:1415-1421.

Diamond J. 2014. Autosomal dominant IFIH1 gain-of-function mutations cause aicardi-goutieres syndrome. Clin Genet 86:473-474.

Dirksen ML, Crouch RJ. 1981. Selective inhibition of RNase H by dextran. J Biol Chem 256:11569-11573.

Eder PS, Walder RY, Walder JA. 1993. Substrate specificity of human RNase H1 and its role in excision repair of ribose residues misincorporated in DNA. Biochimie 75:123-126.

Farkas L, Beiske K, Lund-Johansen F, Brandtzaeg P, Jahnsen FL. 2001. Plasmacytoid dendritic cells (natural interferon- alpha/beta-producing cells) accumulate in cutaneous lupus erythematosus lesions. Am J Pathol 159:237-243.

Fearon DT, Locksley RM. 1996. The instructive role of innate immunity in the acquired immune response. Science 272:50-53.

Figiel M, Chon H, Cerritelli SM, Cybulska M, Crouch RJ, Nowotny M. 2011. The structural and biochemical characterization of human RNase H2 complex reveals the molecular basis for substrate recognition and aicardi-goutieres syndrome defects. J Biol Chem 286:10540-10550.

Frank P, Braunshofer-Reiter C, Wintersberger U, Grimm R, Busen W. 1998. Cloning of the cDNA encoding the large subunit of human RNase HI, a homologue of the prokaryotic RNase HII. Proc Natl Acad Sci U S A 95:12872-12877.

Friedel RH, Seisenberger C, Kaloff C, Wurst W. 2007. EUCOMM--the european conditional mouse mutagenesis program. Brief Funct Genomic Proteomic 6:180-185.

Fuchs E. 2008. Skin stem cells: Rising to the surface. J Cell Biol 180:273-284.

Funabiki M, Kato H, Miyachi Y, Toki H, Motegi H, Inoue M, Minowa O, Yoshida A, Deguchi K, Sato H, Ito S, Shiroishi T, Takeyasu K, Noda T, Fujita T. 2014. Autoimmune disorders associated with gain of function of the intracellular sensor MDA5. Immunity 40:199-212.

Gall A, Treuting P, Elkon KB, Loo YM, Gale M,Jr, Barber GN, Stetson DB. 2012. Autoimmunity initiates in nonhematopoietic cells and progresses via lymphocytes in an interferon-dependent autoimmune disease. Immunity 36:120-131.

Goldstone DC, Ennis-Adeniran V, Hedden JJ, Groom HC, Rice GI, Christodoulou E, Walker PA, Kelly G, Haire LF, Yap MW, de Carvalho LP, Stoye JP, Crow YJ, Taylor IA, Webb M. 2011. HIV-1 restriction factor SAMHD1 is a deoxynucleoside triphosphate triphosphohydrolase. Nature 480:379-382.

Golub R, Cumano A. 2013. Embryonic hematopoiesis. Blood Cells Mol Dis 51:226-231.

Goubau D, Schlee M, Deddouche S, Pruijssers AJ, Zillinger T, Goldeck M, Schuberth C, Van der Veen AG, Fujimura T, Rehwinkel J, Iskarpatyoti JA, Barchet W, Ludwig J, Dermody TS, Hartmann G, Reis e Sousa C. 2014. Antiviral immunity via RIG-I-mediated recognition of RNA bearing 5'-diphosphates. Nature 514:372-375.

Grammatikos AP, Tsokos GC. 2012. Immunodeficiency and autoimmunity: Lessons from systemic lupus erythematosus. Trends Mol Med 18:101-108.

Günther C, Kind B, Reijns MA, Berndt N, Martinez-Bueno M, Wolf C, Tungler V, Chara O, Lee YA, Hubner N, Bicknell L, Blum S, Krug C, Schmidt F, Kretschmer S, Koss S, Astell KR, Ramantani G, Bauerfeind A, Morris DL, Cunninghame Graham DS, Bubeck D, Leitch A, Ralston SH, Blackburn EA, Gahr M, Witte T, Vyse TJ, Melchers I, Mangold E, Nothen MM, Aringer M, Kuhn A, Luthke K, Unger L, Bley A, Lorenzi A, Isaacs JD, Alexopoulou D, Conrad K, Dahl A, Roers A, Alarcon-Riquelme ME, Jackson AP, Lee-Kirsch MA. 2015. Defective

removal of ribonucleotides from DNA promotes systemic autoimmunity. J Clin Invest 125:413-424.

Gurtler C, Bowie AG. 2013. Innate immune detection of microbial nucleic acids. Trends Microbiol 21:413-420.

Harper JW, Elledge SJ. 2007. The DNA damage response: Ten years after. Mol Cell 28:739-745.

Hartner JC, Walkley CR, Lu J, Orkin SH. 2009. ADAR1 is essential for the maintenance of hematopoiesis and suppression of interferon signaling. Nat Immunol 10:109-115.

Hiller B, Achleitner M, Glage S, Naumann R, Behrendt R, Roers A. 2012. Mammalian RNase H2 removes ribonucleotides from DNA to maintain genome integrity. J Exp Med 209:1419-1426.

Hoffmann J, Akira S. 2013. Innate immunity. Curr Opin Immunol 25:1-3.

Hornung V, Ellegast J, Kim S, Brzozka K, Jung A, Kato H, Poeck H, Akira S, Conzelmann KK, Schlee M, Endres S, Hartmann G. 2006. 5'-triphosphate RNA is the ligand for RIG-I. Science 314:994-997.

Iannello A, Debbeche O, Martin E, Attalah LH, Samarani S, Ahmad A. 2006. Viral strategies for evading antiviral cellular immune responses of the host. J Leukoc Biol 79:16-35.

Ishikawa H, Barber GN. 2008. STING is an endoplasmic reticulum adaptor that facilitates innate immune signalling. Nature 455:674-678.

Jackson SP, Bartek J. 2009. The DNA-damage response in human biology and disease. Nature 461:1071-1078.

Jameson SC. 2002. Maintaining the norm: T-cell homeostasis. Nat Rev Immunol 2:547-556.

Janeway CA,Jr, Medzhitov R. 2002. Innate immune recognition. Annu Rev Immunol 20:197-216.

Jensen KB, Driskell RR, Watt FM. 2010. Assaying proliferation and differentiation capacity of stem cells using disaggregated adult mouse epidermis. Nat Protoc 5:898-911.

Jeong HS, Backlund PS, Chen HC, Karavanov AA, Crouch RJ. 2004. RNase H2 of saccharomyces cerevisiae is a complex of three proteins. Nucleic Acids Res 32:407-414.

Jiang X, Kinch LN, Brautigam CA, Chen X, Du F, Grishin NV, Chen ZJ. 2012. Ubiquitin-induced oligomerization of the RNA sensors RIG-I and MDA5 activates antiviral innate immune response. Immunity 36:959-973.

Joshi R. 2013. Interface dermatitis. Indian J Dermatol Venereol Leprol 79:349-359.

Joyce CM. 1997. Choosing the right sugar: How polymerases select a nucleotide substrate. Proc Natl Acad Sci U S A 94:1619-1622.

Kato H, Takeuchi O, Mikamo-Satoh E, Hirai R, Kawai T, Matsushita K, Hiiragi A, Dermody TS, Fujita T, Akira S. 2008. Length-dependent recognition of double-stranded ribonucleic acids by retinoic acid-inducible gene-I and melanoma differentiation-associated gene 5. J Exp Med 205:1601-1610.

Kawai T, Akira S. 2010. The role of pattern-recognition receptors in innate immunity: Update on toll-like receptors. Nat Immunol 11:373-384.

Kawai T, Akira S. 2011. Toll-like receptors and their crosstalk with other innate receptors in infection and immunity. Immunity 34:637-650.

Kawai T, Takahashi K, Sato S, Coban C, Kumar H, Kato H, Ishii KJ, Takeuchi O, Akira S. 2005. IPS-1, an adaptor triggering RIG-I- and Mda5-mediated type I interferon induction. Nat Immunol 6:981-988.

Kim N, Huang SN, Williams JS, Li YC, Clark AB, Cho JE, Kunkel TA, Pommier Y, Jinks-Robertson S. 2011. Mutagenic processing of ribonucleotides in DNA by yeast topoisomerase I. Science 332:1561-1564.

Kind B, Muster B, Staroske W, Herce HD, Sachse R, Rapp A, Schmidt F, Koss S, Cardoso MC, Lee-Kirsch MA. 2014. Altered spatio-temporal dynamics of RNase H2 complex assembly at replication and repair sites in aicardi-goutieres syndrome. Hum Mol Genet 23:5950-5960.

Kracker S, Radbruch A. 2004. Immunoglobulin class switching: In vitro induction and analysis. Methods Mol Biol 271:149-159.

Krämer A, Green J, Pollard J,Jr, Tugendreich S. 2014. Causal analysis approaches in ingenuity pathway analysis. Bioinformatics 30:523-530.

Kumar H, Kawai T, Akira S. 2011. Pathogen recognition by the innate immune system. Int Rev Immunol 30:16-34.

Lan YY, Londono D, Bouley R, Rooney MS, Hacohen N. 2014. Dnase2a deficiency uncovers lysosomal clearance of damaged nuclear DNA via autophagy. Cell Rep 9:180-192.

Leadbetter EA, Rifkin IR, Hohlbaum AM, Beaudette BC, Shlomchik MJ, Marshak-Rothstein A. 2002. Chromatin-IgG complexes activate B cells by dual engagement of IgM and toll-like receptors. Nature 416:603-607.

Lebon P, Badoual J, Ponsot G, Goutieres F, Hemeury-Cukier F, Aicardi J. 1988. Intrathecal synthesis of interferon-alpha in infants with progressive familial encephalopathy. J Neurol Sci 84:201-208.

Lee J, Kumagai A, Dunphy WG. 2007. The Rad9-Hus1-Rad1 checkpoint clamp regulates interaction of TopBP1 with ATR. J Biol Chem 282:28036-28044.

Lee-Kirsch MA, Gong M, Chowdhury D, Senenko L, Engel K, Lee YA, de Silva U, Bailey SL, Witte T, Vyse TJ, Kere J, Pfeiffer C, Harvey S, Wong A, Koskenmies S, Hummel O, Rohde K, Schmidt RE, Dominiczak AF, Gahr M, Hollis T, Perrino FW, Lieberman J, Hubner N. 2007. Mutations in the gene encoding the 3'-5' DNA exonuclease TREX1 are associated with systemic lupus erythematosus. Nat Genet 39:1065-1067.

Liu YJ. 2001. Dendritic cell subsets and lineages, and their functions in innate and adaptive immunity. Cell 106:259-262.

Loo YM, Gale M,Jr. 2011. Immune signaling by RIG-I-like receptors. Immunity 34:680-692.

Lukas J, Lukas C, Bartek J. 2011. More than just a focus: The chromatin response to DNA damage and its role in genome integrity maintenance. Nat Cell Biol 13:1161-1169.

Madison KC. 2003. Barrier function of the skin: "La raison d'etre" of the epidermis. J Invest Dermatol 121:231-241.

Mannion NM, Greenwood SM, Young R, Cox S, Brindle J, Read D, Nellaker C, Vesely C, Ponting CP, McLaughlin PJ, Jantsch MF, Dorin J, Adams IR, Scadden AD, Ohman M,

Keegan LP, O'Connell MA. 2014. The RNA-editing enzyme ADAR1 controls innate immune responses to RNA. Cell Rep 9:1482-1494.

Matzinger P. 1994. Tolerance, danger, and the extended family. Annu Rev Immunol 12:991-1045.

Matzinger P. 2002. The danger model: A renewed sense of self. Science 296:301-305.

Medzhitov R. 2007. Recognition of microorganisms and activation of the immune response. Nature 449:819-826.

Medzhitov R, Janeway CA,Jr. 1997. Innate immunity: Impact on the adaptive immune response. Curr Opin Immunol 9:4-9.

Meek DW. 2009. Tumour suppression by p53: A role for the DNA damage response? Nat Rev Cancer 9:714-723.

Mellman I, Steinman RM. 2001. Dendritic cells: Specialized and regulated antigen processing machines. Cell 106:255-258.

Meylan E, Curran J, Hofmann K, Moradpour D, Binder M, Bartenschlager R, Tschopp J. 2005. Cardif is an adaptor protein in the RIG-I antiviral pathway and is targeted by hepatitis C virus. Nature 437:1167-1172.

Mok CC, Lau CS. 2003. Pathogenesis of systemic lupus erythematosus. J Clin Pathol 56:481-490.

Mombaerts P, Iacomini J, Johnson RS, Herrup K, Tonegawa S, Papaioannou VE. 1992. RAG-1-deficient mice have no mature B and T lymphocytes. Cell 68:869-877.

Morita M, Stamp G, Robins P, Dulic A, Rosewell I, Hrivnak G, Daly G, Lindahl T, Barnes DE. 2004. Gene-targeted mice lacking the Trex1 (DNase III) 3'-->5' DNA exonuclease develop inflammatory myocarditis. Mol Cell Biol 24:6719-6727.

Morrison SJ, Hemmati HD, Wandycz AM, Weissman IL. 1995. The purification and characterization of fetal liver hematopoietic stem cells. Proc Natl Acad Sci U S A 92:10302-10306.

Morrison SJ, Weissman IL. 1994. The long-term repopulating subset of hematopoietic stem cells is deterministic and isolatable by phenotype. Immunity 1:661-673.

Moynahan ME, Chiu JW, Koller BH, Jasin M. 1999. Brca1 controls homology-directed DNA repair. Mol Cell 4:511-518.

Muller U, Steinhoff U, Reis LF, Hemmi S, Pavlovic J, Zinkernagel RM, Aguet M. 1994. Functional role of type I and type II interferons in antiviral defense. Science 264:1918-1921.

Nagasawa T. 2006. Microenvironmental niches in the bone marrow required for B-cell development. Nat Rev Immunol 6:107-116.

Nandakumar J, Cech TR. 2013. Finding the end: Recruitment of telomerase to telomeres. Nat Rev Mol Cell Biol 14:69-82.

Nick McElhinny SA, Kumar D, Clark AB, Watt DL, Watts BE, Lundstrom EB, Johansson E, Chabes A, Kunkel TA. 2010. Genome instability due to ribonucleotide incorporation into DNA. Nat Chem Biol 6:774-781.

Nudler E, Mustaev A, Lukhtanov E, Goldfarb A. 1997. The RNA-DNA hybrid maintains the register of transcription by preventing backtracking of RNA polymerase. Cell 89:33-41.

Oda H, Nakagawa K, Abe J, Awaya T, Funabiki M, Hijikata A, Nishikomori R, Funatsuka M, Ohshima Y, Sugawara Y, Yasumi T, Kato H, Shirai T, Ohara O, Fujita T, Heike T. 2014. Aicardi-goutieres syndrome is caused by IFIH1 mutations. Am J Hum Genet 95:121-125.

Oldenburg M, Kruger A, Ferstl R, Kaufmann A, Nees G, Sigmund A, Bathke B, Lauterbach H, Suter M, Dreher S, Koedel U, Akira S, Kawai T, Buer J, Wagner H, Bauer S, Hochrein H, Kirschning CJ. 2012. TLR13 recognizes bacterial 23S rRNA devoid of erythromycin resistance-forming modification. Science 337:1111-1115.

Pardo A, Selman M. 2002. Idiopathic pulmonary fibrosis: New insights in its pathogenesis. Int J Biochem Cell Biol 34:1534-1538.

Pena-Diaz J, Bregenhorn S, Ghodgaonkar M, Follonier C, Artola-Boran M, Castor D, Lopes M, Sartori AA, Jiricny J. 2012. Noncanonical mismatch repair as a source of genomic instability in human cells. Mol Cell 47:669-680.

Perrino FW, Harvey S, Shaban NM, Hollis T. 2009. RNaseH2 mutants that cause aicardi-goutieres syndrome are active nucleases. J Mol Med (Berl) 87:25-30.

Pestka S, Krause CD, Walter MR. 2004. Interferons, interferon-like cytokines, and their receptors. Immunol Rev 202:8-32.

Pichlmair A, Schulz O, Tan CP, Naslund TI, Liljestrom P, Weber F, Reis e Sousa C. 2006. RIG-I-mediated antiviral responses to single-stranded RNA bearing 5'-phosphates. Science 314:997-1001.

Poon IK, Lucas CD, Rossi AG, Ravichandran KS. 2014. Apoptotic cell clearance: Basic biology and therapeutic potential. Nat Rev Immunol 14:166-180.

Potenski CJ, Klein HL. 2014. How the misincorporation of ribonucleotides into genomic DNA can be both harmful and helpful to cells. Nucleic Acids Res 42:10226-10234.

Purton LE, Scadden DT. 2007. Limiting factors in murine hematopoietic stem cell assays. Cell Stem Cell 1:263-270.

Quevedo WC,Jr, Fleischmann RD. 1980. Developmental biology of mammalian melanocytes. J Invest Dermatol 75:116-120.

Ramantani G, Kohlhase J, Hertzberg C, Innes AM, Engel K, Hunger S, Borozdin W, Mah JK, Ungerath K, Walkenhorst H, Richardt HH, Buckard J, Bevot A, Siegel C, von Stulpnagel C, Ikonomidou C, Thomas K, Proud V, Niemann F, Wieczorek D, Hausler M, Niggemann P, Baltaci V, Conrad K, Lebon P, Lee-Kirsch MA. 2010. Expanding the phenotypic spectrum of lupus erythematosus in aicardi-goutieres syndrome. Arthritis Rheum 62:1469-1477.

Ramdas L, Wang J, Hu L, Cogdell D, Taylor E, Zhang W. 2001. Comparative evaluation of laser-based microarray scanners. BioTechniques 31:546, 548, 550, passim.

Ravichandran KS, Lorenz U. 2007. Engulfment of apoptotic cells: Signals for a good meal. Nat Rev Immunol 7:964-974.

Rehwinkel J, Maelfait J, Bridgeman A, Rigby R, Hayward B, Liberatore RA, Bieniasz PD, Towers GJ, Moita LF, Crow YJ, Bonthron DT, Reis e Sousa C. 2013. SAMHD1-dependent retroviral control and escape in mice. EMBO J 32:2454-2462.

Reijns MA, Bubeck D, Gibson LC, Graham SC, Baillie GS, Jones EY, Jackson AP. 2011. The structure of the human RNase H2 complex defines key interaction interfaces relevant to enzyme function and human disease. J Biol Chem 286:10530-10539.

Reijns MA, Rabe B, Rigby RE, Mill P, Astell KR, Lettice LA, Boyle S, Leitch A, Keighren M, Kilanowski F, Devenney PS, Sexton D, Grimes G, Holt IJ, Hill RE, Taylor MS, Lawson KA, Dorin JR, Jackson AP. 2012. Enzymatic removal of ribonucleotides from DNA is essential for mammalian genome integrity and development. Cell 149:1008-1022.

Rice G, Patrick T, Parmar R, Taylor CF, Aeby A, Aicardi J, Artuch R, Montalto SA, Bacino CA, Barroso B, Baxter P, Benko WS, Bergmann C, Bertini E, Biancheri R, Blair EM, Blau N, Bonthron DT, Briggs T, Brueton LA, Brunner HG, Burke CJ, Carr IM, Carvalho DR, Chandler KE, Christen HJ, Corry PC, Cowan FM, Cox H, D'Arrigo S, Dean J, De Laet C, De Praeter C, Dery C, Ferrie CD, Flintoff K, Frints SG, Garcia-Cazorla A, Gener B, Goizet C, Goutieres F, Green AJ, Guet A, Hamel BC, Hayward BE, Heiberg A, Hennekam RC, Husson M, Jackson AP, Jayatunga R, Jiang YH, Kant SG, Kao A, King MD, Kingston HM, Klepper J, van der Knaap MS, Kornberg AJ, Kotzot D, Kratzer W, Lacombe D, Lagae L, Landrieu PG, Lanzi G, Leitch A, Lim MJ, Livingston JH, Lourenco CM, Lyall EG, Lynch SA, Lyons MJ, Marom D, McClure JP, McWilliam R, Melancon SB, Mewasingh LD, Moutard ML, Nischal KK, Ostergaard JR, Prendiville J, Rasmussen M, Rogers RC, Roland D, Rosser EM, Rostasy K, Roubertie A, Sanchis A, Schiffmann R, Scholl-Burgi S, Seal S, Shalev SA, Corcoles CS, Sinha GP, Soler D, Spiegel R, Stephenson JB, Tacke U, Tan TY, Till M, Tolmie JL, Tomlin P, Vagnarelli F, Valente EM, Van Coster RN, Van der Aa N, Vanderver A, Vles JS, Voit T, Wassmer E, Weschke B, Whiteford ML, Willemsen MA, Zankl A, Zuberi SM, Orcesi S, Fazzi E, Lebon P, Crow YJ. 2007. Clinical and molecular phenotype of aicardi-goutieres syndrome. Am J Hum Genet 81:713-725.

Rice GI, Bond J, Asipu A, Brunette RL, Manfield IW, Carr IM, Fuller JC, Jackson RM, Lamb T, Briggs TA, Ali M, Gornall H, Couthard LR, Aeby A, Attard-Montalto SP, Bertini E, Bodemer C, Brockmann K, Brueton LA, Corry PC, Desguerre I, Fazzi E, Cazorla AG, Gener B, Hamel BC, Heiberg A, Hunter M, van der Knaap MS, Kumar R, Lagae L, Landrieu PG, Lourenco CM, Marom D, McDermott MF, van der Merwe W, Orcesi S, Prendiville JS, Rasmussen M, Shalev SA, Soler DM, Shinawi M, Spiegel R, Tan TY, Vanderver A, Wakeling EL, Wassmer E, Whittaker E, Lebon P, Stetson DB, Bonthron DT, Crow YJ. 2009. Mutations involved in aicardi-goutieres syndrome implicate SAMHD1 as regulator of the innate immune response. Nat Genet 41:829-832.

Rice GI, del Toro Duany Y, Jenkinson EM, Forte GM, Anderson BH, Ariaudo G, Bader-Meunier B, Baildam EM, Battini R, Beresford MW, Casarano M, Chouchane M, Cimaz R, Collins AE, Cordeiro NJ, Dale RC, Davidson JE, De Waele L, Desguerre I, Faivre L, Fazzi E, Isidor B, Lagae L, Latchman AR, Lebon P, Li C, Livingston JH, Lourenco CM, Mancardi MM, Masurel-Paulet A, McInnes IB, Menezes MP, Mignot C, O'Sullivan J, Orcesi S, Picco PP, Riva E, Robinson RA, Rodriguez D, Salvatici E, Scott C, Szybowska M, Tolmie JL, Vanderver A, Vanhulle C, Vieira JP, Webb K, Whitney RN, Williams SG, Wolfe LA, Zuberi SM, Hur S, Crow YJ. 2014. Gain-of-function mutations in IFIH1 cause a spectrum of human disease phenotypes associated with upregulated type I interferon signaling. Nat Genet 46:503-509.

Rice GI, Kasher PR, Forte GM, Mannion NM, Greenwood SM, Szynkiewicz M, Dickerson JE, Bhaskar SS, Zampini M, Briggs TA, Jenkinson EM, Bacino CA, Battini R, Bertini E, Brogan PA, Brueton LA, Carpanelli M, De Laet C, de Lonlay P, del Toro M, Desguerre I, Fazzi E, Garcia-Cazorla A, Heiberg A, Kawaguchi M, Kumar R, Lin JP, Lourenco CM, Male AM, Marques W,Jr, Mignot C, Olivieri I, Orcesi S, Prabhakar P, Rasmussen M, Robinson RA, Rozenberg F, Schmidt JL, Steindl K, Tan TY, van der Merwe WG, Vanderver A, Vassallo G, Wakeling EL, Wassmer E, Whittaker E, Livingston JH, Lebon P, Suzuki T, McLaughlin PJ, Keegan LP, O'Connell MA, Lovell SC, Crow YJ. 2012. Mutations in ADAR1 cause aicardi-goutieres syndrome associated with a type I interferon signature. Nat Genet 44:1243-1248.

Rich T, Allen RL, Wyllie AH. 2000. Defying death after DNA damage. Nature 407:777-783.

Rickert RC, Roes J, Rajewsky K. 1997. B lymphocyte-specific, cre-mediated mutagenesis in mice. Nucleic Acids Res 25:1317-1318.

Rigby RE, Leitch A, Jackson AP. 2008. Nucleic acid-mediated inflammatory diseases. Bioessays 30:833-842.

Roberts RW, Crothers DM. 1992. Stability and properties of double and triple helices: Dramatic effects of RNA or DNA backbone composition. Science 258:1463-1466.

Rodriguez CI, Buchholz F, Galloway J, Sequerra R, Kasper J, Ayala R, Stewart AF, Dymecki SM. 2000. High-efficiency deleter mice show that FLPe is an alternative to cre-loxP. Nat Genet 25:139-140.

Rogakou EP, Pilch DR, Orr AH, Ivanova VS, Bonner WM. 1998. DNA double-stranded breaks induce histone H2AX phosphorylation on serine 139. J Biol Chem 273:5858-5868.

Roy D, Lieber MR. 2009. G clustering is important for the initiation of transcription-induced R-loops in vitro, whereas high G density without clustering is sufficient thereafter. Mol Cell Biol 29:3124-3133.

Roy D, Yu K, Lieber MR. 2008. Mechanism of R-loop formation at immunoglobulin class switch sequences. Mol Cell Biol 28:50-60.

Roy D, Zhang Z, Lu Z, Hsieh CL, Lieber MR. 2010. Competition between the RNA transcript and the nontemplate DNA strand during R-loop formation in vitro: A nick can serve as a strong R-loop initiation site. Mol Cell Biol 30:146-159.

Roy R, Chun J, Powell SN. 2011. BRCA1 and BRCA2: Different roles in a common pathway of genome protection. Nat Rev Cancer 12:68-78.

Rydberg B, Game J. 2002. Excision of misincorporated ribonucleotides in DNA by RNase H (type 2) and FEN-1 in cell-free extracts. Proc Natl Acad Sci U S A 99:16654-16659.

Ryoo J, Choi J, Oh C, Kim S, Seo M, Kim SY, Seo D, Kim J, White TE, Brandariz-Nunez A, Diaz-Griffero F, Yun CH, Hollenbaugh JA, Kim B, Baek D, Ahn K. 2014. The ribonuclease activity of SAMHD1 is required for HIV-1 restriction. Nat Med 20:936-941.

Sadler AJ, Williams BR. 2008. Interferon-inducible antiviral effectors. Nat Rev Immunol 8:559-568.

Schlee M, Roth A, Hornung V, Hagmann CA, Wimmenauer V, Barchet W, Coch C, Janke M, Mihailovic A, Wardle G, Juranek S, Kato H, Kawai T, Poeck H, Fitzgerald KA, Takeuchi O, Akira S, Tuschl T, Latz E, Ludwig J, Hartmann G. 2009. Recognition of 5' triphosphate by RIG-I helicase requires short blunt double-stranded RNA as contained in panhandle of negative-strand virus. Immunity 31:25-34.

Schmidt-Supprian M, Rajewsky K. 2007. Vagaries of conditional gene targeting. Nat Immunol 8:665-668.

Schoggins JW, Wilson SJ, Panis M, Murphy MY, Jones CT, Bieniasz P, Rice CM. 2011. A diverse range of gene products are effectors of the type I interferon antiviral response. Nature 472:481-485.

Scholzen T, Gerdes J. 2000. The ki-67 protein: From the known and the unknown. J Cell Physiol 182:311-322.

Schöpf B, Bregenhorn S, Quivy JP, Kadyrov FA, Almouzni G, Jiricny J. 2012. Interplay between mismatch repair and chromatin assembly. Proc Natl Acad Sci U S A 109:1895-1900.

Sekiguchi J, Shuman S. 1997. Site-specific ribonuclease activity of eukaryotic DNA topoisomerase I. Mol Cell 1:89-97.

Seth RB, Sun L, Ea CK, Chen ZJ. 2005. Identification and characterization of MAVS, a mitochondrial antiviral signaling protein that activates NF-kappaB and IRF 3. Cell 122:669-682.

Shaw NN, Arya DP. 2008. Recognition of the unique structure of DNA:RNA hybrids. Biochimie 90:1026-1039.

Skourti-Stathaki K, Proudfoot NJ. 2014. A double-edged sword: R loops as threats to genome integrity and powerful regulators of gene expression. Genes Dev 28:1384-1396.

Sontheimer RD. 2009a. Lichenoid tissue reaction/interface dermatitis: Clinical and histological perspectives. J Invest Dermatol 129:1088-1099.

Sontheimer RD. 2009b. Lichenoid tissue reaction/interface dermatitis: Clinical and histological perspectives. J Invest Dermatol 129:1088-1099.

Sotiropoulou PA, Karambelas AE, Debaugnies M, Candi A, Bouwman P, Moers V, Revenco T, Rocha AS, Sekiguchi K, Jonkers J, Blanpain C. 2013. BRCA1 deficiency in skin epidermis leads to selective loss of hair follicle stem cells and their progeny. Genes Dev 27:39-51.

Stadtfeld M, Graf T. 2005. Assessing the role of hematopoietic plasticity for endothelial and hepatocyte development by non-invasive lineage tracing. Development 132:203-213.

Stark GR, Darnell JE,Jr. 2012. The JAK-STAT pathway at twenty. Immunity 36:503-514.

Stetson DB, Ko JS, Heidmann T, Medzhitov R. 2008. Trex1 prevents cell-intrinsic initiation of autoimmunity. Cell 134:587-598.

Sun L, Wu J, Du F, Chen X, Chen ZJ. 2013. Cyclic GMP-AMP synthase is a cytosolic DNA sensor that activates the type I interferon pathway. Science 339:786-791.

Sun Q, Sun L, Liu HH, Chen X, Seth RB, Forman J, Chen ZJ. 2006. The specific and essential role of MAVS in antiviral innate immune responses. Immunity 24:633-642.

Sun W, Li Y, Chen L, Chen H, You F, Zhou X, Zhou Y, Zhai Z, Chen D, Jiang Z. 2009. ERIS, an endoplasmic reticulum IFN stimulator, activates innate immune signaling through dimerization. Proc Natl Acad Sci U S A 106:8653-8658.

Suzuki Y, Holmes JB, Cerritelli SM, Sakhuja K, Minczuk M, Holt IJ, Crouch RJ. 2010. An upstream open reading frame and the context of the two AUG codons affect the abundance of mitochondrial and nuclear RNase H1. Mol Cell Biol 30:5123-5134.

Takeuchi O, Akira S. 2010. Pattern recognition receptors and inflammation. Cell 140:805-820.

Taylor WR, Stark GR. 2001. Regulation of the G2/M transition by p53. Oncogene 20:1803-1815.

Testa G, Schaft J, van der Hoeven F, Glaser S, Anastassiadis K, Zhang Y, Hermann T, Stremmel W, Stewart AF. 2004. A reliable lacZ expression reporter cassette for multipurpose, knockout-first alleles. Genesis 38:151-158.

Traut TW. 1994. Physiological concentrations of purines and pyrimidines. Mol Cell Biochem 140:1-22.

Vasioukhin V, Bauer C, Degenstein L, Wise B, Fuchs E. 2001. Hyperproliferation and defects in epithelial polarity upon conditional ablation of alpha-catenin in skin. Cell 104:605-617.

Vos SM, Tretter EM, Schmidt BH, Berger JM. 2011. All tangled up: How cells direct, manage and exploit topoisomerase function. Nat Rev Mol Cell Biol 12:827-841.

Watt FM. 2014. Mammalian skin cell biology: At the interface between laboratory and clinic. Science 346:937-940.

Westover KD, Bushnell DA, Kornberg RD. 2004. Structural basis of transcription: Nucleotide selection by rotation in the RNA polymerase II active center. Cell 119:481-489.

Williams JS, Kunkel TA. 2014. Ribonucleotides in DNA: Origins, repair and consequences. DNA Repair (Amst) 19:27-37.

Williams JS, Smith DJ, Marjavaara L, Lujan SA, Chabes A, Kunkel TA. 2013. Topoisomerase 1-mediated removal of ribonucleotides from nascent leading-strand DNA. Mol Cell 49:1010-1015.

Wilson A, Oser GM, Jaworski M, Blanco-Bose WE, Laurenti E, Adolphe C, Essers MA, Macdonald HR, Trumpp A. 2007. Dormant and self-renewing hematopoietic stem cells and their niches. Ann N Y Acad Sci 1106:64-75.

Wu J, Chen ZJ. 2014. Innate immune sensing and signaling of cytosolic nucleic acids. Annu Rev Immunol 32:461-488.

Wu J, Sun L, Chen X, Du F, Shi H, Chen C, Chen ZJ. 2013. Cyclic GMP-AMP is an endogenous second messenger in innate immune signaling by cytosolic DNA. Science 339:826-830.

Xu Z, Zan H, Pone EJ, Mai T, Casali P. 2012. Immunoglobulin class-switch DNA recombination: Induction, targeting and beyond. Nat Rev Immunol 12:517-531.

Yang YG, Lindahl T, Barnes DE. 2007. Trex1 exonuclease degrades ssDNA to prevent chronic checkpoint activation and autoimmune disease. Cell 131:873-886.

Yoneyama M, Kikuchi M, Matsumoto K, Imaizumi T, Miyagishi M, Taira K, Foy E, Loo YM, Gale M,Jr, Akira S, Yonehara S, Kato A, Fujita T. 2005. Shared and unique functions of the DExD/H-box helicases RIG-I, MDA5, and LGP2 in antiviral innate immunity. J Immunol 175:2851-2858.

Zhong B, Yang Y, Li S, Wang YY, Li Y, Diao F, Lei C, He X, Zhang L, Tien P, Shu HB. 2008. The adaptor protein MITA links virus-sensing receptors to IRF3 transcription factor activation. Immunity 29:538-550.

Zou L, Elledge SJ. 2003. Sensing DNA damage through ATRIP recognition of RPA-ssDNA complexes. Science 300:1542-1548.

6 Appendix

Table 6.1: List of deregulated genes from a gene expression analysis of total skin from *K14Cre RNaseh2b*^{FLOX} mice.

Deregulated genes with a fold change ≥1.5 and p ≤ 0.05 are displayed.

Probe Set ID	p (corr)	p	FC (abs)	Regulation	Gene Symbol
1450468_at	0.011078357	1.71E-05	7.58	down	Myoc
1436279_at	0.022228211	9.73E-05	7.06	down	Slc26a7
1458268_s_at	0.010874013	1.64E-05	6.38	down	Igfbp3
1423062_at	0.005604662	3.41E-06	5.97	down	Igfbp3
1444451_at	0.022921821	1.05E-04	5.39	down	Pappa2
1419473_a_at	0.02003716	6.84E-05	3.62	down	Cck
1438641_x_at	0.011341926	1.94E-05	3.10	down	Fam57b
1434667_at	0.045409087	4.64E-04	2.71	down	Col8a2
1452807_s_at	0.03454647	2.40E-04	2.53	down	Fam57b
1416693_at	0.022214346	9.63E-05	2.37	down	Foxc2
1417633_at	0.02437203	1.21E-04	2.13	down	Sod3
1417343_at	0.04192272	3.99E-04	2.04	down	Fxyd6
1437937_at	0.039222952	3.25E-04	1.98	down	Ccbp2
1417070_at	0.040957343	3.72E-04	1.95	down	Cyp4v3
1416968_a_at	0.04904834	5.46E-04	1.84	down	Hsd3b7
1460346_at	0.02909892	1.59E-04	1.71	down	Arsa
1448167_at	0.016263928	4.52E-05	1.70	down	Ifngr1
1424029_at	0.047810193	5.20E-04	1.69	down	Tspyl4
1417634_at	0.047810193	5.16E-04	1.68	down	Sod3
1435212_at	0.037562784	2.78E-04	1.67	down	P2rx2
1454104_a_at	0.042330243	4.09E-04	1.66	down	Slc16a9
1454015_a_at	0.011341926	2.12E-05	1.66	down	Cdh13
1429206_at	0.005308266	2.58E-06	1.60	down	Rhobtb1
1448613_at	0.03926199	3.45E-04	1.58	down	Ecm1
1427773_a_at	0.04627189	4.82E-04	1.55	down	Rabac1
1425093_at	0.024503976	1.23E-04	1.55	down	P2rx3
1439038_at	0.043363128	4.28E-04	1.54	down	Khnyn
1421867_at	0.043392874	4.30E-04	1.52	down	Nr3c1
1460319_at	0.033932794	2.23E-04	1.52	down	Fut8
1422803_at	0.039040215	3.17E-04	1.51	down	Fstl3
1457097_at	0.033932794	2.31E-04	1.50	down	Skap2

Probe Set ID	p (Corr)	p	FC (abs)	Regulation	Gene Symbol
1418173_at	1.99E-04	1.09E-08	248..75	up	Krt25
1449378_at	0.003385193	7.46E-07	101.10	up	Krt27
1436557_at	0.012015101	2.35E-05	57.28	up	Krt73
1434425_at	0.002337471	3.86E-07	41.67	up	Tchh
1448457_at	0.003963769	9.82E-07	34.72	up	Krt71
1419507_at	0.045409087	4.63E-04	30.91	up	Krtap15
1427211_at	0.039222952	3.33E-04	30.13	up	Krtap8-1
1419767_at	0.009040871	8.26E-06	21.03	up	Padi3
1439100_s_at	0.048752893	5.37E-04	21.00	up	Krtap11-1
1417717_a_at	0.009040871	9.72E-06	19.30	up	Tyr
1430132_at	0.017622245	5.49E-05	18.92	up	Krt28
1453214_at	0.020978615	7.78E-05	15.98	up	Lrrc15
1429835_at	0.03164906	1.92E-04	15.78	up	2310033E01Rik
1448470_at	0.02873153	1.57E-04	15.61	up	Fbp1
1415861_at	0.005604662	3.55E-06	15.60	up	Tyrp1
1436869_at	0.03336487	2.15E-04	14.92	up	Shh
1456901_at	0.005604662	3.24E-06	14.83	up	Adamts20
1415862_at	0.02759537	1.48E-04	14.71	up	Tyrp1
1415844_at	0.002337471	3.32E-07	12.58	up	Syt4
1422523_at	0.017685393	5.78E-05	12.46	up	Pmel
1423271_at	0.012675797	2.64E-05	11.84	up	Gjb2
1420409_at	0.032779336	2.04E-04	11.58	up	Krt35
1439409_x_at	0.009040871	1.17E-05	11.51	up	Tyrp1
1430635_at	0.037410703	2.72E-04	11.30	up	Mlana
1419709_at	0.020978615	7.79E-05	11.27	up	Stfa3
1436055_at	0.03153318	1.90E-04	10.94	up	Lrrc15
1421856_at	0.045342103	4.58E-04	10.79	up	S100a3
1415845_at	0.009040871	1.01E-05	10.66	up	Syt4
1435761_at	0.039222952	3.29E-04	10.34	up	BC100530///Stfa1
1460185_at	0.017685393	5.67E-05	8.67	up	Krt85
1418028_at	0.009040871	8.75E-06	8.59	up	Dct
1435639_at	0.02386954	1.16E-04	8.04	up	2610528A11Rik
1417422_at	0.017330242	5.22E-05	6.78	up	Gnmt
1448397_at	0.004339723	1.56E-06	6.45	up	Gjb6
1418935_at	0.037357025	2.71E-04	6.40	up	Trpm1
1448485_at	0.020881187	7.48E-05	6.08	up	Ggt1
1448752_at	0.039040215	3.15E-04	5.82	up	Car2
1437445_at	0.016128201	4.34E-05	5.43	up	Trpm1
1419152_at	0.016128201	4.40E-05	5.25	up	2810417H13Rik
1438752_at	0.03390757	2.20E-04	5.23	up	A230058F20Rik
1423952_a_at	0.023398947	1.12E-04	4.95	up	Krt7
1455540_at	0.03560491	2.49E-04	4.87	up	Cps1
1450618_a_at	0.048919447	5.43E-04	4.55	up	Sprr2a1///Sprr2a2
1427372_at	0.039040215	3.16E-04	4.44	up	Cyp27b1
1428304_at	0.017622245	5.58E-05	4.32	up	Esco2

1424629_at	0.03114012	1.87E-04	4.32	up	Brca1
1419153_at	0.022214346	9.67E-05	4.23	up	2810417H13Rik
1418211_at	0.036173876	2.58E-04	4.20	up	Oca2
1424046_at	0.004339723	1.83E-06	4.13	up	Bub1
1429171_a_at	0.008196097	6.32E-06	4.12	up	Ncapg
1437540_at	0.013930823	3.30E-05	4.06	up	Mcoln3
1424292_at	0.009040871	1.15E-05	3.88	up	Depdc1a
1416686_at	0.041561574	3.83E-04	3.80	up	Plod2
1415810_at	0.04192272	3.99E-04	3.78	up	Uhrf1
1424118_a_at	0.015429875	3.95E-05	3.65	up	Spc25
1434240_at	0.02146454	8.58E-05	3.59	up	4632434I11Rik
1448754_at	0.042233054	4.05E-04	3.59	up	Rbp1
1452954_at	0.017622245	5.58E-05	3.58	up	Ube2c
1416802_a_at	0.029505746	1.66E-04	3.57	up	Cdca5
1416687_at	0.04400499	4.41E-04	3.53	up	Plod2
1426817_at	0.011992623	2.28E-05	3.43	up	Mki67
1448205_at	3.74E-04	3.09E-08	3.38	up	Ccnb1///Gm5593
1435306_a_at	0.003385193	7.06E-07	3.33	up	Kif11
1435281_at	0.01274057	2.72E-05	3.31	up	Cpt1c
1417323_at	0.014069148	3.45E-05	3.31	up	Psrc1
1425916_at	0.014069148	3.43E-05	3.31	up	Capn8
1424278_a_at	0.02146454	8.25E-05	3.27	up	Birc5
1417938_at	0.009040871	1.08E-05	3.22	up	Rad51ap1
1452458_s_at	0.009275186	1.28E-05	3.21	up	Lrr1
1454694_a_at	0.023398947	1.12E-04	3.21	up	Top2a
1439040_at	0.014494368	3.63E-05	3.21	up	Cenpe
1418203_at	0.02146454	8.47E-05	3.18	up	Pmaip1
1448314_at	0.018790066	6.25E-05	3.18	up	Cdk1
1433893_s_at	0.02146454	8.52E-05	3.10	up	Spag5
1452242_at	1.41E-04	3.87E-09	3.07	up	Cep55
1424128_x_at	0.012992521	2.93E-05	3.04	up	Aurkb
1418026_at	0.022541879	1.01E-04	3.04	up	Exo1
1419127_at	0.022199633	9.32E-05	3.04	up	Npy
1416558_at	0.016974647	4.85E-05	3.02	up	Melk
1427161_at	0.009040871	1.11E-05	2.99	up	Cenpf
1439377_x_at	0.007017641	5.22E-06	2.99	up	Cdc20
1438009_at	0.023104781	1.06E-04	2.98	up	Hist1h2ab
1417910_at	0.011341926	2.10E-05	2.97	up	Ccna2
1450842_a_at	0.015196107	3.85E-05	2.95	up	Cenpa
1418281_at	0.006813805	4.88E-06	2.95	up	Rad51
1435005_at	0.020916197	7.55E-05	2.91	up	Cenpe
1451246_s_at	0.022907764	1.04E-04	2.91	up	Aurkb
1416299_at	3.81E-04	4.19E-08	2.89	up	Shcbp1
1439019_at	0.037562784	2.77E-04	2.88	up	Fras1
1416309_at	0.006567447	4.52E-06	2.85	up	Nusap1
1436808_x_at	0.033932794	2.32E-04	2.85	up	Mcm5
1416757_at	0.012675797	2.65E-05	2.85	up	Zwilch
1450920_at	0.036173876	2.59E-04	2.84	up	Ccnb2

1452314_at	0.012992521	2.93E-05	2.83	up	Kif11
1448627_s_at	0.02146454	8.47E-05	2.83	up	Pbk
1434748_at	0.012912958	2.81E-05	2.81	up	Ckap2
1449133_at	0.029163785	1.61E-04	2.79	up	Sprr1a
1437611_x_at	0.016974647	4.86E-05	2.75	up	Kif2c
1428105_at	0.03767577	2.90E-04	2.75	up	Tpx2
1432453_a_at	0.026208734	1.38E-04	2.74	up	Ms4a10
1419323_at	0.026782457	1.42E-04	2.73	up	Padi1
1448635_at	0.009040871	1.17E-05	2.70	up	Smc2
1417541_at	0.034454297	2.38E-04	2.70	up	Hells
1434767_at	0.014069148	3.44E-05	2.70	up	Mis18bp1
1421594_a_at	0.030217253	1.78E-04	2.70	up	Sytl2
1449207_a_at	0.046111293	4.78E-04	2.67	up	Kif20a
1447363_s_at	0.02576449	1.35E-04	2.67	up	Bub1b
1421546_a_at	0.020818172	7.40E-05	2.65	up	Racgap1
1422430_at	0.041895613	3.91E-04	2.65	up	Fignl1
1434278_at	0.017622245	5.39E-05	2.64	up	Mtm1
1437716_x_at	0.009275186	1.29E-05	2.62	up	Kif22
1447040_at	0.039222952	3.24E-04	2.61	up	
1458374_at	0.017685393	5.80E-05	2.61	up	Mis18bp1
1416118_at	0.03767577	2.90E-04	2.60	up	Trim59
1419943_s_at	0.023398947	1.13E-04	2.60	up	Ccnb1///Gm5593
1423847_at	0.04067832	3.66E-04	2.60	up	Ncapd2
1437580_s_at	0.04688727	4.89E-04	2.59	up	Nek2
1418334_at	0.016002957	4.19E-05	2.59	up	Dbf4
1429734_at	0.023377985	1.09E-04	2.58	up	4632434I11Rik
1436707_x_at	0.015452961	4.00E-05	2.56	up	Ncaph
1441693_at	0.011078357	1.77E-05	2.55	up	Adamts3
1427707_a_at	0.008415986	6.95E-06	2.55	up	Stil
1456280_at	0.02534305	1.29E-04	2.54	up	Clspn
1428104_at	0.047810193	5.23E-04	2.53	up	Tpx2
1455609_at	0.009275186	1.30E-05	2.53	up	Cit
1416076_at	0.04192272	3.97E-04	2.49	up	Ccnb1///Gm5593
1416342_at	0.02576449	1.35E-04	2.49	up	Tnc
1449877_s_at	0.013691212	3.20E-05	2.48	up	Kifc1
1435575_at	0.016263928	4.52E-05	2.48	up	Kntc1
1416664_at	0.025420498	1.31E-04	2.48	up	Cdc20
1431087_at	0.04949901	5.58E-04	2.46	up	Spc24
1437187_at	0.010408515	1.49E-05	2.46	up	E2f7
1419513_a_at	0.033932794	2.33E-04	2.46	up	Ect2
1437370_at	0.005472912	2.86E-06	2.44	up	Sgol2
1422460_at	0.02146454	8.28E-05	2.43	up	LOC100045924///Mad2l1
1417019_a_at	0.03560491	2.50E-04	2.38	up	Cdc6
1439510_at	0.011341926	2.00E-05	2.37	up	Sgol1
1434280_at	0.046918575	4.91E-04	2.36	up	
1456593_at	0.013691212	3.20E-05	2.36	up	
1449708_s_at	0.029257255	1.64E-04	2.35	up	Chek1
1422814_at	0.009040871	9.54E-06	2.35	up	Aspm

1428481_s_at	0.02873153	1.56E-04	2.34	up	Cdca8
1418264_at	0.016974647	4.79E-05	2.34	up	Cenpk
1436847_s_at	0.011341926	2.08E-05	2.33	up	Cdca8
1425815_a_at	0.004339723	1.77E-06	2.33	up	Hmmr
1416666_at	0.008734481	7.46E-06	2.32	up	Serpine2
1445298_at	0.009040871	1.16E-05	2.31	up	
1434437_x_at	0.03767577	2.90E-04	2.31	up	Rrm2
1454904_at	0.030217253	1.77E-04	2.30	up	Mtm1
1444416_at	0.037562784	2.78E-04	2.30	up	Cenpa
1453226_at	0.011341926	1.95E-05	2.30	up	Kif18b
1448113_at	0.045409087	4.63E-04	2.28	up	Stmn1
1436186_at	0.020978615	7.80E-05	2.27	up	E2f8
1449064_at	0.039040215	3.16E-04	2.27	up	Tdh
1433408_a_at	0.041561574	3.83E-04	2.26	up	Mcm10
1433583_at	0.039222952	3.42E-04	2.26	up	Zfp365
1419539_at	0.033932794	2.24E-04	2.25	up	Irx4
1423524_at	0.012675797	2.63E-05	2.25	up	Mastl
1439436_x_at	0.004339723	1.31E-06	2.23	up	Incenp
1422462_at	0.012574891	2.53E-05	2.23	up	Ube2t
1417450_a_at	0.022214346	9.65E-05	2.23	up	Tacc3
1443230_at	0.03771621	2.97E-04	2.22	up	
1417587_at	0.03167863	1.94E-04	2.22	up	Timeless
1449699_s_at	0.024215348	1.19E-04	2.22	up	C330027C09Rik
1430811_a_at	0.040133316	3.56E-04	2.21	up	Nuf2
1452287_at	0.032973	2.10E-04	2.20	up	Msi1
1439695_a_at	0.012992521	2.86E-05	2.20	up	Kif20b
1437033_a_at	0.004339723	1.71E-06	2.20	up	Skp2
1416961_at	0.03767577	2.83E-04	2.19	up	Bub1b
1437251_at	0.029840494	1.72E-04	2.18	up	Cdca2
1424511_at	0.02146454	8.59E-05	2.17	up	Aurka
1415860_at	0.011341926	2.03E-05	2.16	up	Kpna2
1456482_at	0.017155636	5.05E-05	2.15	up	Pik3r3
1429172_a_at	0.029731033	1.69E-04	2.13	up	Ncapg
1429660_s_at	0.009040871	9.06E-06	2.13	up	Smc2
1415978_at	0.0453028	4.55E-04	2.13	up	Tubb3
1449324_at	0.022285804	9.82E-05	2.12	up	Ero1l
1424268_at	0.033932794	2.30E-04	2.11	up	Smox
1450862_at	0.039222952	3.29E-04	2.11	up	Rad54l
1429295_s_at	0.033932794	2.31E-04	2.10	up	Trip13
1441757_at	0.010874013	1.63E-05	2.10	up	1190002F15Rik
1443086_at	0.039040215	3.12E-04	2.09	up	Alcam
1441991_at	0.039222952	3.42E-04	2.07	up	Prss53
1418969_at	0.032779336	2.05E-04	2.07	up	Skp2
1420081_s_at	0.021874292	8.92E-05	2.06	up	D2Ertd750e
1423092_at	0.037506506	2.75E-04	2.04	up	Incenp
1417926_at	0.011992623	2.31E-05	2.03	up	Ncapg2
1455990_at	0.029624688	1.67E-04	2.03	up	Kif23
1424766_at	0.009040871	1.11E-05	2.03	up	Ercc6l

1419030_at	0.048919447	5.42E-04	2.02	up	Ero1l
1422513_at	0.04067832	3.66E-04	2.01	up	Ccnf
1418919_at	0.005308266	2.63E-06	2.01	up	Sgol1
1428518_at	0.033932794	2.32E-04	2.01	up	Mlf1ip
1433543_at	0.023398947	1.12E-04	1.99	up	Anln
1451377_a_at	0.030590737	1.81E-04	1.99	up	Aaas
1426300_at	0.024503976	1.22E-04	1.98	up	Alcam
1460247_a_at	0.017155636	5.01E-05	1.98	up	Skp2
1415878_at	0.017622245	5.50E-05	1.98	up	Rrm1
1424221_at	0.027517257	1.46E-04	1.97	up	Susd4
1415849_s_at	0.03767577	2.87E-04	1.96	up	Stmn1
1426301_at	0.023192793	1.07E-04	1.95	up	Alcam
1425416_s_at	0.022199633	9.35E-05	1.95	up	Psrc1
1419156_at	0.045885	4.73E-04	1.95	up	Sox4
1437466_at	0.039040215	3.13E-04	1.94	up	Alcam
1433988_s_at	0.013006523	2.97E-05	1.94	up	C230098O21Rik
1436174_at	0.016128201	4.39E-05	1.94	up	Atad2
1431893_a_at	0.032779336	2.06E-04	1.94	up	Pdss1
1438434_at	0.017685393	5.75E-05	1.94	up	Arhgap11a
1455188_at	0.036307853	2.61E-04	1.94	up	Ephb1
1418108_at	0.039222952	3.35E-04	1.93	up	Rtkn2
1416854_at	0.029163785	1.62E-04	192	up	Slc34a2
1439269_x_at	0.028265612	1.53E-04	1.91	up	Mcm7
1430193_at	0.022541879	1.01E-04	1.91	up	Casc5
1417125_at	0.03771621	2.95E-04	1.90	up	Ahcy
1455049_at	0.043249365	4.21E-04	1.89	up	Igsf3
1434564_at	0.04192272	3.99E-04	1.89	up	E2f3
1443354_at	0.01274057	2.74E-05	1.89	up	
1426002_a_at	0.041561574	3.81E-04	1.87	up	Cdc7
1460593_at	0.020818172	7.39E-05	1.87	up	Susd4
1423463_a_at	0.022214346	9.54E-05	1.85	up	D2Ertd750e
1449345_at	0.011078357	1.77E-05	1.85	up	Ccdc34
1419838_s_at	0.025420498	1.31E-04	1.85	up	Plk4
1433807_at	0.03924884	3.44E-04	1.84	up	6720463M24Rik
1416563_at	0.005836203	3.86E-06	1.83	up	Ctps
1416969_at	0.03767577	2.86E-04	1.82	up	Gtse1
1422768_at	0.01429238	3.54E-05	1.82	up	Syncrip
1444646_at	0.033334363	2.14E-04	1.81	up	Bnc2
1432591_at	0.012281142	2.44E-05	1.80	up	Pappa
1448821_at	0.017330242	5.25E-05	1.80	up	Tyr
1452098_at	0.039622713	3.49E-04	1.80	up	Chtf18
1449170_at	0.009040871	8.26E-06	1.80	up	Piwil2
1438063_at	0.03767577	2.86E-04	1.80	up	Mphosph9
1455790_at	0.009090032	1.20E-05	1.78	up	E2f2
1436532_at	0.040570073	3.63E-04	1.78	up	Dclk3
1459741_x_at	0.022519425	9.98E-05	1.76	up	Ucp2
1439394_x_at	0.03873198	3.07E-04	1.76	up	Cdc20
1435773_at	0.011341926	2.10E-05	1.75	up	4930547N16Rik

1426323_x_at	0.02146454	8.61E-05	1.74	up	Siva1
1441081_a_at	0.023227999	1.08E-04	1.73	up	1110038B12Rik
1434399_at	0.02534305	1.29E-04	1.73	up	Galnt6
1423714_at	0.035847817	2.53E-04	1.73	up	Asf1b
1435136_at	0.03771621	2.96E-04	1.73	up	Whsc1
1424971_at	0.04192272	3.96E-04	1.71	up	Ccdc99
1423760_at	0.04192272	3.98E-04	1.71	up	Cd44
1435497_at	0.032973	2.10E-04	1.70	up	5730590G19Rik
1423957_at	0.010874013	1.65E-05	1.68	up	Aen
1447364_x_at	0.043363128	4.27E-04	1.68	up	Myo1b
1419909_at	0.016128201	4.30E-05	1.67	up	Mphosph9
1419556_at	0.03093096	1.84E-04	1.67	up	Elf5
1418184_at	0.040570073	3.63E-04	1.67	up	Cenpm
1422685_at	0.020007981	6.78E-05	1.66	up	Exoc4
1440262_at	0.041561574	3.82E-04	1.64	up	AI414108
1459679_s_at	0.046937827	4.94E-04	1.63	up	Myo1b
1452197_at	0.018790066	6.26E-05	1.62	up	Smc4
1417837_at	0.030217253	1.78E-04	1.62	up	Phlda2
1458076_at	0.03767577	2.93E-04	1.61	up	
1436434_at	0.036173876	2.58E-04	1.61	up	E2f2
1449291_a_at	0.039222952	3.29E-04	1.60	up	Dcbld1
1415829_at	0.037506506	2.74E-04	1.59	up	Lbr
1416575_at	0.030217253	1.75E-04	1.59	up	Cdc45
1431358_at	0.039222952	3.39E-04	1.58	up	4930547N16Rik
1424110_a_at	0.03767577	2.86E-04	1.58	up	Nme1
1459890_s_at	0.04187566	3.88E-04	1.58	up	1110008P14Rik
1423525_at	0.02759537	1.48E-04	1.58	up	Mastl
1421309_at	0.045885	4.72E-04	1.57	up	Mgmt
1422686_s_at	0.005604662	3.49E-06	1.57	up	Exoc4
1448426_at	0.03873198	3.08E-04	1.56	up	Sardh
1450506_a_at	0.043363128	4.26E-04	1.56	up	Aen
1422747_at	0.043363128	4.25E-04	1.56	up	Chek2
1438645_x_at	0.02096506	7.62E-05	1.55	up	Bace2
1419267_at	0.033932794	2.33E-04	1.54	up	Nfyb
1433485_x_at	0.042330243	4.09E-04	1.54	up	Gpr56
1424156_at	0.047810193	5.17E-04	1.53	up	Rbl1
1454659_at	0.02146454	8.17E-05	1.52	up	Dctd
1455035_s_at	0.025596472	1.33E-04	1.52	up	Nop56
1442134_at	0.011341926	1.94E-05	1.52	up	Prr11
1435452_at	0.036452714	2.63E-04	1.51	up	Tmem20
1446507_at	0.008415986	6.79E-06	1.51	up	
1443999_at	0.03167863	1.93E-04	1.51	up	
1434382_at	0.049268622	5.50E-04	1.51	up	Serinc2
1422723_at	0.047810193	5.20E-04	1.51	up	Stra6
1452414_s_at	0.022740904	1.03E-04	1.51	up	Ccdc86
1454642_a_at	0.04697512	4.98E-04	1.51	up	Commd3
1422684_a_at	0.039222952	3.25E-04	1.50	up	Exoc4
1436472_at	0.004339723	1.44E-06	1.50	up	Slfn9

Table 6.2: Top 12 gene cluster from the microarray-based gene expression profile of total skin from *K14Cre Rnaseh2b*$^{FLOX/FLOX}$ mice

#	cluster
1	Cell cycle: G2/M DNA damage checkpoint regulation
2	Cell cycle control of chromosomal replication
3	Mitotic roles of polo-like kinase
4	Estrogen-mediated S-phase entry
5	ATM signaling
6	Role of CHK proteins in cell cycle checkpoint control
7	Role of BRCA1 in DANN damage response
8	Cyclins and cell cycle regulation
9	DANN damage-induced 14-3-3 signaling
10	Hereditary breast cancer signaling
11	Eumelanin biosynthesis
12	p53 signaling

7 Acknowledgements

First of all I would like to thank my supervisor Prof. Dr. Axel Roers for giving me the opportunity to perform my doctoral thesis in his lab:

Axel, I would really like to thank you for almost eight years in your group. I enjoyed every day and I have never regretted to be a diploma and doctoral student in your lab. Thank you for teaching me so many thinks in science but also for the many advices that were not related to science. Thank you for giving me the freedom to work on my own project and to follow my own ideas. You always gave me the feeling to be a special and talented student.

Many thanks to all my colleagues I have met within the last eight years in Cologne and Dresden. Special thanks to the postdocs Dr. Rayk Behrendt and Dr. Alexander Gerbaulet for their great help and the many advices and ideas they shared with me. I also have to thank all the technicians that supported my work, in particular Christina Hiller and Dora Schreier.

I would also like to thank all collaborators that substantially contributed to this thesis and the referees that agreed to evaluate this thesis.

I would like to thank Dora Schreier for more than six years that we spent together in Dresden. Thank you for the great time that we had. Thank you for your big support and being patient in all the stressful times that I had as a PhD student. I would like to apologize that I have missed to appreciate your important contribution to my first scientific publication.

Special thanks to Julia Seifert for her big support with all administrative work, but much more for having an open ear to all my problems in science and in private life.

Finally I like to thanks my parents for everything.